STRUCTURAL BASIS FOR COORDINATION
IN DIMERIC KINESIN

APPROVED BY SUPERVISORY COMMITTEE

Masahide Kikkawa, M.D., Ph.D.

Joseph Albanesi, Ph.D.

Michael Rosen, Ph.D.

Hongtao Yu, Ph.D.

Kevin Gardner, Ph.D.

DEDICATION

Dedicated to my family, whose consistent love, encouragement and support keep me going through the rainy days, and who gave me the best opportunities I could have wished for.

STRUCTURAL BASIS FOR COORDINATION IN DIMERIC KINESIN

by

Zoltan Metlagel

DISSERTATION

Presented to the Faculty of the Graduate School of Biomedical Sciences
The University of Texas Southwestern Medical Center at Dallas
In Partial Fulfillment of the Requirements For the Degree of

DOCTOR OF PHILOSOPHY

The University of Texas Southwestern Medical Center at Dallas
Dallas, Texas
April, 2009

ACKNOWLEDGEMENTS

I would like to acknowledge my mentor, Dr. Masahide Kikkawa for his guidance, support, and lots of patience; Dr. David Hackney at Carnegie Mellon University for his advice and for providing us with the kinesin constructs and copious amounts of kinesin proteins; Dr. Yoshinori Fujiyoshi for his help and guidance, and the opportunity to use his facility and microscopes, and Dr. Kazumi Kobayashi for his time, help, and patience while using the equipment; my committee members, Drs. Joseph Albanesi, Michael Rosen and Hongtao Yu for their support and generous help; Dr. Michael Rosen in particular for accepting me in his lab for my last two years, and for his generosity and guidance during this time; my program chair, Dr. Kevin Gardner, for providing an excellent learning and research environment, and for taking his time to care for his students as individuals. I would also like to acknowledge Dr. Christopher Gilpin, Tom Januszewsky, George Lawton and Laurie Mueller for their help, patience, and for keeping the equipment available and running, therefore making much of this research possible; Dr. Naoko Mizuno for her help and time in getting me started on the electron microscope and image analysis; the crew at JEOL USA, Inc. for sharing their technical insights and knowledge, and everyone who took the time to discuss with me many helpful and interesting topics. Special thanks go to the Rosen Lab for sharing their space, time, and thoughts with me despite the fact that I was more of a lab parasite; to Daeho Lee and Toshiyuki Oda for their friendship and help. I also owe many thanks to a small set of close friends, exceptional individuals who made my life colorful and interesting, and who stuck with me through good times and bad. While their direct contribution to this work may be small, the value of their friendship and support is immeasurable. Finally, I would like to acknowledge Dr. Hong-Hsing Liu, who kindly made his LaTeX template available.

STRUCTURAL BASIS FOR COORDINATION
IN DIMERIC KINESIN

Publication No. _____

Zoltan Metlagel, Ph.D.
The University of Texas Southwestern Medical Center at Dallas, 2009

Supervising Professor: Masahide Kikkawa, M.D., Ph.D.

Kinesin-1 (conventional kinesin) is a protein motor that carries organelles and vesicle cargo along its microtubule track. The two catalytic heads of Kinesin-1 are linked to function as a highly processive "molecular walker" that can take hundreds of steps before falling off the track. A key requirement for processivity is that the nucleotide cycles of the heads are coordinated to prevent simultaneous release of both heads from the track. The structural basis for coordination has not been established yet. Here, we show the conformational changes involved in nucleotide-dependent switching of the kinesin core in the functional context of the microtubule. The observed conformational differences between two key nucleotide states comprise the structural groundwork for future studies on how the nucleotide cycles are coordinated between the heads.

Further, a software suite, Ruby-Helix, was developed to facilitate helical image analysis and implement a new algorithm for the analysis of helical objects with a seam. Ruby-Helix incorporates several new techniques for conventional helical analysis, and automates many of the repetitive steps involved in helical analysis, thereby greatly increasing the throughput of this method.

TABLE OF CONTENTS

LIST OF FIGURES

LIST OF TABLES

LIST OF ABBREVIATIONS

ADP	Adenosine Diphosphate
apo	denotes the nucleotide-free state
ASU	Asymmetric Unit
MAP	Microtubule-Associated Protein
RNA	Ribonucleic Acid
DNA	Deoxyribonucleic Acid
MT	Microtubule
GTP	Guanidine Triphosphate
GDP	Guanidine Diphosphate
GAP	GTPase-Activating Protein
GEF	Guanidine nucleotide Exchange Factor
ATP	Adenosine Triphosphate
ncd	Non-Claret Disjunctional
KIF	Kinesin Family
MCAK	Mitotic Centromere-Associated Kinesin
SEM	Scanning Electron Microscope
CTF	Contrast Transfer Function
FEG	Field Emission Gun
DQE	Detection Quantum Efficiency
SNR	Signal-to-Noise
CCD	Charge-Coupled Device
STEM	Scanning Transmission Electron Microscopy
EELS	Electron Energy Loss Spectroscopy
PSF	Point Spread Function

MDS	Minimal Dose System
FFT	Fast Fourier Transform
CNS	Crystallography & NMR System
RAM	Random Access Memory
AMPPNP	5'-Adenylylimidodiphosphate
KHC	Kinesin Heavy Chain
Cryo-EM	Cryo-Electron Microscopy
FSC	Fourier Shell Correlation
RDP	Radial Density Plot

PRIOR PUBLICATIONS

[1] M. Kikkawa and Z. Metlagel. A molecular "zipper" for microtubules. Cell, 127(7):1302–4, 2006.

[2] Z. Metlagel, Y. S. Kikkawa, and M. Kikkawa. Ruby-Helix: an implementation of helical image processing based on object-oriented scripting language. J Struct Biol, 157(1):95–105, 2007.

CHAPTER ONE
Introduction

Motor Proteins

Active movement is a key feature of living organisms, and is manifested, at its lowest level, in behaviors such as phototaxis (movement towards light), chemotaxis (movement along a chemical gradient), and others involving the directed movement of an organism. On the subcellular level, rotary motors propel certain bacteria (reviewed in [279]), nucleic acid enzymes translocate along RNA or DNA (reviewed in [68, 146, 240]), translocases thread polypeptide chains across membranes [301], and so-called "mechanoenzymes" transport vesicle and organelle cargo within cells.

The mechanoenzymes directly convert the chemical energy derived from ATP into directed motion [16]. The three families of linear mechanoenzymes known to date include myosins, dyneins and kinesins [99]. The myosin family was first described in the second half of the 19th century (reviewed in [16]) and is a major constituent of the muscle tissues found in higher eukaryotes. It is the only actin-based mechanoenzyme family known to date. The other two families, dyneins and kinesins, track along microtubule (MT) filaments composed of tubulin subunits arranged head-to-tail as protofilaments, which themselves roll up to form a hollow tube [263]. The dynein family of proteins was first described in 1965 [85], but due to a number of technical difficulties remains the least well characterized. In contrast, the first kinesin was described only in 1985 [22, 318], but has since become one of the best studied motor proteins. In addition, kinesin has given rise to a large protein family that includes not only motor proteins, but a variety of regulators of the microtubule cytoskeleton as well.

On a sequence level, the three families of motor proteins share no homology, other than a common P-loop ATP binding motif [99]. Interestingly, however, myosins and kinesins share a similar fold, and several corresponding structural elements in the two proteins share analogous functions (reviewed in [314, 316]). For example, myosins and kinesins generally share a central β-sheet with three α-helices on each side of the β-sheet core domain. Although the connectivities differ between the two protein families, the functions of filament binding [329], and power transmission are performed by the helices in the same relative orientation to the central β-sheet domain. A structure of the kinesin-1 motor core with several important features highlighted is shown in Figure 1.1 on page 47, and the similarities of the myosin and kinesin folds are illustrated in Figure 1.2 on page 48.

Another interesting similarity can be found between kinesins, myosins, and the large family of G-proteins. G-proteins act as "switches", and their activity generally depends on the bound nucleotide, GTP or GDP. On a sequence level, little similarity is found among myosin, kinesin, and G-proteins. However, key residues between the classes seem to be conserved, and the active sites of these proteins, despite differing nucleotides, are remarkably similar. In particular, the P-loop involved in nucleotide binding and the switch I and II regions that sense whether the γ-phosphate of the nucleotide is present or absent, appear to superimpose remarkably well [312, 316]. Common ancestry between proteins is generally detected by sequence similarity. Using only this criterion, kinesin, myosin, and G-proteins cannot be said to be homologous. If, however, structural similarity and functional assignment of secondary structure elements is taken into account, it is likely that these protein families evolved from a common ancestor. In any case, the myosin and kinesin motor families appear to be more similar to one another and to G-proteins than they are to any other nucleotide-binding proteins [314]. It is therefore probable that they diverged early in evolution from a common ancestor [312].

On a functional level, G-proteins are generally active in the GTP state, and

are often deactivated by GTPase-Activating Proteins (GAPs). The GAP can be the target protein itself, as in the case of EF-Tu and its ribosome target [280], or a distinct regulatory protein, as in the case of the Ras family of proteins [27]. In the case of the GAP as substrate, it is often the case that the GTPase dissociates from the target once hydrolysis has returned the G-protein to its inactive state. The nucleotide is subsequently exchanged, generally through a Guanidine nucleotide Exchange Factor (GEF), to restore the G-protein to its active state. The motors myosin and kinesin work similarly, but the track, actin in the case of myosin and microtubule in the case of kinesin, acts as both the GAP and GEF. Nonetheless, it can be said in analogy to G-proteins that these motors also attached to their respective tracks when bound to ATP (instead of GTP), and dissociate once hydrolysis has occured (reviewed in [312, 316]).

Processive single-molecule motility sets kinesin-1 and myosin-V apart from the other motors, and this mechanism has generated substantial interest [11, 14, 95, 241, 264, 266, 315, 336, 343]. Despite extensive research, however, the detailed mechanism of force generation in many motor kinesins is not fully understood.

Since the discovery of *Saccharomyces cerevisiae* [206] and *Aspergillus nidulans* [69] kinesin genes with 30-40% sequence identity to the *Drosophila melanogaster* kinesin-1 motor core, but without significant homology outside the core domain, a "kinesin superfamily" has emerged. The members of this family are unified by the similarity of the core domain, but the kinesin core appears to have been adapted to perform tasks different from the original motor function. The next section will give a brief overview over the kinesin superfamily, with focus on how the basic kinesin core is used in various cellular functions.

The Kinesin Family of Proteins

During the early 1980's, studies of organelle transport in the central nervous system highlighted the critical role of protein motors, which transport organelles between the cell body and the synaptic terminal of neurons [5, 23]. In humans, the distance between the cell body and synapse can be on the order of 1 meter, and the simple diffusion of organelles and small molecules cannot be used to supply the synapse adequately. Active organelle transport by protein motors, therefore, allows such extended cellular structures to be maintained and organized. The two principal motors in this context are kinesin and dynein [3].

Kinesin-1 (conventional kinesin) was first described in 1985 as a microtubule-dependent ATPase activity found in the cell extracts from neurons [22, 318]. The early discovery that kinesin forms a rigor complex with microtubules in the presence of AMP-PNP [187] stood in contrast to the nucleotide cycles of dynein [195] or myosin [92], which dissociate in the presence of ATP or ATP analogues. Moreover, this discovery allowed the straightforward purification of kinesin from crude brain extracts by successive cycles of binding to and unbinding from microtubules [318]. The ability to easily express and purify kinesin proteins has contributed much to the rapid expansion of the field.

The kinesin superfamily now consists of a large number of members with widely differing cellular functions. They can be found in all organisms characterized to date and range from microtubule-regulating proteins such as kinesin-13 [213, 246, 269] to the motor proteins that originally gave the kinesin family its name. It is likely that kinesins evolved from motors that segregated chromosomes in unicellular organisms to general transport machinery engaged in the ferrying of organelles and membranes, ciliary motility, as well as the regulation of their microtubule track [314].

Over 90 kinesin sequences have been discovered to date, and most of these fall in three categories, based on the position of the motor core within the sequence

(reviewed in [314]), with the rest termed *orphan* kinesins. The three categories are illustrated in Figure 1.3 on page 49. The majority of the motor kinesins (kinesin families 1 to 12), including the original motor kinesins (kinesin-1), are classified as *KIN N*, as the enzymatic core is found at the N-terminal end of the protein. In contrast, *KIN C* motors (kinesin-14 family) carry the motor domain at the C-terminal end, and *KIN I* motors (kinesin-13 family) have an internal motor domain. The general organization of the domains in the functional motor is illustrated using the *KIN N* motor kinesin-1 in Figure 1.4 on page 50.

Generally, *KIN N* kinesins are motors that move towards the plus-end of microtubules, while *KIN C* kinesins move towards the minus-end. The *KIN I* kinesin does not move along microtubules, but instead uses the force-generating capability of the kinesin core to depolymerize microtubules [213, 229, 246, 269], thereby perfoming an important function in the regulation of cellular microtubule dynamics [212, 284].

Interestingly, kinesins share high structural similarity and are thought to share a common mechanism of force transduction, even though some translocate along the microtubule in opposite directions from others, while others do not translocate at all. For example, the plus-end directed kinesin-1 motor (conventional kinesin) and the minus-end directed kinesin-14 (*ncd*) motor share 40% sequence identity of the motor core.

It is worth noting in this context that the most class-specific part of the kinesin sequence is not the motor core, but rather the neck region linking the enzymatic core to the rest of the protein [314]. In fact, a phylogenetic tree constructed using the roughly 40 residues of the neck sequence largely agrees with a similar tree based on the approximately 330 residue motor core, suggesting that these two modules have evolved together [314]. In *KIN C* and *KIN I* kinesins, the neck is N-terminal to the core, while in *KIN N* kinesin it is C-terminal.

Kinesins and disease

Given the importance of motors for organelle transport, it is expected that anomalies in motor function lead to disease. This should be true especially in cases where only motors can travel large distances, such as axonal transport. However, only very limited data is available on kinesin-related diseases (reviewed in [200]). One of the more prominent kinesin-related pathologies is *situs inversus*, in which the position of organs along the left-right axis is inverted. Knockout studies in mice showed that this phenotype is due to a disruption of nodal flow during gastrulation, which leads to randomization of the left-right axis. $KIF3^{-/-}$-mice have embryonic defects in the generation of nodal cilia, which are essential for the nodal flow that determines left-right asymmetry [201, 224]. Furthermore, KIF3 is involved in early patterning and neurogenesis, as KIF3 knockout mice display severe developmental phenotypes that are lethal at the embryonic stage [290]. Other kinesins have also been found to play crucial roles in embryogenesis and cell maintenance. Knockouts of KIF5 show abnormal clustering of mitochondria and lysosomes and are also embryonic lethals [291]. Taken together, these data suggest that kinesins are required for normal cell function, not only in highly elongated cells such as neurons that depend on motors for long-range transport, but also in more globular cell types.

Nonetheless, the study of kinesins may well hold a promise for medical applications. Due to the intricate involvement of kinesins in processes such as mitosis, it may be possible to develop drugs that specifically target dividing cells, either by disrupting chromosome segregation, or by targeting the microtubule cytoskeleton. The natural compound *adociasulfate-2* from a marine sponge has been found to block kinesin-dependent motility and mitosis [261]. Other potential kinesin inhibitors have been developed using structure-based computer screening, of which several hold promise as drugs [131]. Furthermore, the drug *monastrol*, an inhibitor of the mitotic spindle kinesin Eg5, causes the formation of monopolar asters and blocks cell division [153] and is now widely used in research applications. Lastly,

the local anesthetic *lidocaine* was found to block axonal kinesin-dependent traffic. Interestingly, however, *lidocaine* does not affect the ATPase activity of kinesin, but rather appears to block the coordination between the catalytic heads [210]. While the main mechanism of action of *lidocaine* is the suppression of action potentials through membrane stabilization (reviewed in [30]), it is possible that transient neurological symptoms after *lidocaine* administration [150, 233] are partly due to the effect of the drug on kinesin motility.

Aside from inhibiting the function of motor kinesins, further promise may be held in drugs that affect regulatory kinesins. The mitotic anti-cancer drugs *taxol* and *nocodazole* disrupt the dynamics of the microtubule cytoskeleton by stabilizing and destabilizing, respectively, microtubules. A more specific mitotic drug could possibly be developed that targets microtubule-depolymerizing machines of the kinesin Kin I type, such as the mitotic centromere-associated kinesin-13 (MCAK). Kinesin-13 and other microtubule regulators have been shown to be important for microtubule remodeling during mitosis [61], and potential benefits could be gained from specifically targeting microtubule regulators enriched in mitotic cells, rather than the more ubiquitous microtubule cytoskeletal components.

The mechanism of kinesin-1 motility

Molecular organization and regulation of the kinesin-1 motor

The molecular organization of kinesin-1 was established in 1989 and showed the globular N-terminal catalytic domains of the kinesin dimer as well as the extended coiled-coil domains [119, 325]. Based in part on these structures, a model for the organization of kinesin-1 was proposed. Kinesin-1 exists as a heterotetramer of two heavy chains and two light chains. The heavy chains contain two identical "heads" of approximately 45 kDa at the N-terminus that form the catalytic core of the motor. These are followed by an extended coiled-coil domain that forms the dimerization domain and links the heads to each other as well as to the cargo. At the C-terminal of the coiled-coil dimerization domain are the light chains with binding sites for adapter molecules, which allow kinesin to dock to and transport different cargoes (reviewed in [151]). A schematic of the organization is shown in Figure 1.4 on page 50. While the details for the organization of other kinesin family members vary, the overall configuration of a coiled-coil domain linking catalytic heads to the cargo is found for several motor kinesins that form higher order structures (reviewed in [314]).

In addition to linking the force-producing domains to the cargo, the coiled-coil domain has been found to contribute to kinesin regulation. When kinesin-1 is inactive in solution, the kinesin tail binds to the heads and inhibits the release of ADP [45, 78, 103, 105, 106, 283, 323]. For this, it is necessary that the coiled-coil domain be foldable to allow the tail domain to contact the catalytic heads. Indeed, several "hinges" that disrupt the coiled-coil structure have been found within the dimerization domain [119, 220, 337]. These hinges contain prolines and glycines and give the motor domains considerable torsional flexibility with respect to the cargo [133]. This flexibility allows kinesin to swivel independently of the attached cargo

without losing any significant speed [138], but also makes it possible for the long neck domain to fold and bring the inhibitory C-terminal domains in contact with the heads (reviewed in [99]). Although the hinges are not a general feature of kinesins, several N-type kinesin do have them, and hence hinges may be a class-specific feature [314].

Architecture of the kinesin catalytic core

The first structures of kinesin catalytic domains in complex with microtubule were published in 1995 in three back-to-back articles, and highlighted the remarkable similarity of the head domains of kinesin-1 [122, 166], and the minus-end directed kinesin-14 [128].

Kinesins are characterized by a catalytic motor core of α/β architecture with a central β-sheet domain of eight strands with three α-helices on either side of the sheet. The helices are involved in microtubule binding, and power transmission, while several of the loops between secondary structure elements are involved in nucleotide binding and sensing [184, 257].

Structurally, the N- and C-terminal extensions of the kinesin catalytic core are located on the same side of the core, and run in parallel strands about 7 Å apart [215, 306]. Furthermore, they are both close to the switch II helix that senses the nucleotide state and relays the information to the neck region (see Figure 1.1 on page 47 for details). The similar architectures of the catalytic domains of the plus-end directed kinesin-1 and the minus-end directed kinesin-14 motors are shown in Figure 1.5 on page 51. In both cases, the motor core is closely connected to the coiled-coil *neck* region that also forms the dimerization domain. However, the C-terminal extension from the core of kinesin-1 forms a 13 residue linker region, called the *neck linker*, that connects the catalytic core to the *neck* domain and can detach from the core [285], while in kinesin-14 the N-terminal extension forms the neck coil with only a few intervening residues.

The directionality of kinesin movement was found to be related to the neck region, not the motor core itself [115, 117]. In fact, it has been shown that a chimeric motor with the neck region of (plus-end directed) kinesin-1 with the motor core of (minus-end directed) kinesin-14 (*ncd*) retains the directionality of kinesin-1 [35]. This finding suggests that motor kinesins are likely "geared" differently, while sharing the same "engine" core [36, 66, 67].

Models for kinesin motility

Kinesin-1 is a "molecular walker" [10, 343] that steps 8 nm from one tubulin dimer to the next along its microtubule track [152, 241] and hydrolyzes 1 ATP per step [46, 47, 71, 265, 289, 324]. In this manner, a single kinesin dimer can take hundreds of steps and cover distances in excess of 1 μm without release from the track [97, 315]. The ability to take many steps without release from the track has been termed "mechanical processivity" [163] and distinguishes kinesin from dynein and most myosins, which are generally not considered to be processive [99], although some evidence to the contrary has emerged recently [84].

In its minimal configuration for processive motility, the kinesin-1 motor consists of a dimer of catalytic heads, connected to each other and the cargo through the extended coiled-coil domain. The kinesin dimer has been found to move linearly along the ridge of a single protofilament of its microtubule track [130]. Such movement is consistent with at least two different modes of motility, commonly referred to as the *"hand-over-hand" model* and the *"inchworm" model*. These models are compared in Figure 1.6 on page 53.

The *hand-over-hand model* is analogous to the walking of *bipeds*, such as humans [10]. Nonetheless, the term *"hand-over-hand"* is preferred in the literature over *"walking"*, because the effect of gravity at the molecular scale is very small, and it is therefore necessary for molecular motors such as kinesin to attach to, and detach from, their respective tracks. In this sense, it is more appropriate to compare

this mode of stepping to a person hanging from and moving across a rope streched between two anchor points and moving *"hand-over-hand"*, putting one hand in front of the other. Nonetheless, referring to the model as *"walking"* may be more intuitive and is equivalent except for the complication mentioned. The *hand-over-hand model* implies the following mechanistic details:

First, during each step, one catalytic head (or foot in humans) is stationary, while the other moves.

Second, the heads exchange positions during each step. Each head therefore alternates between leading and trailing, as well as moving and stationary.

Third, any given binding site will be used by only one of the heads, and the same binding site will be skipped by the other head.

Furthermore, it should be noted that the kinesin heads in a homodimer are equal, rather than having mirror-symmetry like hands or feet. While this led to early expectations that the movement of the heads be symmetric as well, such models have been ruled out [116, 134], and there appears to be general agreement in the field that kinesin-1 moves by an *asymmetric hand-over-hand* mechanism [11, 116, 267]. While this observation could potentially create an additional complication of the model, it will be evident later that the basic features of the proposed model are not significantly affected.

The *hand-over-hand* model directly contrasts with the *"inchworm" model*, which has also been used to explain kinesin motility [134, 288]. In this model, motility is analogous to the movement of caterpillars or centipedes, which propel themselves forward by successively extending the front of their bodies forward and retracting the rear. This model is characterized by the following features:

First, both of the heads move sequentially during the step; each step is therefore composed of two substeps.

Second, distinct leading and trailing feet that do not exchange positions.

Third, each binding site is used by both heads in succession.

Despite the early controversies, much evidence suggests that kinesin-1 moves by the *asymmetric hand-over-hand* mechanism [11, 116, 264, 266, 343] and the heads alternate at each step [95, 113, 155, 267, 276]. Nonetheless, evidence exists that favors the *inchworm* model, particularly under high loads [266].

Regardless of the mechanistic model, given the molecular architecture of kinesin with two connected catalytic heads, the ATPase cycles of the heads must be coordinated for the motor to be processive, such that only one of the heads can be detached at any time during processive movement. The heads, therefore, must communicate. Such communication should serve the purpose of stalling the ATPase cycle of the stationary head until the moving head has completed its step (reviewed in [102]).

To understand the mechanism of processive motility in kinesin, it is necessary to first consider how the ATPase cycle of each head is related to the microtubule binding and unbinding events, as well as to the structural changes that lead to force production.

Biochemical characterization of the kinesin ATPase cycle

Each head in a kinesin dimer can exhibit microtubule-stimulated ATPase activity, and can bind to and unbind from the microtubule, but monomers of kinesin-1 are not processive [14, 83]. This is in contrast to the monomeric kinesin KIF1A, which is believed to be processive [226], but uses two different loops on the motor core alternately to stay attached and move diffusively along the microtubule surface [223, 225, 227]. Nonetheless, the ATPase cycles of monomeric and dimeric kinesins are related to the microtubule binding/unbinding cycles as well as force-producing structural changes in similar ways.

We propose the simple model shown in Figure 1.7 on page 54 for a full nucleotide cycle of kinesin. Important features of the model are a) the coupling between nucleotide state and microtubule attachment/detachment, and b) the existence of weakly and strongly bound states with respect to microtubule. An important caveat not conveyed by the model is that individual kinesin heads can hydrolyze multiple ATP molecules in a single microtubule encounter (i.e. without release from the microtubule) [135, 148, 198]. The ability to hydrolyze multiple ATP molecules without release from the track has been termed *"kinetic processivity"*, and is in contrast to the *"mechanical processivity"* term used earlier to define the ability to take many steps along the track without release of the motor. Thus, while even individual heads of kinesin-1 have limited *"kinetic processivity"*, they are not *"mechanically processive"*. Rather, they transition between strong and weak binding states on the microtubule while undergoing futile ATPase cycles. The relationship betweeen the two types of *processivity* will be discussed in more detail in section The two-head bound state starting on page 35.

The following reaction rates and binding constants directly relevant to the kinetic mechanism of kinesin processivity have been determined for *monomeric* kinesin motor domains ($\circ$ denotes the bound state):

ADP release in absence of microtubule

$$K_{head} \circ ADP \overset{k_1}{\rightleftharpoons} K_{head} + ADP \tag{1.1}$$

with $k_1 = 0.02\ s^{-1}$ [135, 198]

microtubule-stimulated ADP release

$$K_{head} \circ ADP + MT \overset{k_2}{\rightleftharpoons} K_{head} \circ MT + ADP \tag{1.2}$$

with $k_2 = 150 - 300\ s^{-1}$ [198, 217]. Note that release of ADP occurs in a two-step process (binding of $K_{head} \circ ADP$ to microtubule, and release of ADP

from $K_{head} \circ ADP \circ MT$) and the rate given is for the entire process.

binding to microtubule in presence of excess ADP

$$K_{head} \circ ADP \circ MT \overset{K_{d,MT}^{ADP}}{\rightleftharpoons} K_{head} \circ ADP + MT \tag{1.3}$$

with $K_{d,MT}^{ADP} = 16 - 22\ \mu M$ [198, 335], with a rate of head dissociation $k_{off} = 75\ s^{-1}$ [198]

ATPase in absence of microtubule

$$K_{head} \circ ATP \overset{k_{cat}}{\rightleftharpoons} K_{head} \circ ADP + P_i \tag{1.4}$$

with $k_{cat} = 0.029\ s^{-1}$ [135]

microtubule-stimulated ATPase

$$K_{head} \circ ATP \circ MT \overset{k_{cat}^{MT}}{\rightleftharpoons} K_{head} \circ ADP \circ MT + P_i \tag{1.5}$$

with $k_{cat}^{MT} = 60 - 80\ s^{-1}$, $K_{0.5,ATPase}^{MT} = 160\ nM$ for half-saturation of the ATPase rate by microtubule at saturating ATP levels, $K_{0.5,ATPase}^{MT} = 43\ \mu M$ for half-saturation of the ATPase rate by ATP at saturating microtubule levels, and $K_{0.5,binding}^{MT} = 400\ nM$ for half-saturation of kinesin binding to microtubules at saturating ATP levels [135, 198].

microtubule-stimulated ATP hydrolysis

$$K_{head} \circ ATP \circ MT \overset{k_{hyd}}{\rightleftharpoons} K_{head} \circ ADP \circ P_i \circ MT \tag{1.6}$$

with $k_{hyd} = 200\ s^{-1}$. Release of P_i is at least as fast as hydrolysis and therefore essentially irreversible [135, 198].

binding constant for ATP-like state

$$K_{head} \circ ATP_{analog} \circ MT \overset{K_d^{MT,ATP_{analog}}}{\rightleftharpoons} K_{head} \circ ATP_{analog} + MT \tag{1.7}$$

with $K_d^{MT,ATP_{analog}} = 1-7\ \mu M$ [198]. Note that due to steady-state ATP hydrolysis, this is significantly different from the apparent dissociation constant in the presence of excess ATP, measured at 9 μM [198]

binding constant for apo (no nucleotide) state

$$K_{dimer} \circ MT \overset{K_d^{MT,apo}}{\rightleftharpoons} K_{dimer} \circ + MT \tag{1.8}$$

with $K_d = 3\ nM$ [48]. This rate has been determined only for the dimer, but other experiments have shown that a dimer with both heads attached to the microtubule and deviod of nucleotide is unlikely for kinesin-1 [95].

The reverse rates are not shown here, and for most cases they are very small [94]. Other combinations of reactions and states are possible, but unlikely to be encountered physiologically. For example, it is possible to produce nucleotide-free kinesin in the absence of microtubule, but this state tends to destabilize kinesin, reform the bound ADP slowly ($t_{1/2} \geq 10\ min$) in the presence of MgATP [135], and is therefore unlikely to be encountered physiologically [106, 135]. On the other hand, it is worth noting that two distinct conformations may exist for the ADP-state of kinesin bound to microtubule, a weakly-bound state that can dissociate, as well as a state attached more strongly that likely leads to nucleotide ejection [198]. However, it has been challenging to separate these states experimentally, and rates are generally given for the combined process [198].

To produce motility in the dimeric motor, the nucleotide states need to be coordinated between the two heads of the dimer. Of particular importance to *mechanical processivity* is that weak binding states should not occur simultaneously to

prevent premature release of the motor from the microtubule. A model of how the heads are coordinated is the focus of the next section.

Coordination of the step

The coordination of kinesin stepping is achieved by keeping the ATPase cycles of the heads out-of-phase. Several studies have suggested that ADP is released from only one head upon binding of dimer kinesin to microtubule, whereas the other ADP is released too slowly to contribute to the main kinetic pathway [95, 100, 197]. This state is thought to essentially constitute an "ATP waiting state", during which only one of the heads is strongly attached to the microtubule. At this point, it is unclear what this waiting state looks like [34]; several studies have suggested that the tethered head is detached from the microtubule during the wait [157, 214, 327], possibly attached to the bound head [6] or free to diffuse within the reach of the tether [33, 34], while others contend that kinesin waits with both heads attached to the microtubule [341, 343].

Regardless of the waiting state structure, it is clear that ATP binding at the attached head commits the motor to stepping and gates release of ADP from the leading head [49, 264]. A model of a single step is shown in Figure 1.8 on page 56. ATP-induced attachment of the leading head is thought to occur very fast ($> 2000\ s^{-1}$), followed by slower release of ADP from the leading head [49]. The result is that kinesin is transiently attached by both heads to the microtubule in the presence of ATP [214] or ATP analogs [157]. In this state one head is bound to ATP, while the other has no nucleotide, and is therefore strongly attached (see section Biochemical characterization of the kinesin ATPase cycle on page 29 for details on the binding constants). This stepping event closes the nucleotide pocket of the trailing head and commits it to ATP hydrolysis [164, 218, 219]. At the same time, ATP cannot bind to the leading head until the trailing head has completed hydrolysis ($k_{ATPase} = 60 - 80\ s^{-1}$ [135, 198]) and detaches [141, 181, 250]. Hydrolysis of

ATP and release of P_i at the trailing head reverts it to the weakly bound ADP state [101], and detachment of the trailing head completes the cycle, with the heads having switched places. This mechanism, essentially, keeps the nucleotide cycles of the two heads out of phase by coupling the release of the attached head (by ATP hydrolysis) to the attachment of the tethered head (by ADP release) [102].

In summary, coordination is achieved by stalling the nucleotide cycle in one head until the other head has completed a "checkpoint" conformational change. For the leading head, nucleotide binding is stalled until the trailing head is dissociated by ATP hydrolysis. For the trailing head, ATP hydrolysis is delayed until the leading head is attached at the forward binding site. In this model, *mechanical processivity* is principally limited by the binding and hydrolysis of ATP at the bound head before the tethered head has completed its step and is strongly attached. How the probability of this event is significantly reduced through coordination and passage through a two-head bound state is the focus of the following chapters.

The two-head bound state

The key requirement for processivity in this cycle, as implied by the *hand-over-hand* model, is the two-head bound state during which the heads exchange positions. In the absence of a two-head bound state, the motor could completely dissociate from the track and diffuse away. Indeed, Hackney has reported that premature ATP hydrolysis in the attached head before the tethered head attaches to the microtubule leads to the detachment of kinesin [100]. The two-head bound state is important to two theoretically unrelated problems concerning kinesin motility:

Entry into this state governs *mechanical processivity*, the ability to complete consequtive steps without detachment from the track.

Exit from this state governs the *coupling ratio* of the nucleotide cycle to a step, defined as the number of ATP hydrolyzed per step. *Coupling* is sometimes measured in the literature as the *duty ratio* of the motor [81, 231, 237, 347] and

is related to the number of futile hydrolysis cycles of the motor, i.e. nucleotide cycles that do not lead to a step.

The problem of *mechanical processivity* has received clearly more attention in the field than that of *coupling*, although details of the latter are beginning to emerge as well. Consideration of the problem of coupling deserves special attention, because some kinesins, e.g. the monomeric kinesins such as KIF1A are believed to be *mechanically processive* despite low duty ratios [226, 347]. The work presented in this document deals mostly with the problem of *mechanical processivity*, but because *coupling* and *mechanical processivity* may be tighly linked in kinesin-1, *coupling* will be given some consideration as well.

From the observation that kinesin hydrolyzes 1 ATP per step and can cycle repeatedly without falling off the track, it is clear that both entry to and exit from the two-head bound state are tightly gated and segregated. The two-head bound state itself may be rather short-lived (approximately 100 μs) [142]), due to two fast and essentially irreversible *gating* steps that control entry to and exit from this state. As shown in Figure 1.8 on page 56, entry to the state is gated by ADP release, while exit from the state is induced by P_i release. Contrary e.g. to the waiting state described earlier, which could have several distinct conformations, this state is well defined and forms a "choke point" along the pathway through which kinesins moving processively in either direction must pass [34, 93, 222]. Therefore, detailed knowledge of this state can provide direct evidence of the coordination of the heads.

Gating the kinesin step

Increasing evidence suggests that strain plays an important role in the maintenance of the difference in nucleotide states between the heads [49, 93, 107, 141, 250, 342]. Several groups have studied the effects of strain on kinesin motility. Earlier studies suggested that motility of the dimer kinesin is not significantly affected by forward or sideways load, but that large backwards loads stall the motor [17].

Subsequent studies found that the stall force of the dimeric motor depends on the concentration of ATP in the buffer, and that the load acting on the motor must therefore affect the binding of ATP [324]. Indeed, theoretical models as well as experimental evidence suggest that release of the motor from microtubule after ATP binding is significantly faster when a forward load is applied as than when the motor is loaded in the backward direction [74, 308], but that stepping in both directions requires ATP [222], presumably because attachment and release events in both directions are subject to the same gating mechanisms [34, 73]. In contrast, there is no evidence for sideways stepping [241], even under loads applied sideways [17, 73].

Subsequent studies have helped elucidated the structural basis of strain-dependent motility. On one hand, inter-head tension has been implicated in the gating of nucleotide binding to the leading head. Indeed, Rosenfeld and co-workers found evidence that the major effect of strain between the heads is to prevent ATP binding to the leading head [250]. In support of their data are single molecule experiments performed on single kinesin heads, showing that the affinity of the kinesin head for ADP is approximately 7-fold higher when the motor is pulled forward, rather than backward ($\sim$13 vs. $\sim$90 μM, respectively) [307]. Furthermore, when AMPPNP, an ATP analog known to induce a strong binding state in kinesin ($K_d \approx 42\ nM$ [44]), binds to the motor during processive motility, a terminal backstep is required before processive motility can resume [93, 327]. These observations, as well as a theoretical model suggesting that 12-15 pN of strain on the lead head disrupts its ability to bind nucleotide [141], strongly suggest that nucleotide binding to the leading head is gated by backward strain.

On the other hand, strain on the trailing head has been implicated in "trapping" ADP after hydrolysis [52, 307], thereby preventing reversion to the strongly bound apo state. Further experiments have suggested that forwards-directed tension accelerates trailing head release [49, 335], and that an externally imposed forward pull on the motor can restore processive motility to motors otherwise unable to move

efficiently either by extended neck linkers [342], or by mutation of the neck linker attachment site on the motor core [161]. These observations are also consistent with a proposed mechanism by which ADP release is a force-producing event [116] and allows dimers to take one step per ATP hydrolyzed [46, 47, 71, 265, 289, 324], as compared to single heads that hydrolyze on average four ATP before release [148, 198].

It follows from these observations that both *processivity* as well as *coupling* of kinesin dimers should significantly decrease if strain between the heads is decreased. Indeed, biochemical as well as structural evidence shows that relieving the tension on the neck linkers leads to defects in normal motility. Hackney and co-workers showed that extension of the neck linkers by insertion of additional residues leads to a loss of *kinetic processivity* in kinesin-1 [107]. Specifically, microtubule-stimulated half-site release of wild-type kinesin [95, 100, 149] is severly disrupted in constructs with 6 or more additional residues in the presumably unstructured part of the neck linkers [107]; instead, such constructs release all of their bound ADP upon microtubule addition, suggesting that their cycles are no longer out-of-phase [107]. The resulting decrease in *kinetic processivity* is approximately 2-fold for a single amino acid insertion, and 3- to 4-fold for 6 to 12 residue insertions [107, 141].

A single-molecule study using similar constructs, however, found that the decrease in *kinetic processivity* (the ability to complete several nucleotide cycles in a single diffusional encounter with a microtubule [98]) due to the insertion of additional residues in the neck linker does not necessarily lead to a corresponding decrease in *mechanical processivity* (the ability to take many steps before falling off the track [156]). Instead, the authors found a decrease in *coupling* of ATP hydrolysis to stepping, thereby greatly increasing the number of futile hydrolysis events and decreasing the motor velocity [342]. While the non-direct relationship may seem surprising at first, it should be recognized that individual heads under zero-load condition can hydrolyze several ATP before release from the microtubule

[148, 198], and are therefore *kinetically processive*. It is therefore possible that the uncoordinated attachment/release of two heads keeps the dimeric motor attached to the microtubule. An applied backward load increases the resistance to detachment of the motor, because backward loads prevent nucleotide binding, as mentioned previously. A load in the forward direction (towards the microtubule plus-end), on the other hand, restored velocity to the extended mutants [342], suggesting that strain may be as important to *coupling* as it is to *processivity*.

The possibility of a strain-dependent mechanism raises the question of where strain can develop and how it can be propagated to coordinate the heads. The most likely structures to strain across the heads are the neck linkers connecting the heads to each other as well as to the cargo. The neck linker has been implicated in force generation as well as head coordination. To gain a better understanding into the mechanism of the kinesin walk, the next section will take a look at the structural basis underlying the kinesin step.

The structural basis kinesin-1 motility

As mentioned in section Models for kinesin motility starting on page 27, it is now generally accepted that kinesin-1 moves by the *asymmetric hand-over-hand* model. By using this mechanism, a single kinesin can move in 8 nm steps against a load of $5-8$ pN [18, 118, 132, 289, 315, 338], at a velocity of approximately $0.8-1$ $\mu M/s$ [109, 156, 287, 325], and it can do so hundreds of times before release from the track, thereby covering several hundreds of nanometers [97, 315].

In light of the *asymmetric hand-over-hand* model, it is clear that the ATPase cycles of the heads must be tightly coordinated to achieve the observed processivity, as even small deviations from ideal kinetics would exceed the 1% observed release probability [315]. To discuss models of how processivity could be achieved, it will be crucial to study the structures of dimer kinesins capable of processive movement in complex with microtubule, and to distinguish each head based on its nucleotide

state and/or position with respect to the other head or cargo. To this end, it is necessary to consider in detail the conformational changes that occur within the catalytic core upon changes in nucleotide state. These changes are observable in constructs lacking the dimerization domain, and the focus of the next sections will be on their potential contribution to the mechanism of processivity.

Much of the research on kinesin so far has focused on conformational changes, associated with the nucleotide cycle, that are involved in the force-generating powerstroke. The *neck linker*, the presumed force-producing element in *N-type* kinesins [245] is highly conserved, with the consensus sequence $K/RxIxNxxxV/IN$ for the first 10 residues, where x can be any residue [215, 306]. The *neck linker*, starts at the end of helix $\alpha 6$ as it emerges from the motor core and ends at the neck coiled-coil, where the next 30 residues form a highly stable α-helical coiled-coil [314] that is not likely to be involved in motility [300]. The neck linker is shown docked to the motor core in red in Figure 1.1 on 47, while the neck coiled-coil is colored blue.

The coiled-coil *neck* region contains a $\phi - xx(x) - \phi - xxx - \phi - xx - \phi$ motif, where ϕ is hydrophobic and highly conserved [314], and forms part of the kinesin-1 dimer interface [215, 306]. Approximately seven helical turns of the coiled-coil domain are required for dimerization [136, 306, 346], and a construct of this length possesses all the biochemical features of the full dimeric motor [149]. It is also noteworthy that dimerization is tight [346] with $K_d \approx 37\ nM$ [216], despite the relative shortness of the coiled-coil compared to full-length kinesin. Furthermore, the base of the coiled-coils in a dimer can be cross-linked without a loss of motility or processivity, and it has been concluded that unwinding of this region is therefore not essential for motility [247, 300]. Given these observations, the neck linkers can be regarded as a spacer of fixed length connecting the catalytic domains. This may have important ramifications for motility, as discussed below and in later chapters.

Many conformational transitions in proteins, including the ones described in the following section, take place simultaneously, or nearly so, and may not be

separable experimentally. Nonetheless, for the purposes of this discussion, structural transitions will be treated in a modular fashion with particular focus on their possible contribution to the mechanism of processivity.

The kinesin "power-stroke" model

Besides connecting the catalytic heads to each other as well as to the cargo, the neck linker has been implicated in force transduction [245], although the details of is transduced is still under investigation. The neck linker has been proposed to execute a "powerstroke" and thereby "drive" kinesin motility [12, 36, 244, 245, 251, 270, 271, 313], by transitioning from a disordered state in the ADP and apo states [184] to being closely aligned with the side of the head in the ATP-like state, where it can form a short β-sheet with the motor core [258, 270, 313]. In the original model for kinesin motility, this powerstroke, executed upon ATP-binding, was proposed to "fling" the rear head forward to the next binding site, thereby advancing the cargo by 8nm [245, 316]. Consistent with this model is evidence that the neck linkers of the heads in a dimer bound to microtubule by both heads are relatively static [285] and pointed in opposite directions: backwards (towards the minus-end) on the leading head and forward (towards the plus-end) on the trailing head [272, 316], and further, that they change positions during motility [299].

The details of the powerstroke are still under investigation. Given the disordered structure of the neck linker when it is undocked from the motor core, it is unlikely that it acts like a rigid lever arm [144]. Instead, it has been proposed that the neck linker "zippers up" against the head upon ATP binding [51, 204, 244, 247]. What drives the "zippering" of the neck linker is also debated at this point, but newer evidence suggests that dynamic "folding" events at the periphery of the kinesin core are involved [140, 161].

The Brownian ratchet model

Earlier models for kinesin motility implied that the energy derived from ATP binding to the motor core is mainly responsible for driving the docking of the neck linker. However, studies of the thermodynamic properties of neck linker docking have shown that the free energy change release during neck linker docking is too small to account for kinesins ability to step 8 nm against loads of 5-6 pN [244]. Newer models have been put forth in which movement is driven by rectified Brownian motion [43, 137, 145, 204, 221, 222].

Similar models were originally proposed by Huxley for myosin [139], well before structural details of myosins were available, and operate analogous to Feynman's *"thermal ratchet"* model [72], where movement is driven by Brownian thermal fluctuations [234], but directionality is imposed by a thermal barrier against stepping backwards [317]. Such models for kinesin imply that the energy for stepping, i.e. for the movement of the (detached) trailing head to the next binding site are driven by Brownian motion [145, 222, 292], but backstepping is prevented by a "latch" mechanism [204], perhaps the stability of the interaction between the motor core and the docked neck linker. However, such models will have to be evaluated experimentally, with particular attention as to what could constitute the "latch" against backward stepping.

Towards Unraveling Processivity

As mentioned previously, each head is potentially capable of independent nucleotide cycling with attendant binding/unbinding to/from microtubule. However, kinesin's ability to take hundreds of steps [97], with a release probability of $\leq 1\%$ [315] at each step, strongly suggests that the nucleotide cycles of the heads are coordinated, a notion that has been confirmed experimentally [95, 96, 154, 198]. While the general mechanism and structural basis for kinesin *motility* have been extensively studied and seem well-understood, the corresponding mechanism and

structural basis of *mechanical processivity* are still being debated.

Many studies agree that the conserved, class-specific neck linker is important for coordination of the heads, but it is not clear in which way it coordinates stepping. As described in the previous sections, the neck linker may execute a powerstroke-like action to advance the trailing head to the next binding site [245, 316], or the trailing head may advance by Brownian motion [145, 204, 222, 292]. However, neither model addresses how attachment of the leading head precedes detachment of the trailing head, a key requirement for processivity.

As mentioned in section Gating the kinesin step on page 36, the coordination between the heads partly hinges on the generation of strain during motility. The most likely path to transmit strain to the heads is across the neck linkers, as they make the only direct connection between the heads when both motors are attached to the microtubule. Furthermore, as the neck coiled-coil is highly stable and unlikely to unwind during motility [247, 300], it is possible that the neck linker can be regarded as a rope. This idea is consistent with evidence that the neck linker can be disordered when not docked to the core [285], The rope-like neck linker can thus transmit tension from the cargo or the partner-head to either of the heads in the dimer, and thereby coordinate the nucleotide-induced conformational changes through a steric feeback mechanism. To investigate how the strain transmitted to the heads could affect the ATPase cycles of the heads and keep them out-of-phase, the structural changes that occur within heads during motility have to be considered. These changes will be outlined next.

The nucleotide-switch of kinesin

High-resolution structural evidence for nucleotide-induced conformational changes of microtubule-bound kinesin-1 is limited, but the structure of the monomeric kinesin *KIF1A* in complex with microtubule has been solved to resolutions better than 20 Å, both in the ADP- and ATP-like states [164, 167, 168]. These struc-

tures show that kinesin adopts a conformation closely aligned with the microtubule protofilament axis when bound to ATP, while it is "rolled" clockwise (similar to the (coordinated) turning of an airplane in flight) when complexed with ADP, and appears "tilted" clockwise when looking perpendiculary from the outside of the microtubule. In each case, the switch II region (helices α4 and α5, and loops 11-13) has been found to be stationary with respect to the microtubule, so that the bulk of the kinesin core rotates clockwise roughly around its long axis by approximately 20° [164, 168]. These conformations are shown superimposed on each other in Figure 1.9 on page 58. Similar predictions have been made for kinesin-1 on the basis of computer simulations, although the angle of the rotation has been predicted to be smaller [334]. Furthermore, the apo (no nucleotide) conformation of kinesin-1 has been found to adopt a position with respect to the microtubule similar to the ADP state of *KIF1A* as well [271].

The clockwise rotation of the kinesin core may be significant to the mechanism of processivity in two distinct ways. On one hand, the switch II helix prevents the neck linker from docking to the core in the "tilted" conformation [168]. On the other hand, the rotation also moves the bulk of the core towards the plus-end when bound to ATP analogs. Together, these conformational changes move the base of the neck linker connecting the heads closer to the minus-end of the microtubule in the ADP state, when compared to the ATP-like state, an observation supported by other studies [73, 121, 227]. Under the assumption that the neck linker can act as a spacer or string of fixed length, this observation may suggest that the neck linker is involved in the gating of the nucleotide binding to the lead head [6, 93], and/or may serve to pull the rear forward after ATP hydrolysis [335]. These models are decribed in more detail in section The two-head bound state on page 35.

Lastly, changes in the nucleotide binding pocket of the motor core due to nucleotide binding, hydrolysis, and release are transduced partly by the switch II helix and loop to the microtubule binding region. The result of these changes

is that when ATP is bound to the kinesin head, the microtubule binding regions form a surface largely complementary to the microtubule surface. By contrast, the microtubule binding face is predicted to be more convex when ADP is bound in the nucleotide pocket, thereby reducing the affinity of the core to the microtubule [168, 334, 335]. Despite the similar orientation of the kinesin head with respect to the microtubule in the apo and ADP states, changes in the nucleotide sensing regions transmitted to the microtubule-binding region greatly change the affinity of the kinesin head to the microtubule between the apo and ADP states. Furthermore, the ADP-bound form is thought to be highly mobile and thought to be "rocking" on the microtubule despite remaining weakly attached [278]. The ADP-bound form of the kinesin core likely occurs in the trailing head [101], and the weakening of the microtubule-kinesin interface could therefore facilitate a "powerstroke"-like action by the leading head through release of the trailing head.

The energy barrier between different conformations is likely low, and conformational equilibria between the different states, even in the absence of track polymers have been reported for kinesin as well as myosin [168, 316]. In this regard, it is noteworthy to point out that the crystal structures for human kinesin in the apo [184] and ATP-like conformations [270], as well as the rat kinesin in the ATP-like conformation [258] were all solved with bound ADP in the nucleotide pocket. It is becoming increasingly clear that the nucleotide alone does not control kinesin conformation, but that there may be a feedback between nucleotide state and structural state [108]. Is this therefore plausible that both the track and external forces (tension) can coordinate the movements of the switch elements (reviewed in [163, 256]).

The two-head bound state

As mentioned earlier, the two-head bound state likely consists of the trailing head bound to ATP, and the leading head bound to ADP (weakly attached) or

empty (strongly attached). The structure of the two-head bound state has been addressed in the literature [113, 129, 130, 272, 297], but the resolutions obtained have not been sufficient to distinguish the conformations and/or nucleotide states. To address how tension could be involved in coordinating the heads, it is necessary to compare the two-head bound state of strained dimers with that of non-strained dimers using methods with which conformational differences between the heads can be distinguished, and assess the differences with regard to processivity.

In this study, we have addressed this problem, and formulated a hypothesis for the structural basis of processivity of the kinesin-1 motor. **Based on the strain-based gating and feedback mechanism detailed in the preceding pages, we expect that the two-head bound conformation of the kinesin motor in the presence of an ATP analog is constrained by the tension acting on the neck linkers to include one ATP-like head and one nucleotide-free head. We further propose that these are distinguishable based on nucleotide-induced conformational changes similar to those seen in KIF1A.** In order to address and support our hypothesis, we have solved by cryo-electron microscopy the structures of both processive and non-processive dimeric kinesins, as well as of their constituent monomeric heads. The results are presented in the following chapters.

Figures

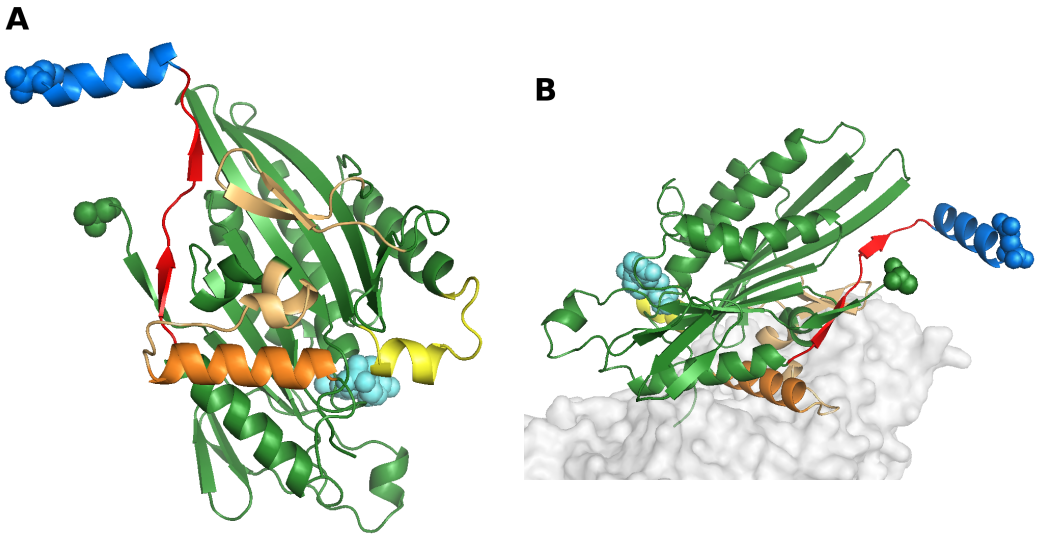

Figure 1.1 Architecture of the kinesin motor core

This figure the architecture of the kinesin-1 motor core (A) looking at the microtubule binding face and (B) looking at the right side of the molecule in the direction of movement. The microtubule plus-end is towards the top of the page in (A) and towards the upper right in (B). The N- and C-termini are shown in green and blue spacefill, respectively, and the nucleotide in light blue spacefill. In (B), tubulin has been inserted in the approximate position for reference and is shown as a grey surface. The coloring of structural elements is as follows: neck linker (red), neck coiled-coil (blue), microtubule binding regions (orange) with switch II helix colored darker, and switch I loop (yellow).

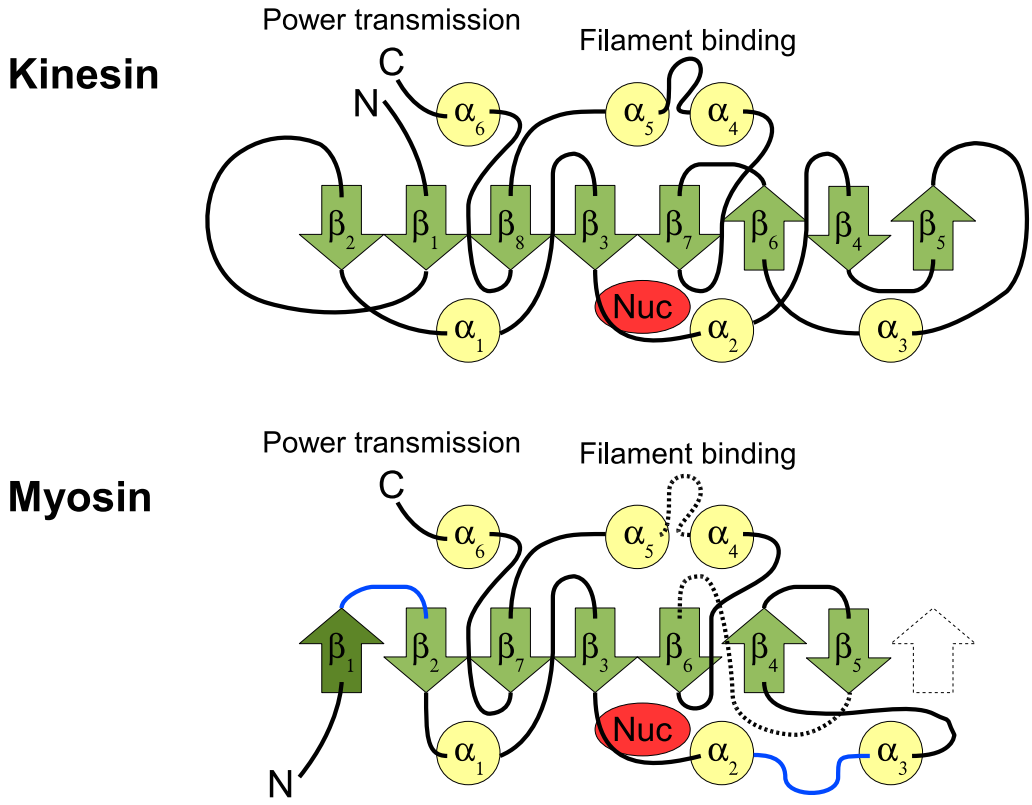

FIGURE 1.2 COMPARISON OF THE KINESIN AND MYOSIN FOLDS

The drawing shows the general topologies of kinesins (top) and myosins (bottom), as well as the connectivities of the secondary structure elements. *Arrows* represent β-sheets, *circles* represent α-helices, and the nucleotide (ATP or ADP) is shown in red. Connectivities in myosin that differ from those found in kinesin are colored blue. Note that the leftmost β-strand in myosin (darker) is reversed compared to kinesin, and the rightmost β-sheet (outline), is absent. Also noteworthy are two actin binding domains present in myosin, but not kinesin. These are shown with dashed lines between β_5 and β_6, and α_4 and α_5 and include 180 and 150 residues, respectively. For simplicity, secondary structure elements on these insertions are not shown.

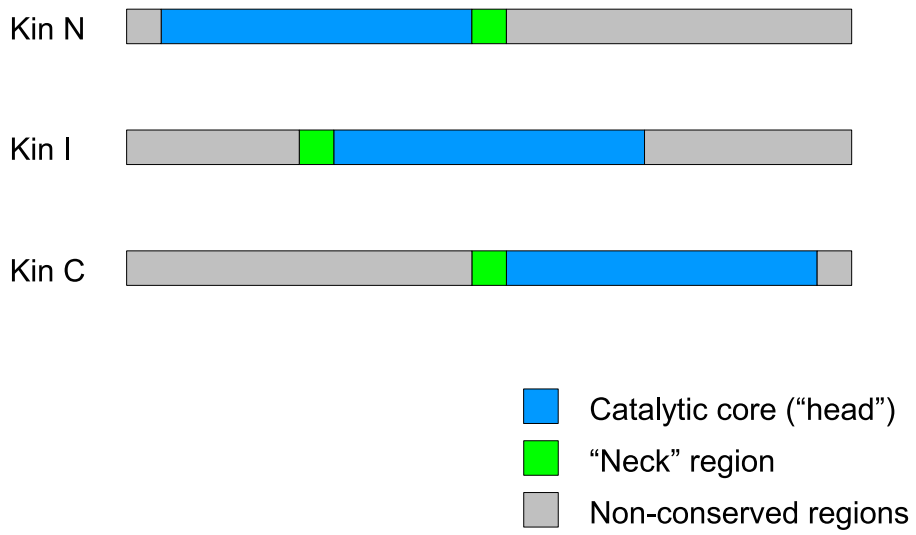

FIGURE 1.3 THE THREE KINESIN CATEGORIES

The schematic shows the classification of kinesin in three different groups, based on the location of the motor core (blue) and neck region (green) within the sequence. The non-conserved regions (grey) often form extended domains that link the motor to the cargo through interactions with adapter molecules. Kinesins that do not fall into any of the three categories due to low sequence homology are termed orphan kinesins. For an example of the functional organization of these domains, see Figure 1.4 on page 50, and for a structural comparison between the *KIN N* kinesin-1 and the *KIN C* kinesin-14 heads see Figure 1.5 on page 51.

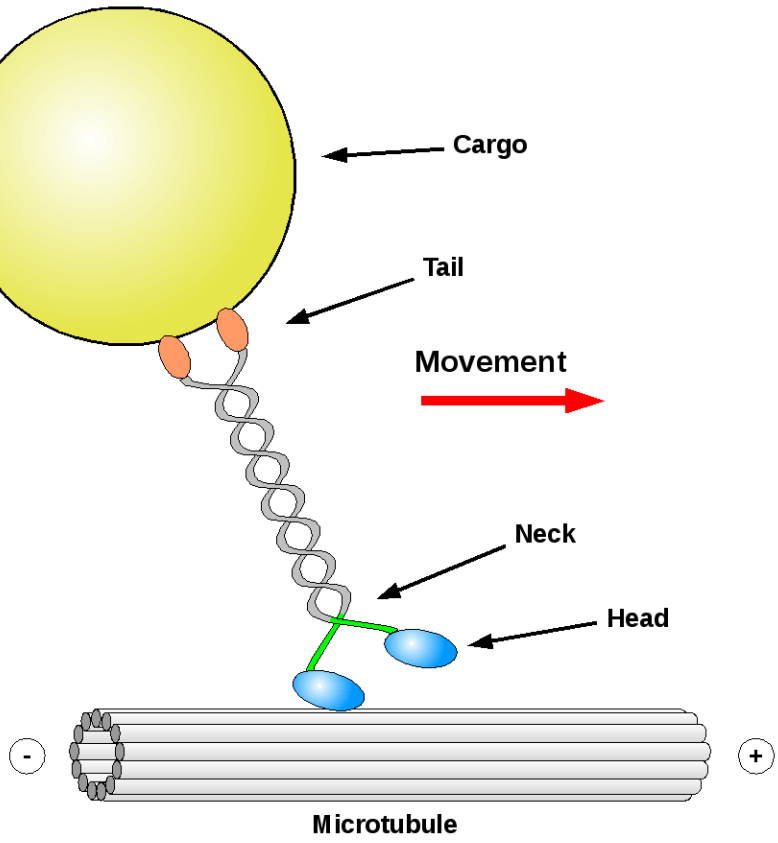

FIGURE 1.4 ORGANIZATION OF KINESIN-1

Kinesin-1 is organized as a heterotetramer of two heavy chains and two light chains. The heavy chains contain the catalytic heads (blue), the coiled-coil dimerization domain (grey), and the neck domain with neck linkers (green) linking the heads to the dimerization domain. The light chains (orange) link the heavy chains to the cargo through a variety of adapter molecules for specific cargoes. The microtubule is shown for reference. The heavy chains of several kinesins are organized in similar fashion, with catalytic heads connected to the cargo by extended dimerization domains, but the relative position of the head within the amino acid sequence differs, as shown in Figure 1.3 on page 49.

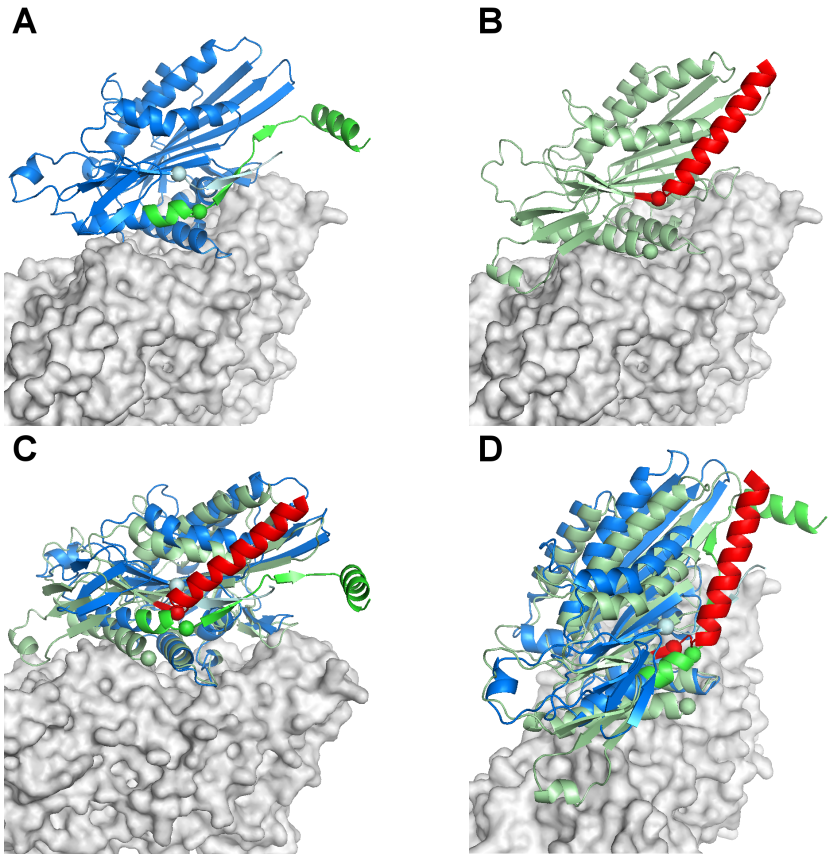

FIGURE 1.5 COMPARISON OF KINESIN-1 AND KINESIN-14

The domain organizations of kinesin-1 (blue) [270] and kinesin-14 (*ncd*) [255] (light green) are compared with respect to the force-transducing elements. Equivalent C_α positions within the sequence are shown as spheres. Tubulin (grey surface) is modeled in approximate location as a reference, with plus-end facing towards the upper right.
(A) Kinesin-1 with the N-terminal region shown in lighter color and the C-terminal force-transducing element in bright green.
(B) Kinesin-14 with the N-terminal force-transducing α-helix colored red and the C-terminal C_α) shown in spacefill.
(C,D) Two different views of the superimposed two structures. For reference, the red and light blue spheres are equivalent residues, as well as the bright green and light green spheres. Atomic coordinates were superimposed by alignment of switch II microtubule binding region residues 601-634 (2NCD) and 256-290 (1MKJ). Tubulin coordinates were modeled based on alignment of residues 256-290 of human kinesin in ATP-like state (1MKJ) and in apo state in complex with microtubule (2P4N).

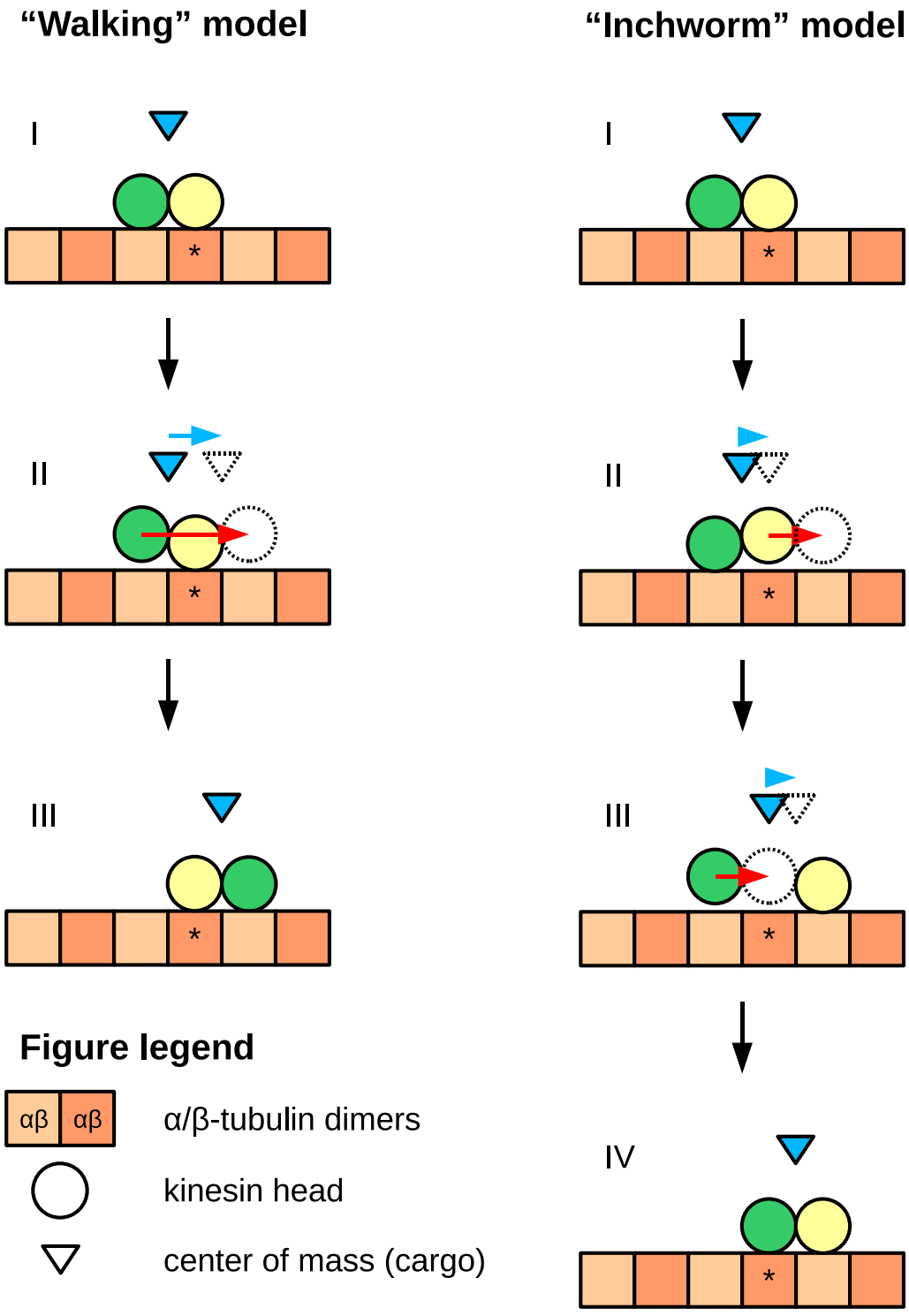
“Walking” model
“Inchworm” model
I
II
III
IV
*
Figure legend
αβ
αβ
α/β-tubulin dimers
kinesin head
center of mass (cargo)

Figure 1.6 Models for processive kinesin motility

Comparison of models for processive stepping of kinesin. The identical kinesin heads are shown as *yellow and green circles* to distinguish them in the drawing. The *blue triangle* denotes the center of mass of the dimer. The *red arrow* and *blue arrow* denote the movement of a head and the center of mass, respectively, and their lengths are proportional to the displacement. The *asterisk* marks a fixed spot on the microtubule. The states are as follows for the hand-over-hand model:

I In the pre-step state, the heads are bound, one behind the other, to the microtubule track.

II Stepping detaches the trailing head (*green*) and moves it forward past the leading head (*yellow*), where it attaches to the next available binding site.

III The post-step state is **mirror-symmetric** to the pre-step state with respect to the *yellow* head. The heads have reversed their relative positions, and the center of mass has moved by **half** of the displacement of the *green* head.

The states for the inchworm model are as follows:

I In the pre-step state, the heads are bound, one behind the other, to the microtubule track.

II The first substep detaches the leading head (*yellow*) and moves it forward to the next available binding site. The separation between the heads increases, and the center of mass moves by $\frac{1}{2}$ of the displacement of the *yellow* head.

III The second substep detaches the trailing head (*green*) and moves it forward to the binding site vacated by the *yellow* head. The separation between the heads decreases, and the center of mass moves again by $\frac{1}{2}$ of the displacement of the *green* head.

IV The post-step state is **equal** to the pre-step state and the center of mass has moved by the **same distance** as each of the heads.

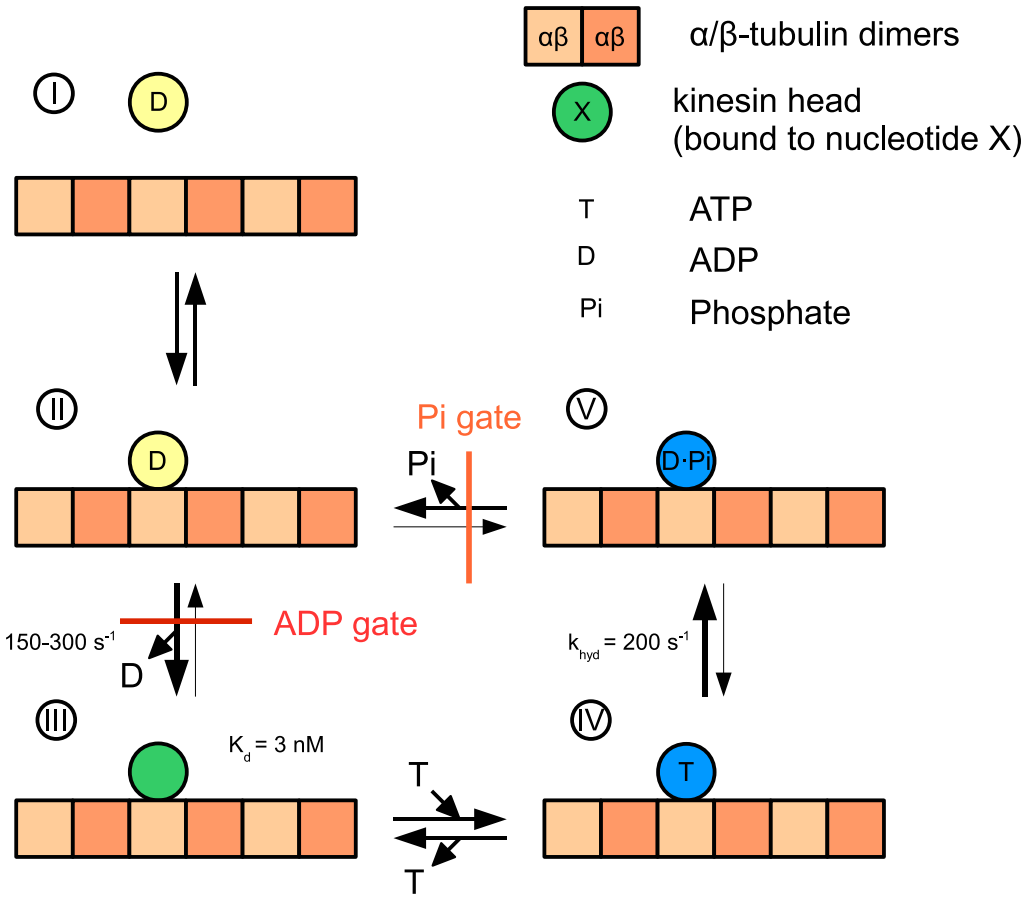

FIGURE 1.7 ATPASE CYCLE OF THE KINESIN HEAD

This sequence illustrates the nucleotide cycle of monomer head.

I Free in solution, each kinesin heads has one tightly bound ADP. Release of this nucleotide is very slow ($0.026\ s^{-1}$) [94, 104], destabilizes kinesin [135, 260] and is therefore not likely to be encountered physiologically [106, 135].

II Diffusional encounter with microtubule leads to weak interaction and starts the kinetic cycle. Subsequent strong attachment of kinesin to the microtubule antagonizes ADP binding and leads to the release of ADP ($150 - 300\ s^{-1}$ for the two-step process [198, 217]). Under physiological conditions this represents an essentially irrevesible gating step, although ADP can rebind if present in sufficiently high concentrations.

III Nucleotide-free kinesin is tighly attached to the microtubule ($K_d = 3\ nM$ [48]) and able to bind ATP.

IV ATP binding to the kinesin head leads to rapid ATP hydrolysis and progression along the pathway ($k_{cat}^{MT} = 60 - 80\ s^{-1}$ [135, 198]).

V Release of P_i is as fast as hydrolysis ($k_{hyd} = 200\ s^{-1}$ [135, 198]) and essentially irreversible [94]. The head is released and can revert to state II. Reattachment is slightly favored over detachment, so that even individual kinesin head possess limited *kinetic processivity* and hydrolyze multiple (approximately 4) ATP molecules before dissociation from the microtubule [148].

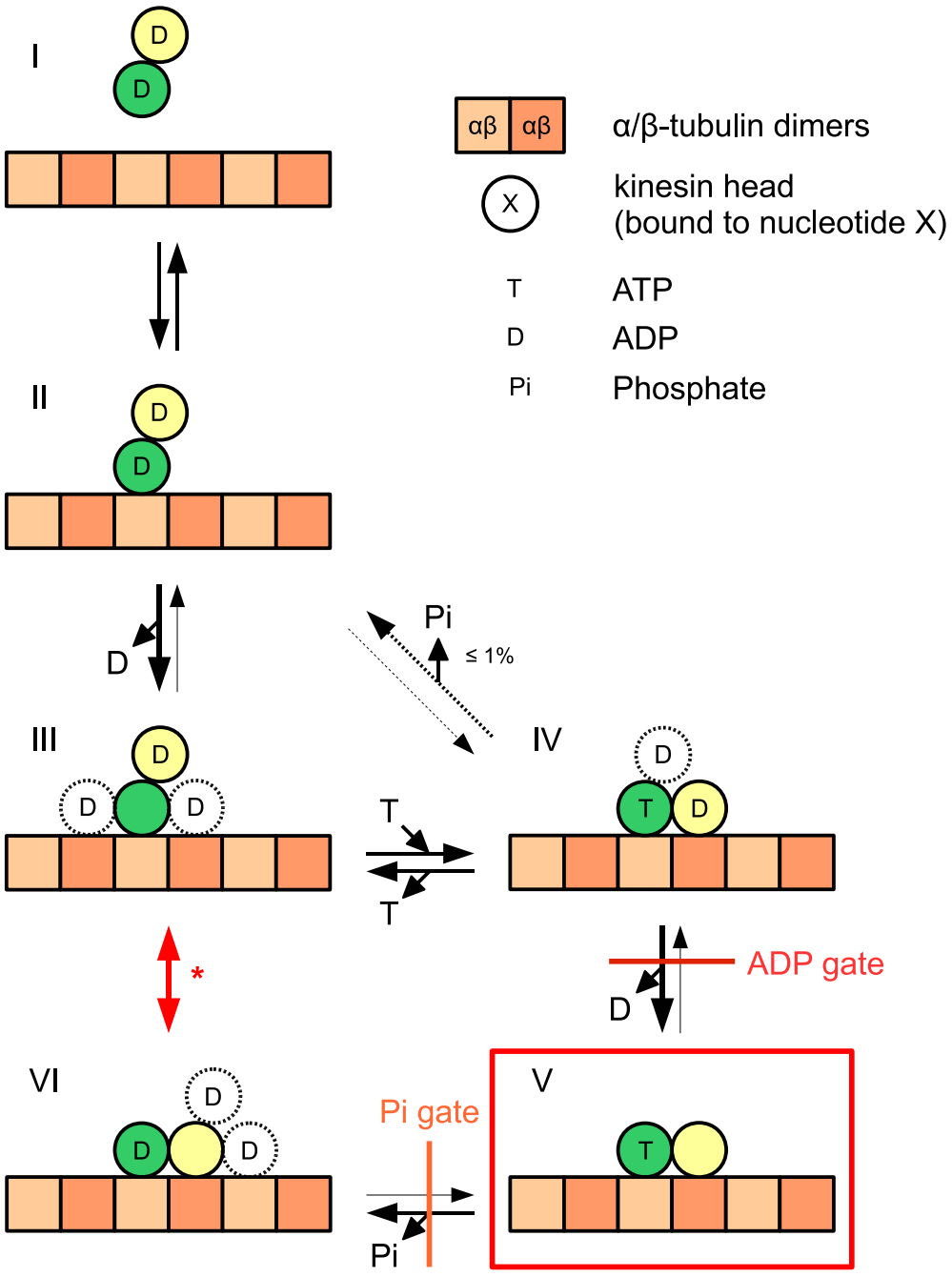

Figure 1.8 Model of processive motility for kinesin-1

This diagram illustrates a model for processive stepping of kinesin. The major pathway follows the states by increasing numerals, except where noted. The red double-headed arrow with asterisk denotes the equivalence of states *III* and *VI*, with the heads having switched roles. Rates for the processes related to individual heads are given on page 1 on page 30 and in Figure 1.7 on page 54.

I In solution, kinesin heads are tightly bound to one ADP molecule per head.

II Diffusional encounter with a microtubule leads to weak attachment and starts the kinetic cycle.

III Attachment of kinesin to the microtubule leads to the fast release of ADP from only the interacting head (at $\approx 50\ s^{-1}$) and (due to the high affinity of the apo state for microtubule) strongly attaches that head in an essentially irreversible gating step to the microtubule [95, 100, 197]. In this "waiting state", the position of the tethered head is unclear [34] (several possibilities are shown in dashed lines), but it releases ADP very slowly ($< 1\ s^{-1}$ [197]) does not strongly interact with the microtubule.

IV Binding of ATP to the attached head induces isomerization of the attached head and rapid attachment of the tethered head from the previous waiting position (shown in dashed lines) ($> 2000\ s^{-1}$ [49]) [260]. Note that ATP hydrolysis at the attached head (and therefore reversion to state II with potential release from the microtubule or futile hydrolysis cycles) competes with ADP release at the tethered head (stepping). Because the rates for these processes are similar (less than 10-fold difference, as mentioned in Figure 1.7 on page 54), both the expected rate of release from the microtubule, as well as the number of futile hydrolysis cycles would be significantly higher than experimentally observed. The observed release probability of $\leq 1\%$ [97, 315] and coupling ratio of 1 ATP per step [46, 265, 324] argue for coordination of nucleotide cycles between the heads.

V ATP-induced isomerization is followed quickly by ADP release from the second head (at $\approx 50\ s^{-1}$ [197]) and strongly attaches the second head to the microtubule. This event traps ATP in the trailing head [52, 307] and leads to its rapid hydrolysis.

VI Release of P_i reverts the trailing head to the weakly attached state, which releases the head from the microtubule and reverts the motor to a waiting state equivalent to state III), but with the head in switched roles.

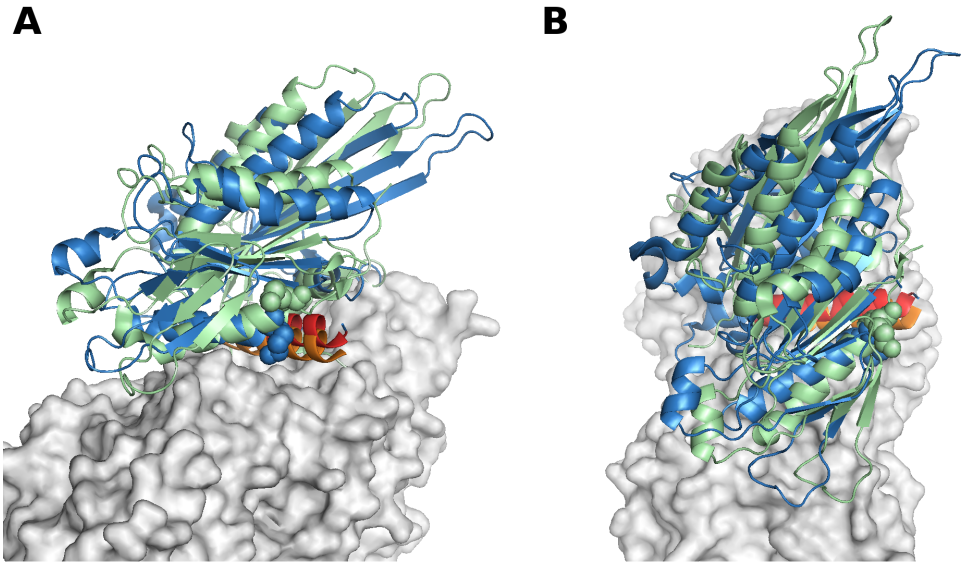

FIGURE 1.9 THE CONFORMATIONAL SWITCH OF KIF1A

This figure compares the microtubule bound structures of KIF1A in the ADP (blue) and ATP-like (green) states [168], (A) looking at the right side of the molecule in the direction of movement and (B) looking approximately perpendiculary at the microtubule interaction surface. The microtubule plus-end is towards the upper right in (A) and up in (B). The switch II helices are colored red and orange for the ADP- and ATP-like states, respectively, and tubulin is shown as a grey surface. For reference, the last resolved residue common to both structures (near the presumed base of the neck linker) is shown in spacefill.

CHAPTER TWO
Methodology

The Electron Microscope

Introduction

The first electron microscope was constructed in 1931 by Ernst Ruska and Max Knoll at the Technische Hochschule in Berlin. Although the resolution of the first prototype was modest at a little over 20 nm, it proved the concept that electron beams could be used to visualize matter [183]. Since then, electron microscope development has been driven by the desire to achieve atomic resolution and beyond. Indeed, resolutions better than 10 Å were achieved after the Second World War, and modern transmission electron microscopes such as the JEOL-2200FS are capable of resolutions below 2 Å [19]. Although a detailed technical description of image formation in the electron microscope can fill books by itself (for excellent references on the subject see [29, 243, 274]) and is well beyond the scope of this document, a brief description of the technical issues directly affecting the collection and interpretation of biological data will be given. It should also be noted that all descriptions here refer to *transmission* electron microscopes, and may not apply to other types of electron imaging equipment, such as *scanning* electron microscopes (SEM).

Electron Microscope Components

As a most simplistic description, an electron microscope should have at least the following components to be useful:

- An electron source (the "gun").
- Lenses to focus the electron beam onto the sample.
- A recording medium to detect interactions between the specimen and the beam.

Of these components, the lenses act on the beam in physically complex ways that cannot be adequately described here. Furthermore, the entirety of lens actions is carefully chosen, such that the interaction of the beam with the sample can be recorded with a minimum of interference of the lenses themselves. The characteristics of the electron gun affect the electron beam, and therefore influence the *interactions of the beam with the sample* directly, while the characteristics of the recording media affect *how we perceive the interaction of the beam with the specimen*. These components will be briefly considered.

Electron Sources

The purpose of the electron gun is to provide an intense, steady stream of electrons with which the sample is illuminated. Electron streams used in conventional electron microscopes typically originate from two physical processes: thermionic emission and field emission. To achieve thermionic emission, a metallic emitter cathode, typically held at a negative potential of 50 - 120 kV, is heated until electrons are extracted and accelerated towards an anode held at ground potential. Two common sources for thermionic emission are tungsten filaments and *lanthanum hexaboride* (LaB_6) crystals. Both types are typically heated to over 2000°C before appreciable emission takes place [243]. LaB_6 crystals are difficult to work with, and are therefore considerably more expensive than Tungsten filaments, but offer 6 - 10X more brightness with similar operating lifetime [274]. Both emitter types have an energy spread in the range of 1.5 - 2.0 eV and opening angles of 0.7 mrad [243]. The energy spread influences the Contrast Transfer Function (CTF), which

is described in detail in section Contrast Formation on page 68.

In contrast to thermionic emission, the field emission effect does not require significant heating of the filament. Instead, a high voltage applied between a tip-shaped cathode and a flat anode produces the necessary electron flux. Although the effect was discovered in 1897 [331], due to technical difficulties the practical application started only in 1966 [50]. Field emission guns (FEGs) require much higher vacuum than thermionic emission (10^{-7} Torr vs. 10^{-5} - 10^{-6} Torr, respectively), but produces a much lower energy spread of 0.1 eV, while the brightness is 10^5 times higher [56]. These advantages, as well as the generally better imaging characteristics of the FEG [348] make FEG-equipped microscopes worth the substantial increase in cost, at least for high-resolution electron microscopy.

Recording Media

Traditionally, images in the transmission electron microscope are recorded on film. Although film is very sensitive, it is generally agreed that sensitivity is not the main issue for choosing the recording medium [56]. Ultimately, information in biological electron microscopy is limited by beam damage, and typically the exposure of the sample to the beam is decreased to limit the damage. Low exposure makes the detection quantum efficiency (DQE) of the recording medium more important than its sensitivity. The DQE is defined as

$$DQE = \frac{SNR_{out}^2}{SNR_{in}^2} \leq 1 \tag{2.1}$$

where SNR_{in} is the signal-to-noise ratio reaching the detector from the sample, while SNR_{out} is the signal-to-noise ratio behind the detector [56, eqn. 1]. The DQE value for commonly used film (such as Kodak SO-163) is 0.85 - 0.9 [56, 274]. Although less important with the advent of higher throughput methods for structure reconstruction, it is also worth pointing out that, in principle, the sampling raster of film is limited by shot-noise, the statistical variation in the number of electrons

that impinge on the recording media. Shot-noise is therefore signal-dependent and follows Poisson statistics [56], but is nonetheless much smaller than what is achieved by current carge-coupled devices (CCDs) operating under the same conditions. This means that, using a high quality scanner, sampling on the order of 1 Å at the specimen is possible [56].

Technical advancements have led to the adoption of CCD cameras suitable for electron microscopy. The recording of images on CCD cameras avoids the long process of developing and scanning film, and the recurring costs of film and chemical use and disposal. In a field where hundreds of films are routinely taken to get enough images of high quality for reconstruction, and where it is not unusual to discard 50% or more of the films, significant increases in overall throughput can be achieved by the use of a CCD camera that requires a minimum of maintenance and manual intervention. Furthermore, CCD cameras can be coupled directly to workstations to produce a pipeline for further image processing and analysis, the results of which can be fed back to the microscope to adjust parameters like defocus, dose, and magnification [31, 286].

Despite the advantages of CCD cameras, the choice of CCD vs. film in ultrastructural electron microscopy has to be carefully considered on a case-by-case basis. The main disadvantages of the CCD camera are its low spatial sampling (currently around 24 μm/pixel) and small image size. Currently common 2048x2048 pixel cameras record only about 1/4 of the area that is captured on film. For this reason, in applications that require large areas to be analyzed together, such as structure reconstruction of filaments, photographic film is the still the preferred method. Nonetheless, development of larger (e.g. 8192x8192 pixels) is currently underway (Hans Tietz, personal communication), and holds the promise to eventually building a pipeline, where the acquisition and interpretation of electron microscopic images is mediated exclusively by electrons.

Image Formation

In the transmission electron microscope, different modes of imaging are possible. These range from *brightfield* and *darkfield* imaging to specialized techniques such as *Scanning Transmission Electron Microscopy* (STEM) and *Electron Energy-Loss Spectroscopy* (EELS). Of these, *brightfield* imaging is by far the most commonly used in biological electron microscopy, including high-resolution electron microscopy, and the following discussion will therefore be limited to this particular imaging mode. While the general treatment of image formation, as described here, is similar to descriptions of image formation for light microscopes, it should be noted that additional complications are present in electron microscope image formation that do not exist in light microscopy.

It is common to describe photons and electrons in terms of both their particle character as well as wave character, whichever is more convenient to explain the phenomenon at hand [29]. One of the more prominent complications when describing electrons as particles is that they, unlike photons, do not travel in straight lines down the microscope axis. Rather, they follow complicated spiraling trajectories that vary with distance from the optical axis [274]. Despite this, however, it is possible to present to the non-expert a useful description by considering only electron paths very close to and nearly parallel with the optical axis ("paraxial rays"), thereby ignoring off-axis effects [274]. This treatment is generally sufficient for the needs in ultrastructural biological electron microscopy, and the procedures generally used, such as microscope alignment, ensure to a large degree that regions of interest in a micrograph are unaffected by deviations from the presented theoretical basis. Indeed the most obvious artifact arising from the non-linear trajectory of electrons is a uniform image rotation. Although this rotation is occasionally confusing to the microscope user (because "up" is not up anymore), it is generally irrelevant to any other aspect of electron microscopy [274]. Due to the more intuitive description of electrons as particles, the basis outlined here will make use of the particle theory as

much as reasonably possible. Nonetheless, due to the dominance of phase contrast with unstained biological specimens (see section Contrast Formation) requires an introduction to the wave theory of electrons, which will be given in that section.

Scattering

Electrons interact with matter more strongly than radiation with similar energy (e.g. X-rays), and such interactions, or scattering events can be exploited to obtain information about the scatterer. The electron wavelength is given by:

$$\lambda = \frac{h}{p} = \frac{h}{\sqrt{2meE}} \tag{2.2}$$

where p is the momentum, E is the accelerating voltage, m and e are the mass and charge of the electron, respectively, and h is Planck's constant [29, eqn. 1.2]. Note that for 200 keV electrons, the wavelength comes out to 2.7 pm or 0.027 Å, suggesting a theorical resolution limit on the order of 5 pm, far better than the practically realized resolution of about 1 Å. The discrepancy arises because electron lenses are inherently poor, and lens aberrations that cannot be corrected in ways analogous to light microscopy dominate image formation.

Interactions between the electron beam and matter lead to scattering events, typically described as "collisions" between beam electrons and atoms. These collisions can be further separated into elastic and inelastic categories, depending on whether energy is transferred during the event. The mean free path of electrons in *vitreous* ice (see section Vitrification/freeze-hydration (a.k.a. cryo-EM)) is approximately 280nm for elastically scattered electrons, compared to approximately 85nm for inelastically scattered electrons [75, p. 16]. The values for scattering from heavy elements are significantly smaller, however, and will be considered separately. In the following discussion, generally only single scattering events are considered, except where noted. Multiple scattering events are difficult to describe, and given

the typical specimen preparation methods, used for biological specimens, that yield sample thickness equal to or smaller than the mean free path of the electrons, it is approriate to ignore multiple scattering phenomena. Generally, elastic and inelastic scattering occurs simultaneously over the area of the specimen, but the discussion will be limited, as much as possible, to what useful information can be extracted from each event [274].

The characteristic of elastic scattering events is that the affected atom or molecule remains in the ground state, and no energy is lost by the impinging electron. This type of scattering occurs predominantly between beam electrons and target nuclei. Based on classical physics (Rutherford scattering model), the nucleus is considered as a rigid, positively charged sphere, and electrons as negative point charges. In this simple model, adapted from the classical Rutherford model for the scattering of α-particles and shown in Figure 2.1A, incident electrons are attracted towards the nucleus by an electronstatic (Coulomb) force related to the distance to the nucleus. They are scattered from their original path by angle θ, related to the radial distance from the nucleus r_n by

$$r_n = \frac{Ze}{V\theta} \tag{2.3}$$

where Z is the atomic number of the target nucleus, and e is the electron charge [274, eqn. 8.6]. It is easy to see that scattering events close to the target are associated with a larger angle θ and are therefore considered as containing high-resolution information. This is particularly important when selecting apertures for imaging, as electrons may be scattered outside the aperture, with a corresponding loss of resolution. The fractional energy loss for a collision between an electron and a target nucleus can be calculated from the following equation:

$$\frac{\Delta V}{V_e} = 2\frac{m_e}{M_n}(1 - \cos\theta) \tag{2.4}$$

where V_e is the accelerating voltage, m_e is the electron mass, M_n is the mass of the target nucleus, and θ is the scattering angle [274, eqn. 8.5]. Note that the mass of nuclei is much larger than that of electrons (approximately $1,845 * atomic\ weight$), and scattering angles for electrons are typically small (on the order of 1°). Therefore, the right side of the equation is very small, and the scattering event is considered elastic.

Inelastic scattering events, in contrast to elastic ones, are associated with the electronic excitation of the affected atom or molecule from the ground state to a higher energy state or even to ionization of the target by completely "knocking off" target electrons. Therefore, inelastic scattering involves the transfer of energy from the impinging electron to the target. Inelastic scattering generally occurs between beam electrons and electrons associated with target nuclei. In analogy to equation 2.3, the scattering angle θ is related to the radial distance between the two electrons r_e by

$$r_e = \frac{e}{V\theta} \tag{2.5}$$

but in this case the beam electron is scattered away from the target electron [274, eqn. 8.6], as shown in Figure 2.1B. Because the factor Z, the atomic number, does not contribute, the angle is smaller than in the case of elastic scattering. The fractional energy loss is then calculated by analogy to equation 2.4. Here, the energy lost due to interaction of two electrons is expressed in analogy to as

$$\frac{\Delta V}{V_e} = 2\frac{m_e}{M_e}(1 - \cos\theta) \tag{2.6}$$

where M_e is the mass of the target electron [274, eqn. 8.5]. Because the fraction of masses on the right side of the equation is close to unity (neglecting any relativistic effects), it is clear that considerable energy loss results from electron-electron scattering. In fact, the amount of energy transferred can be anywhere between zero and the total energy of the impinging electron. This is significant because electron lenses

are not chromatically corrected, and inelastically scattered electrons therefore are not focused correctly to contribute to the image in a meaningful way. Due to the characteristically small scattering angles and the distribtion of energies, though, inelastically scattered electrons tend to pass the objective aperture of the microscope and contribute to the background noise in the image, where they tend to form a "fog". Certain elements exhibit characteristic energy loss spectra, corresponding to energy lost from the excitation of valence electrons. Such spectra and corresponding "elemental" images can be obtained by the use of an energy filter, but this method is not common in biological electron microscopy and will not be considered here.

As mentioned before, both types of scattering occur simultaneously. It is also clear from the above discussion that the total scattering power increases with atomic number. The elastic [274, eqn. 8.7] and inelastic [274, eqn. 8.8] scattering cross sections of an atom can therefore be expressed semi-quantitatively as

$$\sigma_{elastic} = f(Z^{4/3}) \tag{2.7}$$

and

$$\sigma_{inelastic} = f(Z^{2/3}) \tag{2.8}$$

Note that the scattering cross section should be understood not as a measure of the size of the scatterer, but rather as a probablity that a scattering event, elastic or inelastic, will occur. The scattering cross sections for common biological specimens are listed in the following table [274, table 8.2].

Material	$\boldsymbol{\sigma_{elastic}}$	$\boldsymbol{\sigma_{inelastic}}$
Carbon	0.825	1.12
Protein	0.457	0.82
Ice	0.330	0.72
Osmium (stain)	15.840	not avail.

As can be seen, inelastic scattering dominates for unstained proteins, and is al-

together much weaker than scattering obtained from a heavy metal stain such as osmium. The next section will discuss how scattering contributes to image formation.

Contrast Formation

Although brightfield images in the transmission electron microscope may look at first approximation somewhat similar to images obtained from brightfield light microscopy, the underlying mechanisms of contrast generation are very different. The limit at which electron micrographs can be interpreted "by eye" is quickly reached once specimens of subcellular proportions are considered. While the interpretation of organelles in size and shape is generally straightforward, it is not usually possible to make a reasonable interpretation of even large (>400 kDa) molecules or molecular complexes without the help of computational approaches. Contrast generation in the transmission electron microscope is rather complex, and several artifacts greatly influence image formation in non-intuitive ways. Only the most basic considerations for contrast formation, as well as the most commonly encountered artifact limiting resolution, the Contrast Transfer Function (CTF), are discussed here.

Contrast in biological samples can be roughly attributed to two different sources, these being *amplitude contrast* and *phase contrast*. Different methods of sample preparation can produce large differences in the contribution of each source, but it should be understood that to some extent both contribute to the final image. That said, the simplified statement can be made that heavy-atom staining techniques, such as *negative staining* (discussed in section Negative Staining), produce mostly amplitude contrast, while the contrast in unstained specimens, preserved with techniques such as *vitrification*, is mainly from phase contrast.

Amplitude contrast arises because a significant fraction of electrons that impinge on the sample fail to contribute to the subsequent image formation [62]. This

type of contrast can therefore be considered as "deficiency contrast". These electrons can be scattered outside the objective aperture, or be "lost" to inelastic scattering (described in section Scattering). While e.g. heavy metal stains common in biological electron microscopy significantly increase elastic scattering, the likewise increased contribution of multiple scattering events to image formation is difficult to describe. Furthermore, multiple scattering events also increase the probability of electrons to be scattered outside the objective aperture, and thus, again, not contribute to the image. Although electrons that are scattered inelastically do contribute to the image, they do so in a way that is not meaningful for our purposes, and can be considered as "lost" to noise [248]. Other definitions of amplitude contrast are available and more accurate, but the one presented can adequately and intuitively explain contrast generation to the extent needed for a reasonable interpretation of electron micrographs.

From the above definition, as well as the considerations about scattering outlined in section Scattering, it is evident that amplitude contrast in biological specimens is formed largely by stains such as uranyl acetate, and has a minor contribution for images from unstained protein specimens. Given the considerations about scattering outlined above, it would appear that the interest of the biologist is to collect as much of the elastically scattered beam as possible in order to increase the resolution of the image from a stained specimen. This is however incorrect, in that the (amorphous) stain is only useful as far as it faithfully replicates the surface structure of the embedded specimen. Given this limitation, it is in practice more important to the increase the contrast by excluding from the image high scattering angles and inelastically scattered electrons, rather than collecting electrons scattered at high angles. A staining technique that relies largely on amplitude contrast are described in section Negative Staining.

Due to a number of problems associated with staining of specimens (see section Negative Staining), it is desirable to use unstained biological specimens when-

ever possible. As outlined in section Scattering, however, proteins scatter electrons only weakly. Nonetheless, the information contained even in the limited amount of elastic scattering from native proteins can be retrieved and used to reconstruct the underlying density. For this section, it will be more convenient to discuss electron scattering in terms of the wave-optical model.

The wave model describes the electron as a plane wave traveling along the microscope axis (z-direction). The interaction of the wave with the specimen modifies the phase of the wave by an amount in proportion with the thickness of the object. A simple drawing of this model is shown in Figure 2.1. According to this model, the phase shift $\Phi(\mathbf{r})$ of an incident wave due to interaction with the phase object is given by

$$\Phi(\mathbf{r}) = \int C(\mathbf{r}, z)\, \mathrm{d}z \tag{2.9}$$

where $\mathbf{r}$ is a two-dimensional vector, such that $\mathbf{r} = \left[\begin{smallmatrix} x \\ y \end{smallmatrix}\right]$, and $C(\mathbf{r}, z)$ is the Coulomb potential distribution, in three dimensions, within the object [75, eqn. 2.1]. The phase change experienced by the plane wave is thus described by

$$\Psi(\mathbf{r}) = \Psi_0 exp[i\Phi(\mathbf{r})]. \tag{2.10}$$

where Ψ_0 is the incoming wave [75, eqn. 2.2]. Using the weak-phase approximation [125] for $\Phi(\mathbf{r}) \ll 1$, equation can be expanded to

$$\Psi(\mathbf{r}) = \Psi_0 \left[1 + i\Phi(\mathbf{r}) - \frac{1}{2}\Phi(\mathbf{r})^2 + \dots\right] \tag{2.11}$$

where the first term (1) is the unscattered wave, the second term ($i\Phi(\mathbf{r})$) is the first scattering event, and the third term ($\frac{1}{2}\Phi(\mathbf{r})^2$) is the second scattering event [75, eqn. 2.3]. In biological specimens embedded in *vitreous* ice, the mean free path of electrons is close to 300 nm, well over the thickness of the sample, and the equation can thus be truncated after the second term. Assuming that observation of the wave takes place close to the optical axis and far from the specimen with respect to the

wavelength (Fraunhofer approximation) [91], the scattered wave is further modified by the effects of defocusing and lens aberrations, and forms a diffraction pattern in the back focal plane of the objective lens according to

$$\Psi_{bf}(\mathbf{k}) = \mathfrak{F}\left\{\Psi(\mathbf{k})\right\} exp\left[i\gamma(\mathbf{k})\right] \tag{2.12}$$

where $\mathbf{k}$ is the spatial frequency, and $\gamma(\mathbf{k})$ is the summarized effect of the lens action and aberrations [75, eqn. 2.6]. The symbol $\mathfrak{F}$ and later $\mathfrak{F}^{-1}$ denote the Fourier transformation operation, and inverse Fourier transformation, respectively, of the argument. The wave in the image plane is then obtained by multiplication of the diffraction pattern by an aperture function [75, eqn. 2.8]

$$A(\mathbf{k}) = \begin{cases} 1 & \text{for } |k| = \dfrac{\theta}{\lambda} \leq \dfrac{\theta_1}{\lambda} \\ 0 & \text{elsewhere} \end{cases} \tag{2.13}$$

and back-transformation [75, eqn. 2.7]

$$\Psi_{img}(\mathbf{k}) = \mathfrak{F}^{-1}\left\{\mathfrak{F}\left\{\Psi'(\mathbf{k})\right\} A(\mathbf{k}) exp\left[i\gamma(\mathbf{k})\right]\right\} \tag{2.14}$$

Finally, the intensity distribution in the image plane is given by [75, eqn. 2.9]

$$I_{img}(\mathbf{r}) = |\Psi_{img}(\mathbf{r})|^2 \tag{2.15}$$

Given the truncation of 2.11 after the second term, the image is formed by the interference of the unscattered beam with with the single-scattered beam. This imaging mode is referred to as "brightfield imaging", the most common imaging method used in biological electron miroscopy, and is in contrast to "darkfield imaging", where the unscattered wave is blocked in the back focal plane of the objective lens. Also note that, in principle, there is a linear dependence of image contrast to the object potential projected along the optical axis, and thus a straightforward interpretation of the

image is, to some degree at least, possible. However, the biggest hurdle to the easy interpretation of the image is contained in the "lens action" function $\gamma(\mathbf{k})$ in equation 2.12. This effect limits the resolution to which straightforward interpretation is possible, and will be sumarized next.

The effect of the lens on the transmission function is termed the Contrast Transfer Function (CTF). The CTF undulates with respect to spatial frequency, with the outcome that contrast is positive in certain resolution ranges, negative in others, and zero where the CTF intersects the ordinate. Using the weak-phase approximation and assuming that $\Phi(\mathbf{r})$ is real, the relationship between the phase shift $\Phi(\mathbf{r})$ and the image intensity $I(\mathbf{r})$ can be expressed in Fourier space as [75, eqn. 2.10]

$$\mathfrak{F}\{I(\mathbf{r})\} = \mathfrak{F}\{\Phi(\mathbf{r})\} \times \mathfrak{F}\{A(\mathbf{r}) \sin \gamma(\mathbf{r})\} \tag{2.16}$$

The factor $\mathfrak{F}\{A(\mathbf{r}) \sin \gamma(\mathbf{r})\} = h(\mathbf{r})$ where $A(\mathbf{r})$ and $sin\gamma(\mathbf{r})$ are the aperture function and the lens action function, respectively (equations 2.13 and 2.12), and together represent the Fourier transform of the point spread function (PSF). The multiplication of the PSF with the phase shift in Fourier space corresponds in real space to the convolution of the projection of the three-dimensional potential distribution with the PSF, so that [75, eqn. 2.12]

$$I(\mathbf{r}) = \Phi(\mathbf{r}) \circ h(\mathbf{r}) \tag{2.17}$$

In practice, the convolution of the CTF with the image intensity produces effects like fringes and contrast inversions in the image, necessitating CTF correction for the retrieval of information down to the resolving power of the microscope. The technical details of CTF correction are described in section 2.

As mentioned before, the contrast from unstained, native protein specimens is very weak. Specialized techniques had to be developed to visualize biological specimens in the electron microscope. For almost three decades, starting with the

advent of biological electron microscopy in the 1950's, the most common method for increasing contrast was by using stains that replicate the specimen as closely as possible. Only during the 1980's has it become possible to image proteins in their native, aqueous environment. Because the contrast from hydrated proteins is very weak, however, specialized computational methods had to be developed to average large numbers of individual molecules. Today, these methods, often described as "*in silico* crystallization", represent the final push to increase the contrast of proteins to near-atomic resolution [88]. The major techniques for sample preparation for ultrastructural electron microscopy are described in the next section.

Sample Preparation for High-Resolution Studies

For observation of biological samples in the electron microscope, the samples have to be protected from the high vacuum that is necessary for the operation of the microscope. If a hydrated sample were to be inserted in the microscope, the vaccuum would dehydrate the sample as soon as it is inserted into the column, thereby destroying its native structure and rendering it unusable for interpretation of its original state. Furthermore, the dehydration event can release enough water vapor into the column to overwhelm the vacuum system of the microscope, with the prospect of permanent damage to the vacuum system and gun. As such, native biological specimens are inherently poorly suited to electron microscopic observation. Additional problems arise from the poor contrast inherent in most biological assemblies in general, as well as the high sensitivity of chemical bonds found in living organisms to the high-energy electron beam used to image the sample.

One way to protect the sample from electron damage and simultaneously enhance its contrast was developed in the late 1950's with the technique of *negative staining*, where the specimen is embedded in a high-contrast stain highly resistant to electron damage. *Negative staining* technique was the technique of choice for biological electron microscopy until the mid-1980's, when the observation of *frozen-hydrated*, or *vitrified*, samples became practical. *Frozen-hydrated* samples can generally represent molecules and protein complexes in their native, hydrated, state, down to atomic resolution [293, 294] and are today the method of choice for obtaining quantitative structural data for a wide variety of biological samples [75].

More recent developments have led to the combination of classical *negative staining* and *vitrification*, with the goal of merging the advantages of both techniques, while negating their disadvantages. Although these three methods only represent a small fraction of techniques applicable to biological electron microscopy, they were used to gather the vast majority of quantitative, structural data of subcellular macromolecules, and currently represent the backbone of high-resolution

structural electron microscopy. These techniques are outlined below.

Negative Staining

Robert Horne is widely credited with the development and application of *negative staining* to biological electron microscopy. He demonstrated convincingly that biological specimens could be embedded in a thin layer of stain, thereby greatly enhancing their contrast [26]. Stains in common use include heavy metal salts such as uranyl formate, uranyl acetate, ammonium molybdate, and sodium or potassium phosphotungstate. The salt is typically present at low concentrations in the staining buffer, and is applied after partial dehydration of the sample. Uranyl acetate, the stain commonly used for quick assessment of samples in the course of this authors studies, is used at a concentration of 1% to 2%, at the solubility limit of this particular salt.

A general approach to the *negative staining* of purified protein samples is to prepare a buffered solution of the protein/protein complex of interest at a total concentration of 0.1 to 5 mg/ml, depending on the size and nature of the sample. A certain degree of homogeneity is desirable, but it is generally not necessary to purify proteins to the same degree as typically used in X-ray crystallography. Protein samples are often applied to carbon-coated supports on grids of Copper, Rhodium, Nickel, Gold, or Beryllium, to name a few.

In the preparation of the grid, one typically floats a thin support layer of ethyl acetate or atomically flat evaporated mica onto a clean water surface and deposits the grids onto the support surface, such that the support layer adheres to the grid. To increase the resistance of the support surface of the grid to electron damage, as well as to render the support film non-conductive, a thin layer of elemental carbon is evaporated onto the grid [110, 186, 319]. The resulting support surface is hydrophobic, but can be treated in any number of ways to make it suitable to the particular application and electric properties of the specimen. Common treatments

include glow discharge in air (to make the support hydrophilic) and glow discharge in the presence of amyl amine (to render the surface negatively charged).

The buffer containing the protein is typically applied directly as a drop of 2 - 5 μl to the support surface, and excess solution is wicked off using filter paper. Stain is applied to the grid and wicked away as with the protein solution, and the staining may be repeated if necessary to achieve a high degree of embedding of the protein sample. The stained specimen is air-dried to remove excess water, and can then be stored, in many cases for years, without a significant deterioration of the sample itself.

While the contrast enhancement of the specimen afforded by the stain is generally very high, it does come at a price. Artifacts are common with *negative staining* and their implications have to be carefully considered before any interpretation of the underlying specimen structure can take place. The first and foremost artifact is the dehydration of the specimen. During sample preparation, the hydrating water layer around the protein sample is replaced by stain, and the resulting "cast" of stain is imaged. The size of the stain granules generally limits the resolution of the imaged protein surface to around 20 Å [25, 171], although resolutions considerably higher (13 Å [38], 4 Å [202, 203, 268]) have been reported in a few cases. Nonetheless, the stain does not usually penetrate into the interior of a protein or protein complex, which can severely distort or entirely collapse the native structure of the protein or protein complex under investigation [53, 75, 159, 160, 172] and severly limit the obtainable resolution. Furthermore, specimens beyond a certain thickness may not be fully embedded in the stain. The parts of the specimen "sticking out" of the stain are highly sensitive to electron exposure, and therefore do not contribute to the projection image. This leads to a "sided-ness" of the projection images, where projections of the specimen that are expected to be mirror images of each other instead look different.

Another common artifact is the "flattening" of the specimen. Flattening

occurs due to the mechanical forces acting on proteins during *negative staining* and air-drying [159, 160], and can vary widely even within preparations [20]. Boisset and coworkers found that *Androctonus australis* hemocyanin can be reduced to less than 2/3 of the orinal size in the long dimension [21]. In some cases the projection image may only be subtly affected by shrinkage of the specimen in the direction parallel to the beam [20], but in the case of helical specimens such as microtubules and motor-microtubule complexes the flattening effect can severely limit the resolution and interpretability of the reconstruction.

Lastly, a bias toward certain projections within the collection of possible projection views is a commonly encountered with negatively stained specimens. Projection bias arises because the deposition of particles onto the support depends on the interaction between the particle and the support. If a particular surface of the particle interacts better with the support than other parts, the view that brings the interacting surfaces in close contact tends to dominate the projections. Conversely, if a certain view is only possible through unfavorable interactions between specimen and support, this view is likely to be underrepresented or entirely absent from the collection of projections. While the over-/under-representation of certain views does not constitute an artifact in the sense that an artifact can lead to a mis-interpretation of the underlying object, it does affect interpretation insofar as conclusions regarding the structure and/or connectivity of structural elements in the underrepresented view are limited. A case in point would be 2D crystals (stained or unstained), where three dimensional reconstructions require the acquisition of tilted views, and similar considerations can be made for generic objects where only a limited number of projections is available.

Despite these limitations, *negative staining* is commonly employed during the early stages of many projects for rapid assessment of the suitability of a specimen for electron microscopic analysis. In cases where the low inherent contrast of a specimen leads to difficulty in the alignment, and therefore averaging, of the specimen, it can

be helpful to reconstruct the structure from negatively stained samples, and use the resulting model as a reference to assess unstained particles [126].

Vitrification/freeze-hydration (a.k.a. cryo-EM)

It took two decades of work before the limitations of negative staining could be overcome in a practical application, and it is the method of *vitrification*, described here, that is referred to as "cryo-electron microscopy" or short "*cryo-EM*". Several groups succeeded in the late 1970's to embed biological particles in "*vitreous*" ice (from latin: "glass-like"). What makes ice "*vitreous*" is the absence of ice crystals large enough to be detected by X-ray crystallography and other methods. Ice crystals severely damage or distort biological specimens, and absorb more electrons than *vitreous* ice, thereby making observation difficult [2, 62, 63, 75, 89, 189, 293].

Vitrification is achieved by freezing a thin layer of solution so rapidly that water molecules cannot rearrange and form ice crystals. In practice, the *vitrification* procedure is considered an "art", rather than "science". Despite the extensive theoretical work on the subject, the manual steps involved in *vitrification* dominate the procedure, and are therefore highly sensitive to the skill of the experimenter. High variability between samples is common even among experienced electron microscopists, and considering the relatively crude macroscopic tools used to address a microscopic problem, it is quite surprising that the method can work at all. Advantages and problems of imaging freeze-hydrated samples, as well as practical considerations are outlined below.

Imaging samples in vitreous ice affords many advantages beyond the lack of a contrast agent and the problems associated with negative staining. Perhaps the most important advantage is that specimens are imaged in their native, hydrated state. Furthermore, freeze-hydrated specimens are generally not subject to crystal packing forces (except in 2D crystals, of course), and can generally be regarded as true "solution structures", similar to those obtained using techniques such as certain

types of nuclear magnetic resonance spectroscopy. Another advantage offered by cooling samples is a severe drop in radiation induced damage [40, 90, 114, 182].

Despite all the advantages of imaging freeze-hydrated samples, the method is not problem-free. Perhaps the biggest challenge is the low inherent contrast of ice-embedded protein complexes. The obtained contrast is related to the density difference between the sample and the surrounding aqueous medium. The density of protein is approximately 1.3 g/cm^3, very close to the density of pure water of 0.93 g/cm^3 at liquid nitrogen temperature [62]. Contrast can of course be enhanced by increasing the electron dose, but it should be understood that the increased contrast comes at the expense of radiation damage, and therefore high resolution data [262]. Due to the lack of the electron-resistant stain, unstained and *vitrified* samples are much more sensitive to beam exposure than negatively stained samples. Using direct measurements, it was found that beam exposure as low as 6 $e^-/Å^2$ was enough to destroy fine details in ordered arrays of L-valine [87].

To combat this problem, methods have been developed that minimize the exposure of the specimen to the beam. Collectively, these methods are referred to as *minimal dose system* or short *MDS*. They aim to minimize specimen damage from radiation by lowering the electron exposure to the lowest practical levels possible [185]. In practice, exposures of ≤ 10 $e^-/Å^2$ are classified as low dose. As a consequence of *MDS* methods, the contrast in individual images is very low, and can cause problems with the alignment of particles. For this reason, it may be worth to obtain the initial model of a protein of interest from images of negatively stained specimens first, and use them for the initial alignment [75]. Furthermore, larger numbers of particles, often 10^5 to over 10^6 (the exact number generally depends on sample characteristics and the desired resolution) are routinely required to reconstruct structures of ice-embedded specimens, with a general dependence of resolution on the number of high-quality images. Representative examples of proteins and protein complexes that have been solved to successively higher reso-

lution include acetylcholine receptor [211, 309, 311], KIF1A-microtubule complex [164, 166–168, 223], and GroEL [192, 194, 249, 281].

Despite these shortcomings, cryo-electron microscopy of vitrified samples has been used successfully to obtain models of protein complexes, in many cases to near-atomic resolutions [192, 249, 311, 349]. In order to take advantage of the full potential of cryo-electron microscopy, the methods of sample preparation have to be mastered. Although trivial compared to other considerations in the structure reconstruction procedure, the manual steps nonetheless play a critical role in the overall method, and we will briefly consider them here.

The electron absorption of *vitrified* samples necessitates that the thickness of the solution on the EM grid be on the order of less than 100 nm [75]. In practice, it is difficult to control film thickness, but a simple freeze-plunging apparatus to prepare *vitrified* samples has been used to good effect [62]. A schematic of the freeze-plunger with the most important components is shown in Figure 2.2. Several manufacturers are making making manual freeze-plungers, and due to the difficulty to achieve consistent results, automated blotting devices were developed [77], and have been used successfully [24, 143, 275, 326]. Manual and automated freeze-plungers are shown in Figure 2.3. Despite automation, the specimen preparation procudure is the same. Briefly, the sample is applied to the grid support, excess solution is blotted off, and the grid is plunged into liquid ethane or propane.

The choice of the freezing medium is dominated by the need for a high rate of energy transfer from the sample to the cooling medium. Using liquid ethane or propane as the cooling medium, the attainable cooling rate has been estimated to be on the order of 10^6 °C/s for thin (on the order of a few tens of μm) layers of aqueous solution [62, 75]. The time between blotting and plunging is perhaps the most critical, as rapid evaportion of the thin solution layer limits the time the experimenter has to freeze the specimen [55] and necessitates in many cases tight control of the humidity and temperature of the atmosphere. Once frozen, the

grid is transferred to a liquid nitrogen tank and is kept under liquid nitrogen until observation in the electron microscope.

Specially designed cryo sample holders keep the specimen at or the near liquid nitrogen temperature (approximately -180°C) during transfer to and observation in the microscope. At this temperature, water evaporation is negligible, even in the vacuum of the microscope column [62], and observation for extended periods is possible. Aside from keeping temperature, the design of the holder is crucial in isolating the the specimen from vibrations, e.g. from the bubbling of nitrogen in the dewar. Examples of typical cryo sample holders are shown in Figure 2.4.

Lastly, the grids used for vitrified samples can have continuous carbon surfaces, as in the case of *negative staining*, but due to the carbon background it is often desirable to use "holey carbon" grids, where the carbon has holes that can be used to image particles without the carbon background. Such grids can be made by hand [62, 80], but holey films with a defined hole pattern have been developed [39, 239] and are commercially available, e.g. under the name "Quantifoil" (Jena, Germany) [70], and offer advantages, especially for the automated collection of images [31, 238, 253, 281, 286].

Representative results of the freezing procedure is shown in Figure 2.5. It is worth noting that the clear *vitreous* ice desired for high-resolution structural studies can co-exist with small ice crystals on the same specimen. Ice crystals can develop through transient warming of the sample at various stages of the procedure, through continued exposure of the sample to the electron beam, or through deposits originating from small leaks in the microscope vacuum system, and generally limit the duration of observation. More recently, the method of cryo-negative staining was developed to combine the advantages of *negative staining* and *freeze-hydration*. This method is outlined below.

Cryo-Negative Staining

The relatively new method of *cryo-negative staining* was developed to increase the low inherent contrast of protein specimens in ice without significantly distorting the structure of the specimen down to near-atomic resolution [1]. Briefly, in *cryo-negative staining*, the sample is prepared in a way similar to conventional *freeze-hydration*, but with the difference that the grid is incubated with stain prior to freezing. Commonly, a 16% ammonium molybdate solution is used in conjuction with holey films [1, 58, 112], compared to the 2% stain concentration typically used for conventional *negative staining*.

Besides the intended effect of increasing signal-to-noise ratio about 10-fold [58], the stain was also found to significantly decrease the sensitivity of the specimen to beam damage. While unstained particles of GroEL could be seen disintegrating, with an attendant loss of contrast, in unstained *vitreous* ice at a dose of 10 - 30 $e^{-}/Å^{2}$, the same dose had little discernible effect on the same sample stained with ammonium molybdate [58], and the GroEL could subsequently be solved to better than 10 Å resolution [57].

Despite these obvious advantages of *cryo-negative staining*, the method is not entirely free of problems, which includes the deformation of certain tubular structures, presumably due to surface forces during staining [111]. Nonetheless, the method holds much promise, especially for protein that fall below the size limitation typically required for conventional cryo-EM. In practice, it is difficult to align particles in size less than about 300 kDa, and the spliceosomal U1 snRP of about 200 kDa solved by cryo-EM [282] is currently the exception, rather than the rule [75]. Due to the increase in signal-to-noise ratio of particles stained by *cryo-negative staining* technique, it may be possible to push the molecular size limit for cryo-electron microscopy lower by using this technique.

Helical Analysis

Due to the extreme depth of field of the electron microscope, micrographs of objects recorded by transmission electron microscopy represent projections of the electron density distribution along the beam direction. Several methods have been developed to reconstruct the three-dimensional structure of proteins and protein complexes from their projections. A general method to reconstruct the three-dimensional image of a specimen from micrographs has been proposed [59] and successfully implemented [122, 147, 166, 209, 211, 230, 254, 303, 304, 309, 310]. Among the commonly used methods are techniques for the reconstruction of individual, spread-out single particles [193], 2D crystallization methods [8], tomographic reconstruction [232, 321], and helical analysis [60, 162, 230]. Of these, helical analysis was among the first to find practical use [179]. Helical objects lend themselves to structure reconstruction because a single projection image of the object contains information about all the views present in the specimen. A further restriction for protein complexes occurs because only $p1$ and $p211$ spacegroups are allowed for proteins, due to the chirality of the peptide bond [179]. Thus, the only symmetry operations allowed for tubular crystals of biological materials are [179]:

translation parallel to the z-axis.

rotation of $\frac{2\pi}{N}$ radians about the z-axis, where $|N| \geq 1$ and integer.

screw displacement consisting of a translation parallel to the z-axis and a rotation of $\frac{2\pi}{M}$ radians about the z-axis, where $|M| \neq 1$. Furthermore, $M = \frac{u}{t}$, where u is the number of asymmetric units distributed along t turns of the basic helix; both u and t are integers.

twofold rotation about a line perpendicular to and intersecting the z-axis

Among these general symmetry operations, the fixed physical relationship between morphological units and the number of turns of the basic helix leads to a "*selection*

rule" that is the characteristic of the helix. The selection rule is expressed as

$$l = tn + um \tag{2.18}$$

where l is the layer line number, u is the number of morphological units along t turns of the basic helix, n is the start number of the basic helix, and m is an integer. For convenience with calculations involving cylindrical or helical structures, cylindrical polar coordinates are used to express the real space density as $\varrho(r, \phi, z)$, where r is the radius, ϕ the azimuthal angle and z the position along the helix axis. The corresponding Fourier space coordinates are then expressed as $F(R, \Phi, Z)$. Briefly, the reconstruction process consists of the following steps, which are shown schematically in Figure 2.6:

1. the helical object is recorded in the microscope as a 2D projection along the beam axis.

2. the scanned micrograph of the helical object is transformed to Fourier space, yielding a two-dimensional diffraction pattern of the projection of the object.

3. from the diffraction pattern if not otherwise known, the helical symmetry of the object is determined.

4. helical symmetry is imposed to extrapolate the 2D transform (diffraction pattern) of the object to 3D.

5. Fourier-Bessel transformation is used to calculate the real-space 3D density map from the 3D transform.

Step 1 is described in section 2 on page 63. Step 2 is generally done computationally, often using the Cooley-Tukey Fast Fourier Transform (FFT) algorithm [42]. While this step yields a "diffraction pattern" of the image, it is important to keep in mind that, unlike with "real" diffraction patterns, the phases are computed as well,

and there is no phasing step involved. Step 3, indexing of the diffraction pattern, is the most difficult and important, and has been extensively treated by others [169, 170, 180, 302]. While even a simple description of the process is beyond the scope of this document, a few common problems and their implications are mentioned here. First and foremost, determination of the exact symmetry from the micrograph is often very difficult, especially if the diameter of the tube is large [302]. Furthermore, several slightly differing solutions may seem acceptable to explain the diffraction pattern, especially when one has to deal with lattice distortions as small as a a few tens of degrees. Consider the example of actin with a helical repeat of 13 asymmetric units for every 6 turns, so that $\frac{u}{t} = \frac{13}{6}$. The angle between the subunits is then 166.1538° and the helical repeat 355 Å. If the twist decreases slightly, thereby changing the angle between subunits by 0.128° to 166.2818° (very reasonable with large helical polymers), the lattice changes to $\frac{u}{t} = \frac{1299}{600}$, with the repeat increasing approximately 100-fold to 35,463 Å [65]. This change can go undetected, may be difficult to index, and may influence the obtainable resolution. Lastly, if the incorrect symmetry relationship is chosen and imposed during reconstruction, the resulting density map may or may not look "wrong", but in any case there is no way to determine from the result the "correct" selection rule. Together, these problems suggest that special care has to be taken during indexing, particularly in the early stages of structure determination, and that alternate possibilities have to be kept in mind and occasionally re-evaluated.

Once the selection rule has been determined and the diffraction pattern indexed, the reconstruction of the density map is performed. The selection rule links the layer line number l to the order n of a Bessel function given by

$$J_n(x) = \sum_{k=0}^{k=\infty} \frac{(-1)^k \left(\frac{x}{2}\right)^{n+2k}}{k!(n+k)!} \tag{2.19}$$

The contribution of J_n to the scattering amplitude on layer line l is given by $G_{n,l}$ (sometimes referred to as big G):

$$G_{n,l}(R) = \sum_j f_j J_n(2\pi R r_j) \times exp\left[i\left(-n\varphi_j + \frac{2\pi l z_j}{c}\right)\right] \tag{2.20}$$

and the scattered amplitude on layer line l is obtained by summation over the orders n, such that

$$F(R, \psi, l/c) = \sum_n G_{n,l}(R) \times exp\left[in\left(\psi + \frac{\pi}{2}\right)\right] \tag{2.21}$$

Finally the density map is obtained by Fourier-Bessel inversion according to

$$g_{n,l}(r) = \int_0^\infty G_{n,l}(R)\, J_n(2\pi R r)\, 2\pi R \,\mathrm{d}R \tag{2.22}$$

and summation over n and l

$$\varrho(r, \varphi, z) = \frac{1}{c} \sum_{l=-\infty}^{\infty} \sum_{n=-\infty}^{\infty} g_{n,l}(r) \times exp\left[i\left(n\varphi - 2\pi l \frac{z}{c}\right)\right] \tag{2.23}$$

The structure factor per asymmetric unit for layer line l is given by

$$F(R, \psi, l/c) = \sum_j \sum_n f_j J_n(2\pi R r_j) \times exp\left[i\left\{n\left(\psi + \frac{\pi}{2}\right) - n\varphi_j + \frac{2\pi l z_j}{c}\right\}\right] \tag{2.24}$$

Note that in addition to the theory outlined above, it is often necessary to correct distortions in order to reach higher resolution. One of these distortions is the tilt of the helix with respect to the beam, referred to as out-of-plane or ω-tilt. Several methods to estimate and correct lattice distortions are listed in section 2, which also includes information about Ruby-Helix, a semi-automated software package for helical and asymmetric helical analysis.

Asymmetric Helical Analysis

Introduction to Ruby-Helix

Several software packages have been developed for the analysis of helical structures [15, 32, 230, 302, 328, 339], based on helical diffraction theory [60, 179], as described in section 2. These packages typically use shell or Perl scripts to combine a number of programs that are written in C or Fortran to carry out the analysis. As the application of more techniques is needed to obtain increasingly higher resolution from complex and heterogeneous biological structures, this approach becomes more complicated, because the shell or Perl script needs to provide each C or Fortran program with all the parameters required for processing the data.

One approach to this problem is to make a scriptable environment specific to the analysis, as has been done with the Crystallography & NMR System (CNS) [28] and DENZO software packages [228] for X-ray crystallography, and the SPIDER [76] and Situs [333] packages for electron microscopy. Recently, the Python programming language has been used to integrate existing software packages, rather than making specialized scriptable environments. Integration of EMAN [193] and SPIDER into Python is underway, and collection of cryo-EM data is being automated using Python as well [286]. One advantage of the integrated scriptable environment is that necessary parameters (e.g. magnification, defocus, helical lattice parameters), once defined in the script, are "remembered" by the scriptable environment or its objects. Users, therefore, do not need to provide all the information to apply an image analysis method. This advantage makes scripting languages suitable for rapid program development for scientific data processing.

Another problem with the existing helical analysis software packages arose when the new method of asymmetric helical reconstruction [162] was applied in order to analyze motor-microtubule complexes. Even though the theory of asymmetric

helical reconstruction is an extension of conventional helical reconstruction, existing software packages could not be used without extensive modifications. This is because the Bessel orders are hard-coded to be integers in the C or Fortran programs, while the Bessel orders can be non-integers in asymmetric helical reconstruction.

Therefore, Ruby-Helix was developed to solve the problems of software integration and to implement asymmetric helical reconstruction. Ruby-Helix was written using the object-oriented language Ruby [295], a programming language in many respects similar to Python. Furthermore, several new tools to facilitate helical image analysis, as well as to automate many of the repetitive steps involved in helical analysis were incorporated in Ruby-Helix.

Many essential parameters for helical and asymmetric helical analysis are grouped conveniently in two control files, significantly decreasing the workload on the user, and allowing users to take full advantage of the automation offered. Overall, use of Ruby-Helix can considerably decrease the time required for the development of software and to analyze a large number of cryo-EM images to determine high-resolution structures. In the following sections, a kinesin-microtubule complex is used as an example to demonstrate how image processing is performed using Ruby-Helix.

Ruby-Helix Architecture

Ruby-Helix is built on the object-oriented language Ruby [205, 295]. Although Ruby uses interpreted scripting language, the actual calculations are carried out by the underlying compiled libraries (Fig. 2.7), yielding speeds of calculation similar to those of programs written in C or Fortran. The main libraries used for computation are NArray (http://narray.rubyforge.org/), GSL (GNU scientific library, www.gnu.org/software/gsl/), Ruby/GSL (http://rb-gsl.rubyforge.org/), and FFTW3 [79].

In designing Ruby-Helix, three principles were followed. First, the file for-

mats used for the analysis are compatible with the existing MRC package [15, 54]. As a result, Ruby-Helix can read and write image files, big G files, and other control files in MRC format. Second, since computers equipped with gigabytes of memory are commonly used for image analysis, the comparatively slow file input/output to hard disks is minimize by processing data in random access memory (RAM). This does not only improve the speed of calculation, but also reduces the conflicts of names of intermediate files. Third, most of the code is written in Ruby. The algorithms used in the analysis are thus easily traceable, and expansion of the package is straightforward. In addition, the two master parameter files are also read as Ruby scripts. Therefore, parameters can also be given as equations, which is necessary to automate image analysis. Finally, use of the Ruby environment makes debugging easy, because one can easily modify the programs without compiling them.

Overview of helical image analysis using Ruby-Helix

Fig. 2.8 shows the outline of the overall helical image analysis procedure using Ruby-Helix. Except for the selection of seam-free sides, which is unique to asymmetric helical reconstruction, both conventional and asymmetric helical reconstruction use the same programs for the analysis. For correcting the distortions of the helical object, many existing techniques, such as dividing helical objects into short segments and correcting tilt and shift [15, 168, 302], were incorporated in Ruby-Helix. The following sections describe the new implementations and techniques introduced to Ruby-Helix: iterative unbending, defining the repeat length, and selection of the seam-free side in asymmetric helical reconstruction.

Straightening of the helical object

To restore strict helical symmetry from curved helical objects, a new graphical interface program and a script for rapid image straightening were developed. Typically, long helical objects are curved, disturbing the crystalline nature of the

helix and spreading out layer lines in the Fourier transform of the image. Two programs in Ruby-Helix correct distortions automatically.

First, a graphical interface called `Unbend` is used to manually trace the axis of the helical polymer (Fig. 2.9A), and to generate a spline curve along the image to be unbent [64]. This graphical interface program superimposes the spline curve onto the image, so that the user can put enough control points to trace the curved helical polymer. Usually, the distances between the control points are determined empirically depending on the curvature of the helical object: the more flexible the object, the more control points are required, although it is advisable to avoid highly curved tubes/filaments for higher resolution analysis.

The positions of control points are then refined by a program, `auto_unbent`. For a segment of length l, usually on the order of the repeat length, and centered around each control point, `auto_unbent` calculates the 1D projection along the spline curve [344]. The program then performs a cross-correlation $CC_n(\delta x)$ of this 1D projection with its mirror image, and adjusts the spline curve towards the cross-correlation peak defined by:

$$CC_n(\delta x) = \int \left(\int_{y_n - l/2}^{y_n + l/2} \rho(x + \delta x, y) dy \right) \left(\int_{y_n - l/2}^{y_n + l/2} \rho(-x - \delta x, y) dy \right) dx, \quad (2.25)$$

where ρ is the image of the helical polymer, whose axis is parallel to the y-axis and (x_n, y_n) is the coordinate of the n-th control point.

The 1D projection along the filament axis of any helical object should be mirror symmetric, provided that the segment contains approximately one repeat. By taking advantage of this symmetry, the shift of the helix axis from the image center $x = 0$ from δx that gives maximum cross-correlation $CC_n(\delta x)$ can be reproducibly and robustly determined. The coordinates of each control point are automatically adjusted by this value, and written to a new file. As the shift also depends on the neighboring control points, normally several rounds of correction are performed.

A result of this procedure applied to a kinesin-microtubule complex is shown in Fig. 2.9. Even though some of the initial control points were more than 10 Å away from the center of the microtubule, the program quickly corrected the distortion after three iterations to less than 2.5 Å (Fig. 2.9B). As shown in Fig. 2.9C, both the amount of shift and the shortened filament image can be inspected to ensure convergence of the fit towards the center of the helical polymer.

In a later step, further distortion correction is performed using the indexed layer line data, because the helical object can be tilted not only in the plane of ice, but out of the plane as well. These deviations are commonly termed x-shift (in-plane shift), and ω-tilt (out-of-plane tilt), respectively [60].

To correct these distortions, a semi-automated routine for rapid correction and refinement of ω-tilt and x-shift was incorporated in Ruby-Helix. If the image data shows clear layer lines, user input may be limited to three steps of intervention:

1. identification of the axial height of a particular layer line
2. determination of layer line peak positions across the meridian in the transform
3. generation of a parameter file specifying the indices of layer lines to be used for refinement along with the peak positions determined in the previous step.

`Refine_omega_xshift` will compare the near and far side layer lines at a given x-shift and ω-tilt to minimize the phase residuals. If the refinement process does not converge, the user can intervene by modifying the search range of (x, ω) and try the refinement again.

Defining the repeat length

The first step in helical image analysis is to identify the repeat length. In a later step, it is important to precisely determine the start and end position of the boxed area to include an exact multiple number of repeats to avoid layer line spreading over multiple pixels in the Fourier transform. Two programs to facilitate this

process were developed and incorporated into Ruby-Helix, `correlation_matrix`, and `find_truepitch`.

`correlation_matrix` was developed to initially determine the repeat length, and is suitable when the repeat length is not known. `correlation_matrix` calculates the correlation between two segments of equal length (Δy) according to the following equation:

$$CM(y_1, y_2) = \int \left(\int_{y_1 - \Delta y/2}^{y_1 + \Delta y/2} \rho(x, y) dy \right) \left(\int_{y_2 - \Delta y/2}^{y_2 + \Delta y/2} \rho(x, y) dy \right) dx, \qquad (2.26)$$

where ρ is the image of the helical polymer, whose axis is parallel to the y-axis. The length of segment (Δy) is typically chosen to include more than one protein subunit along the helix axis. This "correlation matrix" is written out as a MRC image (Fig. 2.11D). By inspecting the matrix image, the start and end positions of the repeat(s) can be obtained.

This correlation matrix method has advantages over the standard cross correlation method [345], especially when there is heterogeneity within a helical polymer. With the standard cross-correlation method, a smaller region is selected as a reference and a larger region is used as a test image to search for repeats. Therefore, the search depends on the choice of reference image. On the other hand, our method systematically seeks out similar pairs of segments along the entire length of the helical polymer. As a result, a better reference image that gives higher correlation values can be chosen. For example, in the microtubule image shown in Fig. 2.11A, segments with three internal striations give higher correlation values (Fig. 2.11D, red asterisks). When selecting repeats, these higher peaks are more reliable than others. Second, heterogeneity of the helical lattice can be easily detected in the correlation matrix. For example, the microtubule shown in Fig. 2.11 contains a microtubule with both 14 and 15 protofilaments. A transition from the 15 to 14 protofilament lattice obvious in the correlation matrix as a change of striation

pattern (Fig. 2.11D, filled arrowhead.)

Although the above method is useful to roughly determine the repeat length, more precise refinement of the repeat boundaries is required, as it is essential for bringing higher order layer lines to an integer height. `Find_truepitch`, an algorithm developed for this purpose, can determine the repeat length using reference layer line data by performing a cross-correlation search within an image to find similar "patterns" common to both reference image and test image. Using repeat parameters defined in the master parameter file, `find_truepitch` generates a real space 2D projection image from a big G file. This reference image is moved along the length of the filament image, and the cross-correlation plotted as a function of position. A typical plot is shown (Fig. 2.12, solid lines). Beginning and end of each repeat can be determined by noting the cross-correlation peak positions (Fig. 2.12, arrowheads) and entering them for further analysis into the master control file. Furthermore, lateral deviation from the spline curve is plotted on the same graph (Fig. 2.12, green dots), giving a way to exclude pseudo-peaks.

Automated refinement using auto_refine

Polymerized fibrous proteins such as actin and microtubules generally contain more than one repeat per filament. In such a case, each repeat has to be analyzed, refined and extracted individually to obtain high signal-to-noise ratio. `Auto_refine` was developed to automate several of the steps required for refinement, some of which are described above. Based on switches within the master control file (Fig. 2.10), the following subroutines can be executed automatically: boxing out of segments based on information from `correlation_matrix` or `find_truepitch`, refinement of the repeat boundaries, refinement of out-of-plane tilt and in-plane shift, extraction of layer line data, and spline curve refinement.

To help achieve convergence of the automated refinement process, it is generally helpful to check that the following conditions are met:

1. The boxed out filament should appear reasonably straight and centered within the box.

2. The Fourier Transform of the boxed image should display layer lines clearly distinguishable from background intensity, and at integer height.

3. Layer lines selected for tilt and shift correction should show sharp peaks, whose positions are in agreement between near and far side. Note, that layer lines with non-integer Bessel order do not have peaks at the same positions.

4. ω-tilt values should be within reason given constraints on the sample, e.g. under ice thickness conditions typical of cryo-EM. ω-tilt values for filaments such as actin or microtubules should rarely exceed about 20 degrees.

Analysis of helical objects with a seam

To select seam-free side layer line data, asymmetric helical reconstruction takes advantage of two characteristics of layer lines with half-integer Bessel orders. First, when layer line data is averaged, the seam side data cancel each other, while the data from the seam-free side should be enhanced. This is because a M-function $M_{1.5}(x, \Phi)$, at the first amplitude maximum, shows varying phase in $\pi < \Phi < 2\pi$ (seam side), while the function in $0 < \Phi < \pi$ (seam-free side) has constant phase (see Fig. 4A in [162]). As a result, averaged big G data from the mixture of seam side and seam-free side layer line data can be used as a reference for seam-free data. When data from seam-free and seam sides are aligned to this reference, phase residuals of non-integer layer lines will generally show higher phase residuals for seam sides than for seam-free sides (Fig. 3.12C). Second, it is a binary choice to select seam-free side from the near and far sides extracted from one repeat of helical object. This characteristic can be used as an independent criteria for seam-free side selection. This method ultimately depends on the quality of the reference used for averaging, but it is entirely possible to find the seam side without prior knowledge

of its location, even for small sets of data.

Experimental Methods

Sample Preparation

Dimeric Drosophila kinesin constructs were expressed in E.coli using a pET-21 expression vector (Pharmacia LKB Biotechnologies, Inc.) and purified using standard protocol [135]. Protein was stored at -80°C until used. Tubulin was purified from bovine brain using three cycles of polymerization/depolymerization and frozen at -80°C until used. 3 mg/ml tubulin was polymerized in PEM30 buffer (30 mM PIPES-Na, 1 mM EGTA, 1 mM MgCl2, pH 6.8) in the presence of 8% DMSO and 1 mM GTP for 1 h at 37°C. Microtubules were diluted to 0.3 mg/ml in PEM30 buffer containing 40 nM Taxol to stabilize microtubules. 4 μl microtubule solution was applied to a glow-discharged holey-carbon grid and incubated for 1-2 min in the humidity-controlled athmosphere inside the Vitrobot blotting machine (FEI Co.). For all experiments, 100% air humidity was maintained during incubation. After incubation, the grids were briefly blotted from the side with filter paper, and 4 μl of kinesin solution (0.15 mg/ml, in PEM30, 2mM AMPPNP or 2 U apyrase [123, 124, 129] was applied. The grid was incubated for an additional 2-3 min, as before. Without blotting, the grid was then mounted on the guillotine-device of the Vitrobot, excess solution was blotted off (typically 1-4 s), and the grid was flash-frozen in liquid ethane at -180°C [4]. Grids were kept in liquid nitrogen until imaging in the electron microscope.

Imaging and Data Analysis

Grids were imaged under minimal dose conditions on a JEOL-2200FS electron microscope equipped with a field emission gun at an operating voltage of 200 kV and cryo stage kept at -180°C (94K) (dimeric constructs) or JEOL-3000SFF with a field emission gun at 300 kV operating voltage and cryo stage kept at -268°C

(5K) (monomeric constructs) at a nominal magnification of 40,000X (JEOL Ltd., Tokyo, Japan). Images were recorded on film (Kodak SO-163, Eastman Kodak Co., Rochester, NY, U.S.A.) and selected micrographs were digitized on a LeafScan45 (Leaf Systems, Inc.) to a final resolution of 2.5 Å/pixel. Scanned images of 16-protofilament, 4-start microtubule were computationally unbent [64], and reconstructed by conventional helical analysis [59, 60] using the Ruby-Helix software package [207]. Reconstructions from individual helical microtubule repeats were averaged in Fourier space to obtain the final reconstructions. Data was visualized using the AVS software package (Advanced Visual Systems, Inc.), PyMol (DeLano, Warren L. "The PyMOL Molecular Graphics System (2008)", DeLano Scientific, Palo Alto, California, USA, http://www.pymol.org), or UCSF Chimera [236].

Docking and Comparisons

For direct comparison of EM density distributions, the corresponding EM maps were aligned to the same origin using hlxfit4.com [207]. Docking of PDB crystal structures into EM maps was done using the Situs software package [332, 333]. Briefly, a single kinesin-microtubule unit was cut out from the reconstruction and converted to MRC format. The MRC density map was converted to the Situs format using the `conformat` file format converter from the Situs package. The crystal structures of tubulin (PDB ID:1JFF [191]) and kinesin (PDB IDs: 1BG2 [184] for human and 2KIN [258] for rat kinesin) were independently docked to the map using the `colores` program run with default parameters except for the resolution cutoff of 18 Å and Euler angle search increments of 2.0°. Where deemed necessary, the atomic coordinates were modified prior to docking to remove extended loops and residues that are unlikely to be resolved in our density maps and may interfere with the docking of the kinesin core (see Section 3 starting on page 113 for details). Docking statistics (correlation coefficients) were taken directly from the output file of the `colores` program. Docked coordinates of kinesin and tubulin were merged

into a single PDB to reflect a complete kinesin-microtubule complex. For comparisons of docked kinesin-microtubule complexes, as well as for model-building where superimposition of different coordinates was used, the alignment of the coordinates was done using least-squares fitting with the `lsqman` program from the MapMan suite (Uppsala Software Factory (USF) [7, 173–178], and the data was visualized in PyMol (DeLano, Warren L. "The PyMOL Molecular Graphics System (2008)", DeLano Scientific, Palo Alto, California, USA, http://www.pymol.org)

Figures

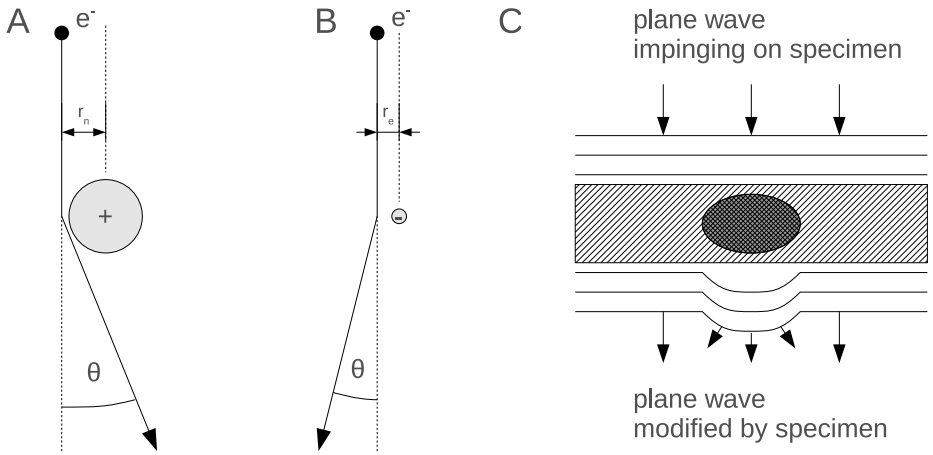

Figure 2.1 Simple models for scattering

Simple models for scattering based on a description of electrons as particles (A, B), or as waves (C).
A,B) Particle model in which nuclei are modeled as rigid spheres of positive charge and electrons as point sources of negative charge. A) Elastic scattering of electrons off a nucleus. B) Inelastic scattering off "stationary" electrons. In each case, θ is the scattering angle, and r_n or r_e denote the radial distance between the electron path and the nucleus or electron, respectively.
C) Wave model showing the incoming plane wave modified by interaction with the specimen. The phase is shifted in proportion to the thickness of the object traversed by the wave, shown as a distortion of the exiting wavefront. In this example, the wavefront is not disturbed by the medium surrounding the particle. Note, however, that native biological specimens are commonly imaged in media that scatter almost as much as the specimen itself.

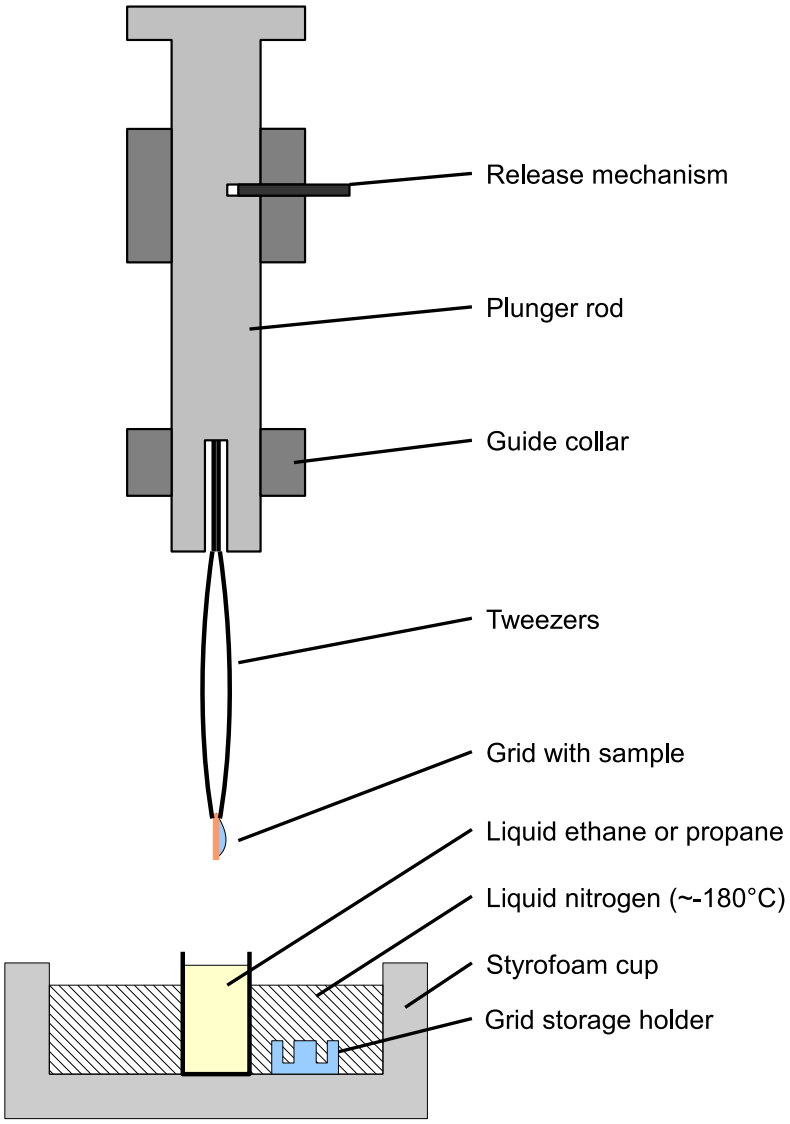

FIGURE 2.2 SCHEMATIC OF FREEZE-PLUNGING DEVICE

This schematic shows the basic setup for the freeze-plunger. Not shown are devices for atmosphere control and blotting the samples. In order to achieve rapid plunging action the plunger rod can be accelerated by springs or rubber bands (not shown). The bath with the cooling medium (ethane or propane) is cooled by liquid nitrogen, in which the sample is typically kept as well before moving it to storage.

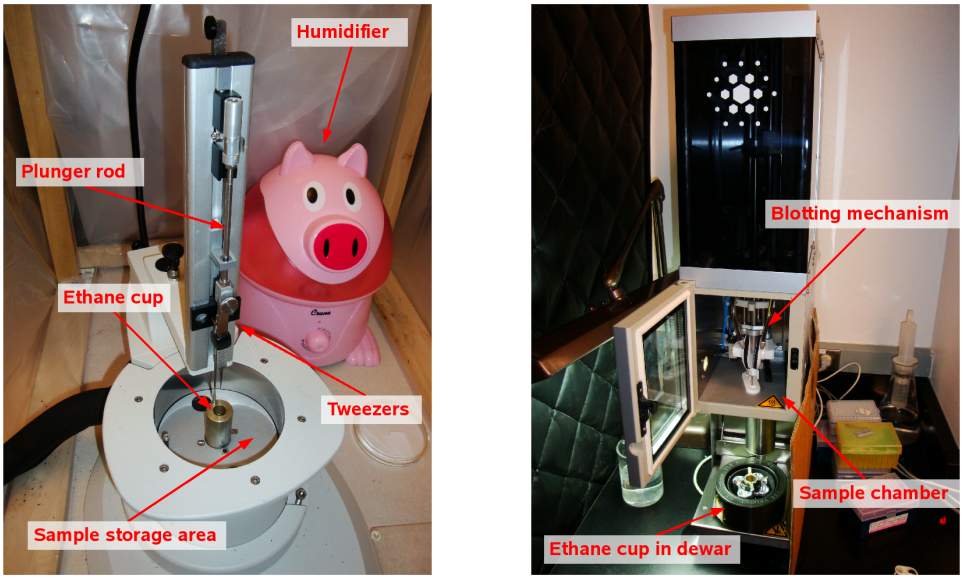

FIGURE 2.3 EXAMPLES OF FREEZE-PLUNGERS

The photo on the left side shows a manual freeze plunger (Leica, Inc.). The pig statue to the right of the freeze plunger is a creatively shaped air humidifier, and is crucial for minimizing evaporation of the sample layer from the grid. Note also that the entire setup is housed in a greenhouse-like cage. The support pillars of the cage, as well as the plastic cover, can be seen in the background.
The photo on the right shows a Vitrobot (FEI Corp.) an automated freezing machine. The black cup containing the cryo-coolant, liquid nitrogen, and samples is raised during operation. The chamber in the middle is temperature and humidity-controlled and contains the blotting disks.

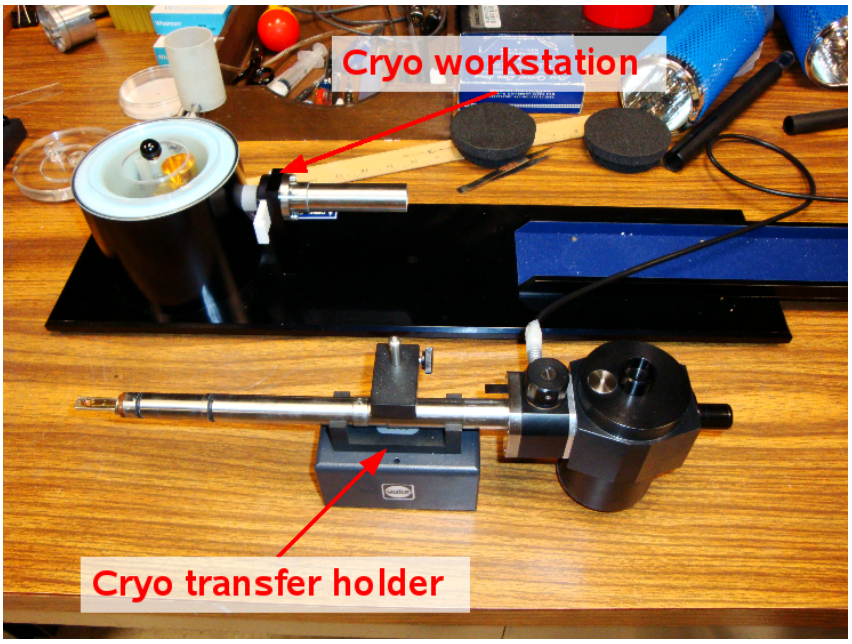

FIGURE 2.4 THE CRYO-EM SAMPLE HOLDER

In the foreground of this photo is a Gatan cryo-holder. The sample is loaded on the tip at the left side, while the dewar on the right contains liquid nitrogen to cool the sample. The cable is used to heat the tip and dewar to room temperature after observation. The cryo workstation in the background allows for the sample to be transferred to the tip under liquid nitrogen.

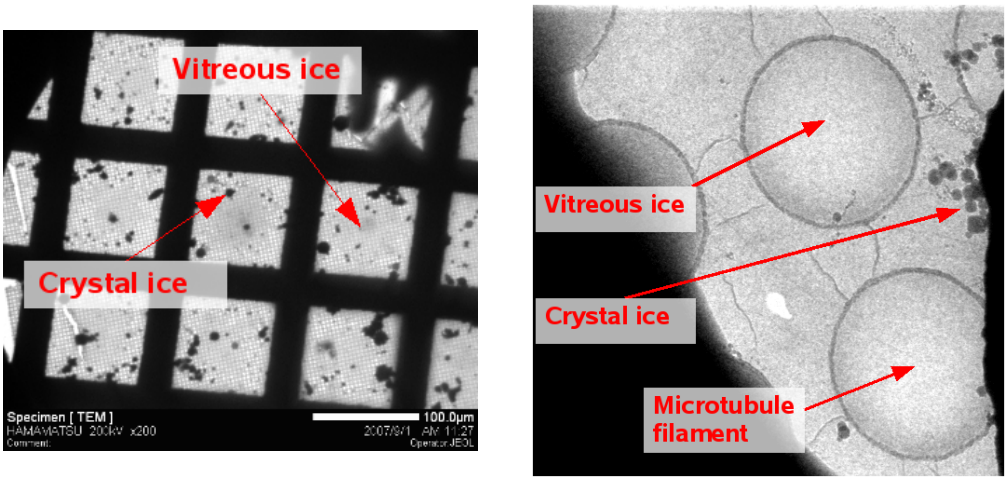

FIGURE 2.5 VITREOUS ICE

The photo on the left side shows a low magnification (200x) view of a representative frozen-hydrated sample grid. Note that *vitrified ice* can co-exist with ice crystals on the same grid, due to contamination and freezing effects.
The photo on the right is a representative close-up of vitrified ice. Note the clear contrast of the microtubule sample within the ice, and how ice crystals, presumably on the same order of thickness as the *vitreous ice*, absorb much more strongly.

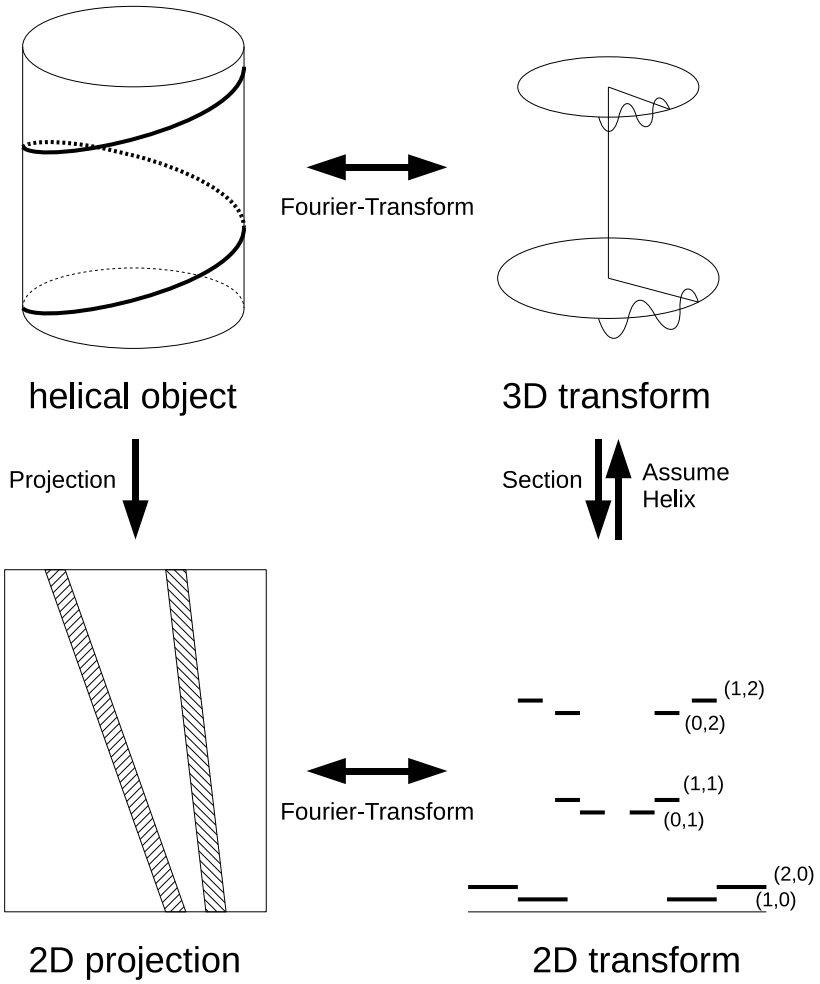

FIGURE 2.6 HELICAL IMAGE RECONSTRUCTION

A helical object (top left) is recorded in the electron microscope as a projection image (bottom left). The image is digitized (scanned) and a "diffraction image" is computed (bottom right). Strong peaks in the diffraction pattern are indexed to impose a helical lattice, allowing extrapolation to three-dimentional Fourier space (top right). Reverse Fourier transformation of the three-dimensional transform then reveals the electron potential distribution of the helical object (top left). Only half of the diffraction pattern and 3D transform are shown due to redundancy.

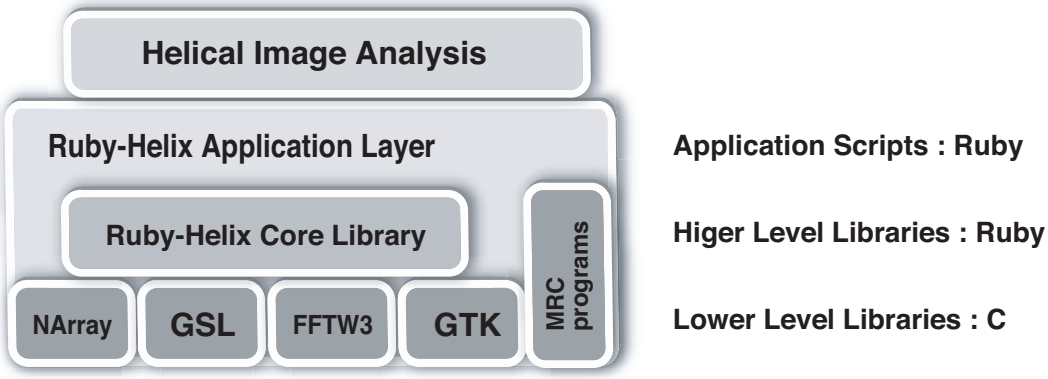

FIGURE 2.7 ARCHITECTURE OF RUBY-HELIX

This diagram shows the architecture of Ruby-Helix with the dependencies on lower level libraries and packages.

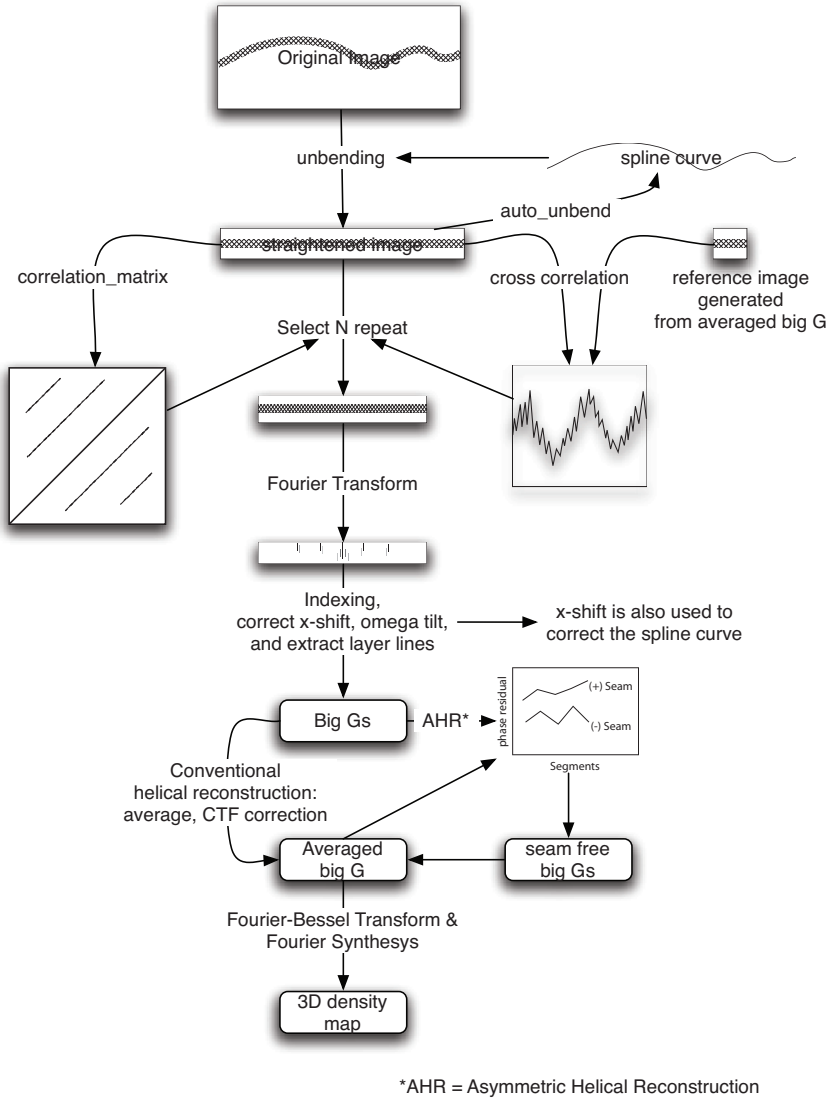

FIGURE 2.8 OVERVIEW OF HELICAL IMAGE ANALYSIS USING RUBY-HELIX

This flowchart details the process for analysis and three-dimensional reconstruction of helical objects using Ruby-Helix.

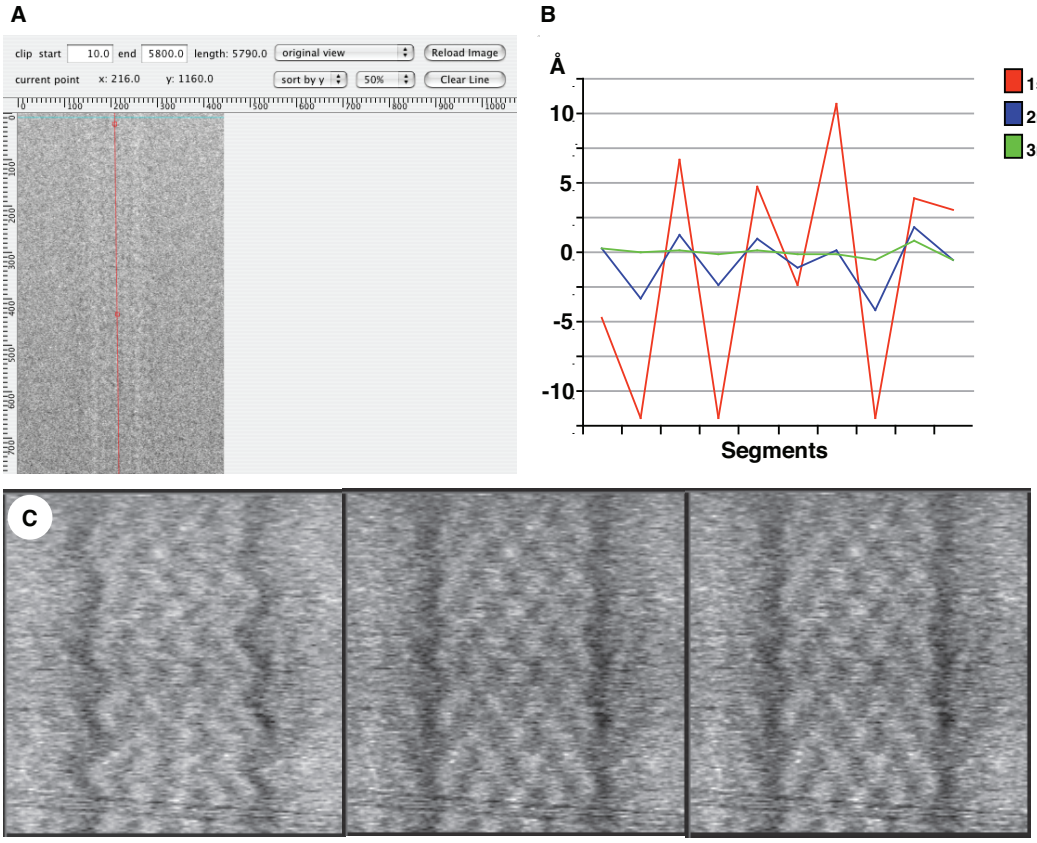

FIGURE 2.9 UNBENDING OF A FILAMENT

(A) Control panel of unbent program (top), the initial spline curve (red line), and the start of the spline curve (blue line) superimposed on the raw cryo-EM image of KIF1A-microtubule complex. Only control points set between the start and end points, as defined in the boxes at the left of the control panel, are refined. (B) Comparison of the shift detected by cross-correlation between the 1D projection of a segment and its mirrored projection. After three iterations of distortion correction by `auto_unbent`, the shift decreased to less than one pixel, which corresponds to <2.5 Å. (C) Images of the original in A, showing motor-microtubule complex over three iterations of `auto_unbent`. The images are shortened along the filament to enhance the moire pattern of the microtubule and to demonstrate the effect of unbending.

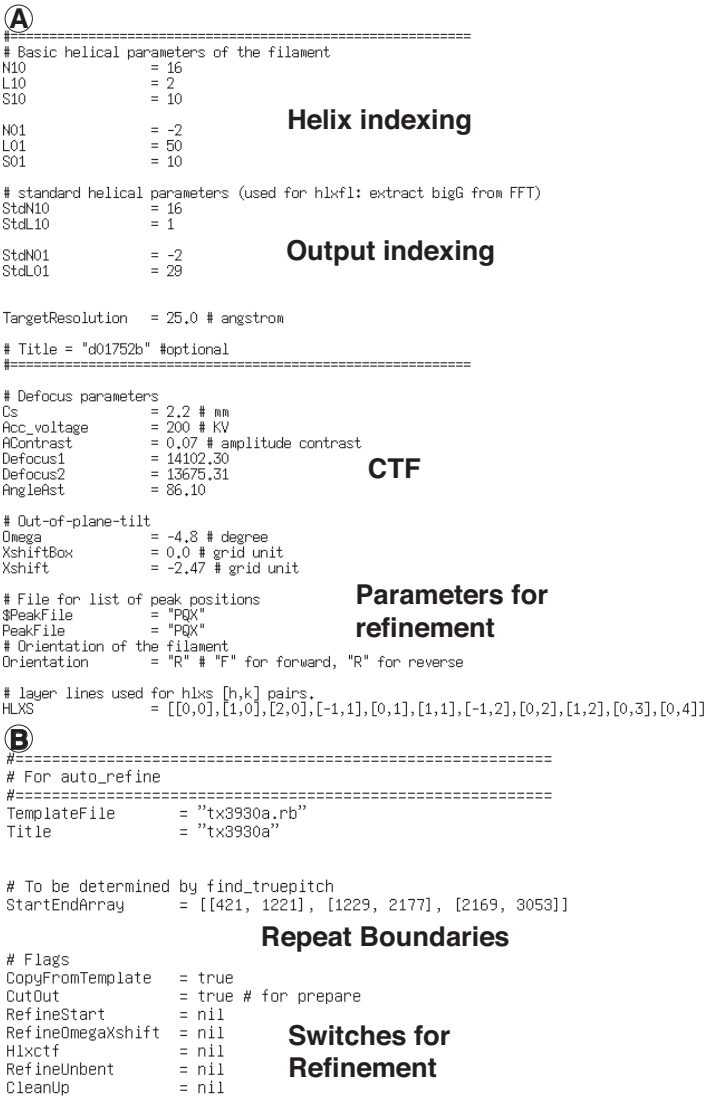

FIGURE 2.10 MASTER CONTROL FILES

(A) Part of the master control file showing important parameters for several subroutines. (B) Control switches for analysis in total.rb control file.

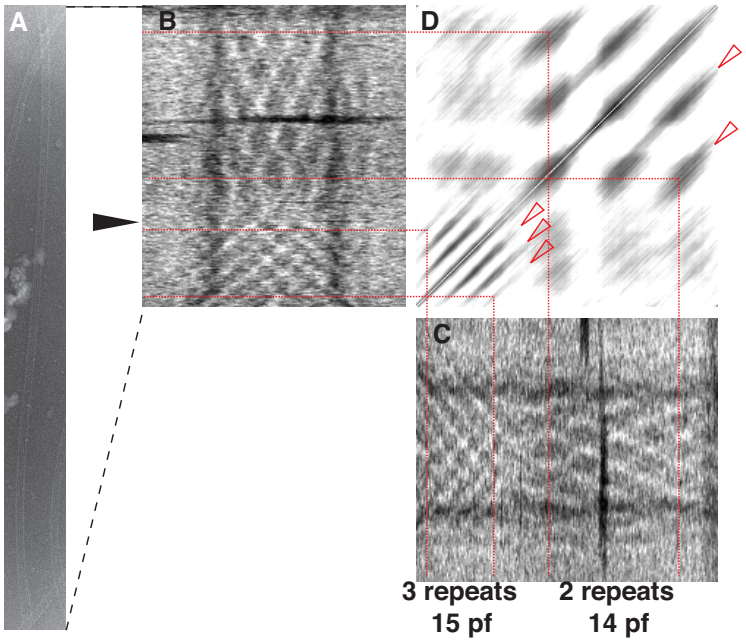

FIGURE 2.11 DETERMINATION OF THE REPEAT LENGTH USING CORRELATION_MATRIX

Determination of the repeat length using `correlation_matrix`. (A) Raw image of a kinesin-microtubule complex. (B,C) The image is straightened and shortened along the helix axis by a factor of 32. Note the change of microtubule lattice from 14 to 15 protofilaments in the middle of the microtubule, as indicated by the filled arrowhead. (D) Output of `correlation_matrix`, showing correlation between two segments of the shortened image. Dark diagonal streaks (open arrowheads) indicate higher correlation. By selecting an appropriate point in the streak, the positions of start and end of repeat(s) can be obtained.

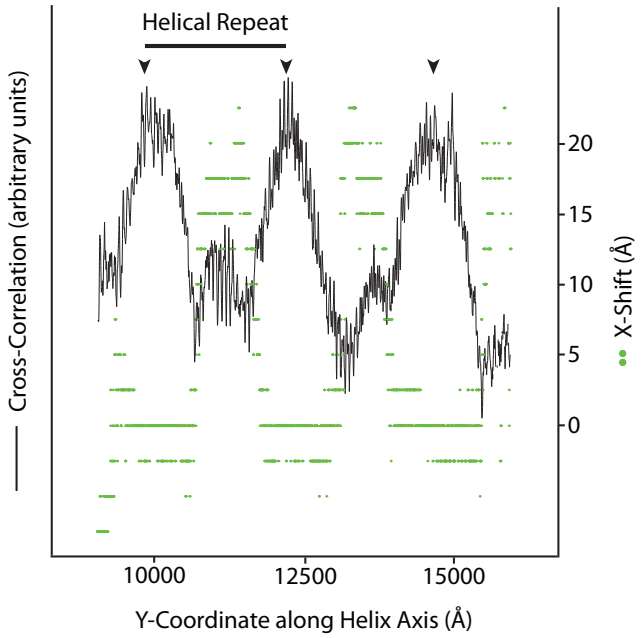

FIGURE 2.12 DETERMINATION OF THE REPEAT LENGTH USING FIND_TRUEPITCH

Determination of the repeat length using `find_truepitch`. Cross-correlation values (grey line) with peaks (arrowheads). One helical repeat is defined by the distance between two cross-correlation peaks. Smaller peaks are correlations with kinesin molecules. In-plane shift perpendicular to presumed helix axis (green dots). The discrete distribution is due to the shift being measured in pixels. Values on both axes were converted to Å based on a pixel size of 2.5 Å.

CHAPTER THREE
Results

Rationale

In order to address the structural principles underlying kinesin processivity, we have first analyzed and compared the structures of monomeric kinesin heads in complex with microtubule, as well as of processive and non-processive dimer kinesins. For our analyses, we chose constructs of the *Drosophila melanogaster* kinesin-1 heavy chain (conventional kinesin, KHC [188]), as it can be readily purified in adequate quantities and has been well characterized biochemically [97, 98, 101, 107, 135, 136, 148, 346].

The monomeric construct dKH357 [148, 149] was used to determine the nucleotide-dependent structural changes of individual kinesin heads in the absence of the constraints likely to act on the heads in processive dimers. The monomer structures therefore establish a "baseline" model for nucleotide-dependent switching of the kinesin-1 core. We have solved the kinesin-microtubule complex structures with kinesin in an ATP-like state, as well as in the absence of nucleotide. The kinesin head is strongly attached to microtubule in these states, and both are expected to play critical roles in the processive stepping of kinesin-1 (see section 1). Furthermore, these states are expected to constitute the two-head bound transition state and are therefore key to understanding kinesin processivity.

The dimeric construct dKH405 was used to determine the structures of processive and non-processive kinesins in the two-head bound transition state. Based on our hypothesis that a strain-based gating and feedback mechanism constrains the conformations of the two-head bound conformation of the kinesin motor, we

expect to find structural differences between processive (constrained) wild-type and non-processive (unconstrained) mutant dimers. Specifically, we expect the processive dimer to include one ATP-like head and one nucleotide-free head, even under conditions of saturating ATP-analog concentrations. In contrast, both heads of the non-processive mutant dimer under the same conditions are expected to be in a conformation reflecting the bound ATP-analog. Furthermore, the observed differences are expected to reflect nucleotide-dependent switching as established by the monomer constructs.

Lastly, the KIF1A-microtubule complex structure was solved by asymmetric helical analysis [162] using the Ruby-Helix package [207]. Comparison of the result with previously published results [164, 167, 168] can establish the validity and resolution range to which reconstructions obtained from asymmetric helical analysis are consistent with reconstructions obtained by conventional helical analysis.

Experimental strategy

Using cryo-electron microscopy and image analysis, we have obtained images of the kinesin head-microtubule structure in two distinct nucleotide states. This method allows the preservation of the native, hydrated state of kinesin, in the functional context of the microtubule. The construct used for this part of the study was the monomeric *Drosophila melanogaster* kinesin head dKH357. The biochemical characteristics of this construct have been shown to be consistent with those of similar kinesin-1 heads from other organisms [196–198]. These heads bind tightly to the microtubule in the presence of the ATP nucleotide analog AMPPNP ($K_d^{MT,ATP_{analog}} = 1 - 7\ \mu M$ [198]) [9, 22, 120, 123, 168] and in the absence of nucleotide ($K_d = 3\ nM$) [48, 123], and possess ATPase rates comparable to full-length wild-type kinesins [148, 149].

Using conditions that fully saturate the microtubule lattice [129, 271], we have decorated *in vitro* polymerized microtubule with the dKH357 kinesin construct, either in the presence of excess AMPPNP or apyrase (to remove any traces of ADP or ATP from the buffer). Using cryo-electron microscopy, we have then obtained images of frozen-hydrated microtubule-kinesin complexes. From these images we reconstructed the structures of the kinesin head-microtubule from 16 protofilament, 2-start microtubules by conventional helical analysis, as described in section 2 on page 83. The CTF-corrected reconstructions are shown in Figure 3.1. For the final reconstructions, 2,300 and 11,000 asymmetric units (ASU) were averaged for the AMPPNP and apo states, respectively. The resolution for the reconstructions is approximately 19 Å for the AMPPNP state and 17 Å for the apo state. The resolution cutoffs reported here are based on a Fourier Shell Correlation (FSC) cutoff value of 0.3. The FSC results are shown in Figure 3.13. The FSC statistically favors

particle numbers significantly larger than have been averaged for our reconstructions, and it is be doubtful that any single FSC threshold can accurately describe the resolution of a density map [320, 322]. Therefore, the resolution cutoff was fixed at 18 Å for all subsequent comparisons. This estimate of the signal-to-noise ratio of the reconstructions is in our opinion conservative even for the AMPPNP state.

Estimation of conformational changes

We used several methods to estimate the conformational changes involved in nucleotide-dependent switching of the kinesin-1 motor core. The results generally agree and are consistent with our expectation that the kinesin core rotates clockwise from the AMPPNP state to the apo state, in analogy to the nucleotide-dependent rotation observed in KIF1A between the ATP-like and ADP states [167], albeit of much smaller angle.

First we superimposed the reconstructions of dKH357 in the AMPPNP and apo states by aligning them in Fourier space. The result is shown in Figure 3.4A, and shows a nucleotide-dependent tilt. While it is possible that the observed density differences reflect a conformational change, the observed density differences are in fact not statistically significant by the criteria of the Student's t-test. However, in this case it may be difficult to show that the observed differences are statistically significant, because the relatively small angle of presumed rotation of the kinesin core would shift the envelope of the protein, as evidenced in the isosurface representation in Figure 3.4A. The envelope visualized by an isosurface is a choice, in this case an estimate of the protein-water interface, where electron density is expected to change abruptly. One could estimate the appropriate isosurface by enclosing a volume based on the specific weight of proteins in general, but the difficulty of estimating the protein boundary would remain, particularly for smaller proteins, because extended structures outside the protein core clearly contribute to protein mass, even though they may not be resolved. A further complication is the small difference in density

between protein and water (approximately 1.3 g/ml and 1.0 g/ml, respectively), which in turn makes estimates of protein density based on electron scattering more uncertain. Due to these factors, density gradients such as the protein envelope can be poorly defined in reconstructions. It is therefore desirable to collect evidence about the apparent conformational change using a method that takes advantage of changes in core density that may not be appropriately reflected in the isosurface representation.

To obtain further evidence for the nucleotide-dependent tilt of the kinesin-1 core apparent in the isosurface reconstructions, we have used a six-dimensional rigid-body density matching algorithm to match the densities of our constructs to densities derived from similar kinesin crystal structures. This method seeks to maximize the correlation in density between the electron density map and a density map of comparable resolution derived from the atomic coordinates. The advantage of rigid-body docking methods is that they utilize the density information in all three dimensions of the density map, rather than just the envelope represented by an arbitrarily chosen isosurface. Rigid-body docking can therefore detect density differences in the protein core, rather than relying on density gradients at the protein boundary, and is therefore more robust against noise in the density profile of the protein. Furthermore, this method can supply quantitative information of the fit between X-ray and EM-derived densities.

Care has to be taken to avoid several pitfalls of the docking procedure. First, the fit for approximately globular proteins will depend at least partly on the resolution cutoff for the reconstruction. Kinesin-derived density is sufficiently asymmetric at a resolution cutoff of approximately 20 Å or better to distinguish the orientation of the kinesin core, and our reconstructions are therefore suitable for rigid-body docking. Second, because we are interested in comparatively small conformational changes of the kinesin core, care should be taken to avoid fitting residues that are not resolved within our reconstruction or are significantly outside the kinesin core.

For this purpose, the atomic coordinates of human kinesin in the ADP (PDB ID:1BG2 [184]) and ATP-like (PDB ID: 1MKJ [270]) were used. The conformations of the chosen atomic structures represent approximations to the expected conformation in our density map. In particular, 1MKJ represents a kinesin with docked neck linker [270], as expected for the ATP-like conformation. In contrast, the neck linker is undocked and disordered in 1BG2 [184], as expected for the apo state. However, it is important to keep in mind that the crystal structures were solved in the absence of microtubule and may not fully replicate the physiologically relevant conformations. Further, the atomic coordinates were modified prior to docking as shown in Figure 3.2. In the case of 1BG2 [184], residues 239-250 were removed. In the crystal-derived atomic structure, these residues form an extended loop that clearly clashes with tubulin density when fitted to the 9 Å resolution structure of the kinesin-microtubule complex solved by Sindelar and Downing [271] and shown in Figure 3.2A. These authors could clearly resolve α-helices in their reconstruction, and the validity of their docking results could thus be easily verified through the superposition of helical densities from crystal- and EM-derived density maps, despite some obvious clashes within the loop including residues 239-250. To avoid similar clashes, as well as potential difficulties for the fitting algorithm to simultaneously include the kinesin core as well as the entirety of the extended loop within our reconstruction, we removed residues 239-250. In the case of 1MKJ [270], the neck linker was truncated at T336 to remove the residues that are part of the neck domain. The coiled coil is not resolved in our reconstrutions, likely due to conformational flexibility within the linker region. In either case, the removed residues formed densities large enough to affect the accuracy of the docking, but could either not be resolved in our density maps, or would clash with what is likely tubulin density.

Following modification of the atomic coordinates, exhaustive rigid-body fitting was performed to find solutions that explain the density differences of our reconstructions between the ATP-like and apo states. The search was performed

using the using default parameters, except for search angle increments of 2° (default is 20°), the smallest integral value allowed by the software, and the best 6-10 fits were inspected. To estimate the effect of differences among the different set of atomic coordinates on the docking, the coordinates were fitted to both the "matched" and the "mismatched" electron density map. The result of a "matched" pair is e.g. the docked coordinates for the ATP-like state of kinesin (1MKJ [270]) docked in the corresponding electron-density map (the AMPPNP state). In contrast a "mismatch" would occur if the presumed conformation of the atomic coordinate set does not match the nucleotide state of the electron density map, e.g. coordinates for the ATP-like state of kinesin (1MKJ [270]) docked in the electron-density map of the apo kinesin-microtubule complex or vice versa. Out of the combination of four fits, in all cases except one, only one unique "reasonable solution" emerged. "Reasonable solutions" were considered those that matched the kinesin atomic coordinates with known kinesin density in the electron-density map in approximately the well-established orientation for kinesin heads [127, 129, 130, 167, 168, 199, 271], as well as tubulin coordinates in the tubulin density. In the sole instance that yielded two "reasonable solutions" for kinesin, these solutions were separated by an RMSD of less than 1 Å and practically superimposed. All other ("non-reasonable") solutions fitted the kinesin atomic coordinates entirely into tubulin density. No solutions were found that were "reasonable" but were e.g. of incorrect polarity. In the case of tubulin, the 6 best fits were duplicates and eliminated as such by the fitting software, giving a single final solution approximately consistent with established data [167, 168, 190, 191, 271, 330].

The fitted coordinates of the unique "reasonable solutions" of "matched" coordinate/density map pairs are shown in Figure 3.3. To establish the basis for nucleotide-dependent conformational switching and confirm earlier results, the fits were directly compared. The results are shown superimposed in Figure 3.4 and are consistent with the nucleotide-dependent tilting of the kinesin core observed by

superposition of the isosurfaces. This result holds true even where "mismatched" atomic coordinates were used for docking (not shown). In the case of "mismatched" pairs of atomic coordinates and electron density maps, the "mismatched" coordinate set closely aligned with the "matched" set, so that the nucleotide-dependent tilt could be recapitulated even if the same atomic coordinate set was docked to both the map of the AMPPNP complex and the apo complex electron density map.

Table 3.1 lists the docking statistics as absolute and normalized correlation coefficients for pairs of atomic coordinates and electron density maps used for docking. As can be seen from the above table, the fitting scores for the AMPPNP-complex map are consistently lower than for the apo-complex map. Furthermore, while the fit for the "matched" coordinate set (1BG2 [184]) is better than that for the "unmatched" set (1MKJ [270]) for the apo-complex density map, the density matching algorithm cannot be used to distinguish "matched" and unmatched coordinate sets in the AMPPNP-complex map. This may be reflective of the lower resolution of the AMPPNP-complex map, but the fit should not be judged from these numbers alone, as "unreasonable" fits have scores in the same range.

We also applied the rigid-body docking method to fit the atomic coordinates to the microtubule portion of our density map, with the goal of building a model of the kinesin-microtubule interaction. However, the fitted tubulin atomic coordinates appeared to be consistently somewhat mismatched from the density map. In particular, the tubulin atomic coordinates appeared rotated clockwise from the direction of the protofilament density when fitted to our map of the apo complex. The resulting solution clearly placed large parts of the tubulin atomic coordinates outside of the corresponding tubulin electron density. This problem is illustrated in Figure 3.5.

Several lines of evidence suggest that this apparent mismatch may be an anomaly, but its origin is not clear. First, all the kinesin-microtubule complexes that were analyzed belong to the 16 protofilament, 2-start class. Even if residual

differences in the supertwist of the protofilament (due to extension or compaction of the helical lattice) remained after averaging the approximately 20 repeats, such differences would be far smaller than the observed rotation. Further, the overlay of the density maps from the apo and AMPPNP state complex maps shows that similarly chosen isosurfaces are approximately aligned, and differences in protofilament direction are not apparent. Second, the fit of the tubulin coordinates to the AMPPNP complex density map appears more aligned with the protofilament density than the fit of the same coordinates to the apo map, despite the high apparent similarity of the tubulin densities in the map. Nonetheless, the same problem of mismatched density mentioned for the apo map appears to affect the docking for the AMPPNP density map, though to a smaller extent. In this case, the boundaries of the electron density and the surface representation appear approximately aligned and parallel on the right side of the protofilament (with the plus-end facing up), while the parts of the atomic structure are clearly outside the tubulin density. While the origin of this problem is unclear, it does largely appear to be confined to tubulin-derived density in our maps. The fit of the kinesin atomic coordinates to the electron density maps seems consistent with expectations in that the fit is reasonably capable of explaining the appearance of the density map.

Comparison of models

Small differences in fitting due to misalignments of density maps can potentially be eliminated by comparing the complex structures based on alignment of the relatively invariant tubulin component. This can be achieved by merging the fitted tubulin and kinesin coordinates from the same electron density map, and superimposing the merged complexes using only the coordinates of the fitted tubulin atomic structure for alignment. Although the problems with fitting the tubulin density described in the preceding paragraph considerably limit the usefulness of this approach, it may nonetheless be possible to make some qualitative observations.

Here, we have compared our results with several published in the literature. The references chosen for this comparison were the complex structures of the monomeric KIF1A [164, 168], and the motor domain of the human dimeric kinesin-1 [271], both of which have been solved to sub-nanometer resolution in complex with microtubule.

First, we have compared our reconstructions to the structure of the human kinesin-1 head in complex with microtubule. For this comparison, we have superimposed the merged coordinates of the monomer kinesin head-microtubule complex in the AMPPNP state with the published coordinates of the human kinesin head in complex with microtubule (PDB ID: 2P4N [271]). As mentioned previously, the coordinates for the complex structures were in both cases obtained by independently docking atomic coordinates for tubulin (PDB ID: 1JFF [191]) and kinesin (PDB IDs: 1BG2 [184] and 1MKJ [270]) to the respective electron density map, and subsequent merging of the fitted coordinates. Due to a potentially significant error in the fitting of tubulin coordinates to our density map (described in detail on page 118) of the apo state, we opted to use instead the kinesin-microtubule complex in the AMPPNP state. The fit of the tubulin coordinates appears to be somewhat inaccurate even in the AMPPNP map, but the inaccuracy appears to be limited to a translational component in the direction perpendicular to the protofilament axis.

The superimposed complex structures are shown in Figure 3.6. As expected due to the translational component of our docking fit of tubulin, our result appears translated perpendicular to the protofilament axis. Aside from this translation, the switch II helix at the center of the microtubule-binding interface appears to align well, consistent with our expectation. Further apparent is a counter-clockwise tilt of the kinesin in our complex from the kinesin in the reference. Disregarding the sideways translation, this tilt appears consistent with our results reported earlier (see Figure 3.4).

Currently, no published structures of the kinesin-1-microtubule complex are available with kinesin in the ATP-like state, and a direct comparison of our data

is therefore not possible. Based on our previous observation that the the switch II microtubule-binding region appears to align well between our complex in the AMPPNP state and the published kinesin-1 microtubule complex in the apo state, we have constructed a simulation of the ATP-like conformation based on aligning the microtubule-binding region of the atomic coordinates of human kinesin in the ATP-like state (PDB ID: 1MKJ [270]) with the microtubule-binding region of kinesin in the published apo complex (PDB ID: 2P4N [271]). The superimposed structures are shown in Figure 3.7A-C. The simulation highlights several features of the proposed nucleotide-dependent conformational change. First, the nucleotide-induced conformational change appears to be small with respect to changes in the core density. In fact, a conformational change of this magnitude may be resolved by cryo-electron microscopy only at resolutions below 1 nm. Second, there is a clockwise nucleotide-dependent tilt of the core from the ATP-like to the apo state. The angle of this tilt appears similar to that suggested by our results (see Figure 3.4), but the axis of rotation appears to be closer to the minus-end proximal (lower) part of kinesin. In contrast, the axis of rotation in our reconstructions appear to be within the (upper) "nose" structure of kinesin, distal to the minus end.

Several explanations are possible to explain this discrepancy. One is that density from the docked neck linker near the "nose" of kinesin towards the plus-end is deformed by neck linker binding. Evidence for such deformation has been reported recently [140, 161], and may obscure structural features at resolutions comparable to what our study is reporting. Another possibility is that the conformation of kinesin in the presumed ATP-like state does not fully reflect the conformation of the same kinesin when in complex with microtubule. While the neck linker is indeed docked in the crystal, it is possible that the bound nucleotide (ADP) does not allow kinesin to adopt a fully ATP-like conformation. It is certainly worth noting that the bound nucleotide in the crystal structures of the ATP-like state (PDB ID: 1MKJ [270]), as well as in the ADP and apo states (PDB IDs: 1BG2 [184] and 2P4N

[271]) is ADP. This raises the question whether the nucleotide alone fully controls conformation in kinesin in the absence of microtubules [163]. Lastly, the assumption upon which our model was built, that the switch II microtubule-binding region of kinesin should closely overlap in ATP-like and apo states may be fundamentally flawed. Nucleotide-dependent switching in the monomeric KIF1A suggests that there may be considerable conformational changes within the switch II helix, leading to possible variations from perfect alignment of the microtubule-binding region [168].

Taken together, our results suggest a nucleotide-dependent conformational change of the kinesin core. Our data suggest that the kinesin head is more closely aligned with the protofilament axis when bound to the ATP analog AMPPNP, while it is tilted clockwise when no nucleotide is bound. Our apo structure is consistent with a previously published model [271], while a model for the AMPPNP state has not been published at comparable resolution. Our proposed model for this conformational appears to be consistent with a similar model proposed for the monomeric kinesin KIF1A [168]. Nonetheless, due to several problems arising partly from the limited resolution of our maps, it will be necessary to re-evaluate our data when higher-resolution density maps are available.

Structural basis for processivity

Experimental strategy

To directly assess the structural basis for coordination in dimer kinesin, we have also solved the microtubule-bound structures of processive wild-type kinesin and a non-processive mutant in the two-head bound transition state. The recombinant wild-type kinesin construct has a core motor domain identical to that used for the determination of nucleotide-dependent switching in the previous section, but the wild-type protein includes a longer neck domain for dimerization. The non-processive mutant is identical to wild-type, except for a 12-residue insertion in the neck linker, C-terminal to the start of the coiled-coil neck domain. The location of the insertion in the homologous human kinesin is marked in Figure 3.2B as the color change from the neck linker (red) to the neck-coil (green) [107]. The biochemical characteristics of the wild-type construct are consistent with those of similar dimeric kinesin constructs [196–198], including half-site release of ADP upon microtubule binding [148, 149]. The mutant construct also has ATPase and binding properties similar to the wild-type, but does not exhibit half-site ADP release. Instead, it releases most of its bound ADP upon microtubule-binding, leading to approximately 3-fold decrease in kinetic processivity [107].

Based on our hypothesis of a strain-based gating and feedback mechanism that constrains the conformations of the heads in a two-head bound dimer, we expect to find structural differences between processive (constrained) wild-type and non-processive (unconstrained) mutant dimers. Specifically, we expect the processive dimer to include one head in the ATP-like conformation and one head in the apo conformation, even under conditions of saturating AMPPNP concentrations. In contrast, the heads of the non-processive mutant dimer under the same conditions are expected to be in a conformation reflecting the bound ATP-analog. The observed

differences are expected to reflect nucleotide-dependent switching as established by the monomer constructs.

The strategy for data collection and analysis is the same outlined for the monomeric constructs, including the helical class of microtubule used for analysis and helical averaging. While this approach facilitates the comparison of datasets from monomers and dimers, the interpretation of the results is more challenging. Due to the expected helical averaging of two different conformations in the wild-type dimer, the reconstruction for this construct is expected to represent an intermediate conformation with density contributions from both nucleotide states present. Another consideration particular to dimeric kinesin constructs in complex with microtubule concerns the saturation of the microtubule lattice. Several studies using dimeric kinesins have used conditions where the kinesin motor domains were in excess over avaliable binding sites. In these cases, the unbound heads generally appeared as partial densities, mostly near the kinesin "nose" [123, 124, 129]. Furthermore, the conformation of the bound head is then expected to reflect the bound nucleotide, as in the case of monomers, due to the lack of strain on the neck linker. To avoid this problem, we have used conditions that favor a two-head bound state.

Technical considerations

We used several methods to compare our results for the dimer kinesins with the earlier results from the monomers. The results from the wild-type kinesin are consistent with our expectation. Difficulties during the reconstruction of the mutant dimer prevented a meaningful structural comparison of processive and non-processive kinesins, however. Nonetheless, we have established that it is in principle possible to distinguish processive dimers with "mixed" nucleotide state from non-processive dimers in which both heads have the same nucleotide state.

In obtaining the reconstruction for the dimer kinesins, we had to consider two complicating issues. The first is that oversaturation of the microtubule lattice

would lead to kinesin-microtubule complexes with a head attached to the microtubule, while the second head is unbound (tethered). The tethered heads typically appear as partial densities ahead of the bound head [123, 124, 129]. In the case of fractional oversaturation, however, the density attributed to the bound head can be "contaminated" with density from the tethered head. This condition may complicate the interpretation of the density map, because the tethered head density is typically found near the beginning of the neck coiled-coiled (the start of the green region in Figure 3.2) and can obscure the nucleotide-dependent tilting of the core, even at resolutions better than 20 Å. Furthermore, because no strain is acting on the heads, we would expect to preferentially reconstruct the ATP-like state when AMPPNP is present. In our sample conditions [130], the binding of both heads to microtubule was strongly favored, and none of our reconstructions showed density from tethered heads. It is therefore possible to decorate microtubule with two-head bound kinesin dimers and to reconstruct the "mixed" state of dimer kinesin using helical analysis.

The second complication of using helical analysis to determine the structures of dimer-kinesin-microtubule complexes with two bound heads arises due to the helical averaging process itself. Kinesin dimers bind randomly to the microtubule lattice, and helical averaging will therefore produce an average of the two conformations, even in the best case of fully decorated microtubule with a kinesin:tubulin ratio of 1:1. By using this ratio, therefore, we expected to obtain the average conformation between the leading and trailing heads. Depending on the degree of difference between the states under study, this averaging step may lead to difficulty interpreting the result. However, it can be assumed that the resulting "intermediate" conformation can be interpreted in terms of the underlying nucleotide states, as previously determined for the monomers kinesins. This assumption is based in part on Hackney's finding that the kinesin neck linker plays a major role in regulating the ATPase activities of the heads [107], and also on the finding that structural state of

a microtubule-bound monomeric kinesin head represents the underlying nucleotide state [164, 168]

Despite the technical feasibility of distinguishing a "mixed" state dimer from a "pure" state dimer, it is practically difficult to test our hypothesis using helical analysis. Due to the high similarity of kinesin in the two nucleotide states, considerably higher resolution than we obtained is required to unambiguously indentify nucleotide-dependent conformation changes in kinesin-1. Even better resolution is then required to distinguish "mixed" states from "pure" states. Nonetheless, using the wild-type dimer kinesin, we were able to demonstrate the technical feasibility of reconstructing microtubule-bound dimer kinesins.

Comparisons of monomeric and dimeric kinesins

We were able to reconstruct using helical analysis the structures of dimeric kinesins bound to microtubule under conditions that favor the binding of both heads to microtubule (i.e. motor domain/tubulin-dimer ratio of 1:1 [130]). The CTF-corrected reconstructions are shown in Figure 3.8. For the final reconstructions, 23,000 and 31,000 asymmetric units (ASU) were averaged for the wild-type and mutant constructs, respectively. The resolution cutoff for the reconstructions is approximately 17 Å for the wild-type and 18 Å for the mutant, as shown in Figure 3.1. As before, the resoution cutoffs reported here are based on a Fourier Shell Correlation (FSC) cutoff value of 0.3, and the maps were compared using a resolution cutoff of 18 Å.

To compare the reconstructions and test our hypothesis, that the kinesin heads in a wild-type dimer should be in different conformations, we have aligned and superimposed the density maps of monomeric kinesins as well as dimeric kinesins. The superimposed density maps are shown in Figure 3.9. The appearance and conformation of the wild-type dimer is generally consistent with that of the monomers. Due to the comparatively small degree of nucleotide-dependent tilting

of the kinesin core at this resolution cutoff, it is not possible to determine whether the wild-type dimer is in a "mixed" conformation.

The appearance of the non-processive mutant surprisingly is different from that of the other constructs, despite similar sample preparation and imaging conditions. It appears significantly smaller and more globular than the other constructs, and its conformation cannot be accurately determined. The most likely reason of the smaller appearance of the mutant is that the construct is unable to fully saturate the microtubule lattice. This is confirmed by the comparison of density profiles, plots of density along the microtubule axis, for the wild-type and mutant reconstructions shown in Figure 3.10. It is likely that the 12 additional residues in the neck linker of the mutant make many more combinations of binding sites accessible to the heads. The resulting bound dimers may therefore be separated by several tubulin subunits, either along the protofilament axis, laterally, or both. The neck linkers and neck domains that connect the heads can then adopt many different conformation, and it is conceivable that they partially occupy one or several binding sites, thus preventing the binding of additional dimers. Other explanations are also possible that may give further insight into the mechanism of processivity and are discussed in the next chapter.

To estimate the degree to which our expectation of a "mixed" conformation might be reflected in the density map of the wild-type or mutant dimer kinesin, we have used the rigid-body density matching algorithm used for the monomeric constructs. The results from the docking are shown in Figure 3.11. The conformation shown in this result should not be taken as evidence of the dimer kinesin adopting a conformation either towards the ATP-like or apo state. Rather, this was done to estimate the degree of correlation between the EM-derived density map and a crystallographic map of comparable resolution. As can be seen from the docked result and Table 3.1, the correlations for the fit are comparable to those for the monomeric constructs. Further, while the density map closely overlap with either nucleotide

state for the monomer, the density on the right side of the molecule seems to be more similar to the apo state, in that density that is present in the ATP-like state is missing from the wild-type dimer. More work is required to confirm this finding, but it is consistent with the expectation that only half of the heads in the dimer have docked neck linkers.

Asymmetric helical reconstruction using Ruby-Helix

Using Ruby-Helix to apply our new method, asymmetric helical reconstruction, we were able to analyze several microtubules in our test data set, to select successfully seam-free layer line data and to reconstruct the three-dimensional structure of a kinesin-microtubule complex from experimental cryo-electron microscopy images. The overall procedure is shown in Fig. 3.12A. The procedure was applied to a data set of five microtubules containing 17 helical repeats. Resolution for the alignment was limited to 25 Å. The initial big G data was obtained by averaging both near and far sides of a long microtubule that contains approximately four repeats, regardless of the seam position. The 0th iteration denotes that the far and near sides of each repeat were aligned independently to this "crude" reference, and averaged. At this point, phase residuals used to judge the fit of each repeat to the reference tend to show no clear pattern (not shown). For the following iterations, the average structure of the previous iteration is used as reference for the next. Furthermore, at the end of each iteration, the 10% data showing the highest phase residuals at the 8nm layer line (of Bessel order -1.5), are discarded from the next iteration. This method preferentially should exclude seam-containing sides from further averaging.

To demonstrate that seam sides are preferentially excluded during the procedure, a kinesin-microtubule complex not included in the above dataset was aligned to each of the average structures obtained from iterations 0 to 2 (Fig. 3.12B,C). As can be noted by comparing the plots in B, phase residuals vary across the length of the microtubule, for both seam side and seam-free side. Nonetheless, after 2 iterations of refinement, the phase residual difference between the seam-containing side and the seam-free side has considerably increased, as shown by arrows.

To demonstrate the validity of the above procedure, three-dimensional density maps of the KIF1A-microtubule complex were reconstructed from 14 protofilament microtubules using asymmetric helical reconstruction, as well as from 15 protofilament microtubules using conventional helical reconstruction. For 14 and 15

protofilament microtubules, 22,000 and 80,000 asymmetric units were averaged, respectively. Typically, indexing used for these reconstructions are: $(\nu, l) = (15, 1), (-2, 19)$ for 15-protofilament microtubules and $(\nu, l) = (14, -1), (-1.5, 45)$ for 14-protofilament microtubules. For comparison, both density maps are shown at 17 Å resolution (3.12D,E). Visual inspection of the two structures as well as the difference map (not shown) show no significant difference, demonstrating the validity of asymmetric helical reconstruction.

Using the above two characteristics, it was possible to progressively select seam-free layer line data and reconstruct the three-dimensional structure of a kinesin-microtubule complex from experimental cryo-electron microscopy images. The overall procedure is shown in Fig. 3.12A. The procedure was applied to a data set of five microtubules containing 17 helical repeats. Resolution for the alignment was limited to 25 Å. The initial big G data was obtained by averaging both near and far sides of a long microtubule that contains approximately four repeats, regardless of the seam position. The 0th iteration denotes that the far and near sides of each repeat were aligned independently to this "crude" reference, and averaged. At this point, phase residuals used to judge the fit of each repeat to the reference tend to show no clear pattern (not shown). For the following iterations, the average structure of the previous iteration is used as reference for the next. Furthermore, at the end of each iteration, the 10% data showing the highest phase residuals at the 8nm layer line (of Bessel order -1.5), are discarded from the next iteration. This method preferentially should exclude seam-containing sides from further averaging.

To demonstrate that seam sides are preferentially excluded during the procedure, a kinesin-microtubule complex not included in the above dataset was aligned to each of the average structures obtained from iterations 0 to 2 (Fig. 3.12B,C). As can be noted by comparing the plots in B, phase residuals vary across the length of the microtubule, for both seam side and seam-free side. Nonetheless, after 2 iterations of refinement, the phase residual difference between the seam-containing side

and the seam-free side has considerably increased, as shown by arrows.

To demonstrate the validity of the above procedure, three-dimensional density maps of the KIF1A-microtubule complex were reconstructed from 14 protofilament microtubules using asymmetric helical reconstruction, as well as from 15 protofilament microtubules using conventional helical reconstruction. For 14 and 15 protofilament microtubules, 22,000 and 80,000 asymmetric units were averaged, respectively. Typically, indexing used for these reconstructions are: $(\nu, l) = (15, 1), (-2, 19)$ for 15-protofilament microtubules and $(\nu, l) = (14, -1), (-1.5, 45)$ for 14-protofilament microtubules. For comparison, both density maps are shown at 17 Å resolution (3.12D,E). Visual inspection of the two structures as well as the difference map (not shown) show no significant difference, demonstrating the validity of asymmetric helical reconstruction.

Summary and conclusions

In summary, we have elucidated nucleotide-dependent switching in kinesin-1, and have found that the conformational change in kinesin-1 is analogous to the nucleotide-dependent tilting of the KIF1A monomer. In contrast to the extensive conformational change of the core seen with KIF1A [167] between the ATP-like and apo/ADP states, the analogous change in kinesin-1 is very small.

We have also compared the two-head bound states of processive wild-type and non-processive mutant dimer kinesins. We have generally demonstrated that two-head bound kinesins can be studied by helical image analysis methods. Our results have shown that the wild-type kinesin is similar in terms of appearance and conformation to the monomer kinesins. A non-processive mutant has been found to be deficient in its ability to decorate the microtubule lattice, in contrast to wild-type dimer and monomer kinesins.

Overall, we were unable to directly address the structural basis of kinesin-1 processivity in our studies. Nonetheless, we have gained valuable new knowledge about nucleotide-dependent switching in kinesin-1, and our results open several new avenues to explore the basis of kinesin processivity. These ideas will be discussed in the next chapter.

Lastly, we have successfully demostrated the validity and robustness of our new method, asymmetric helical analysis, by applying the method to experimental cryo-EM images.

Figures

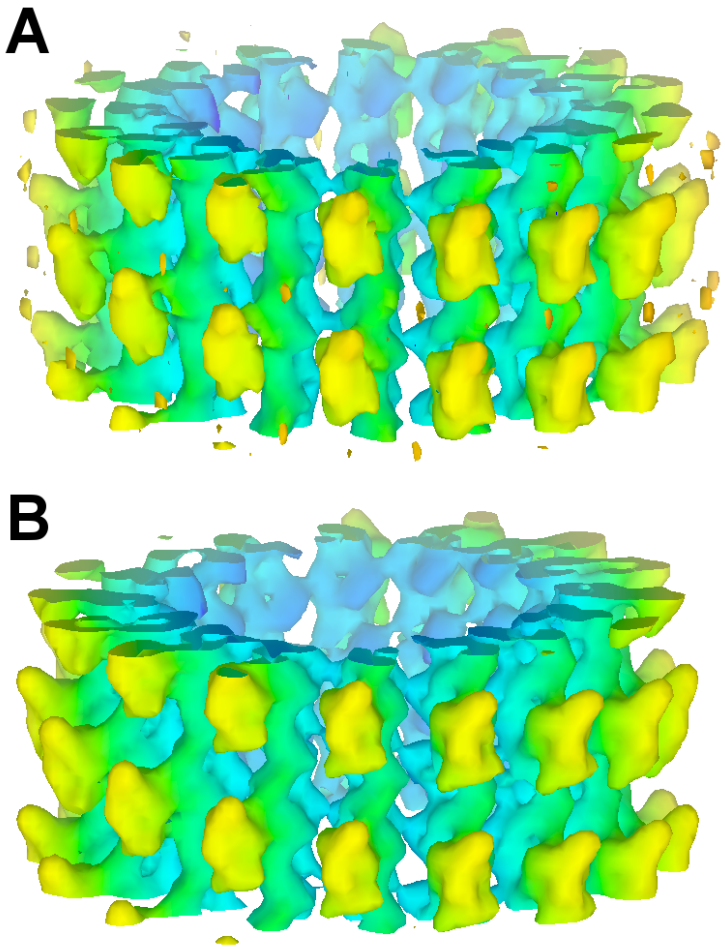

Figure 3.1 Reconstructions of monomer kinesin

Structures of a monomeric kinesin construct (dKH357) in ATP-like (A) and apo (B) state. Reconstructions were obtained by conventional helical analysis, filtered to 18 Å, and adjusted to show similar isosurfaces. Color varies by radius from inside (blue) to outside (orange).

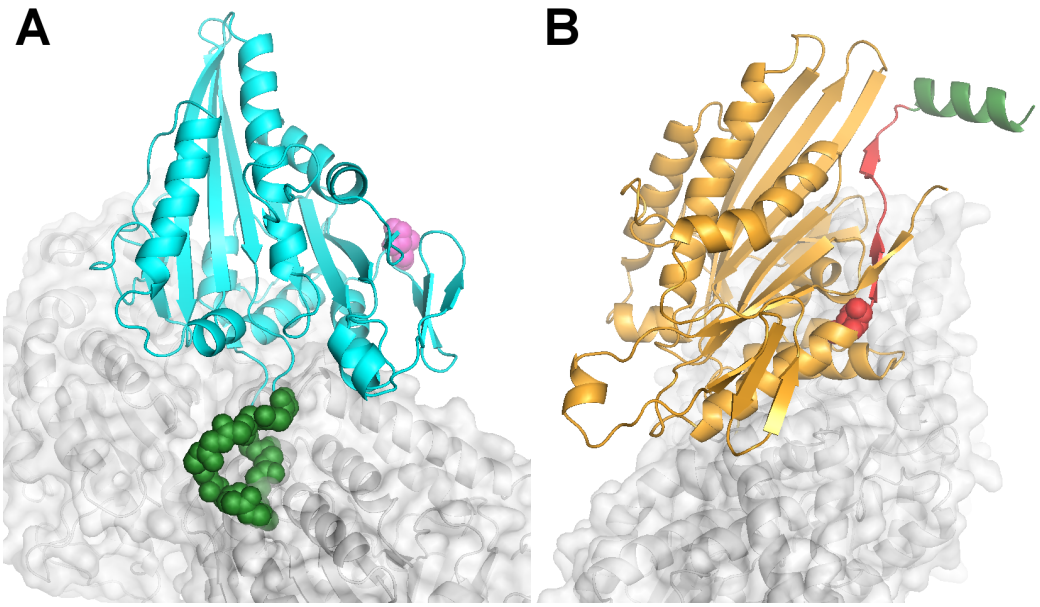

FIGURE 3.2 MODIFIED PDB'S FOR RIGID-BODY DOCKING

Atomic coordinates of human kinesin highlighting modifications performed prior to rigid-body docking to our density maps. Removed residues are colored green.
(A) Apo state (PDB ID: 2P4N [271], cyan), with residue I325 at the start of the neck linker shown as magenta spacefill. Plus-end of microtubule is facing toward upper left. Main-chain atoms of the removed residues in are shown in spacefill for clarity and to highlight clashes with tubulin density.
(B) ATP-like state (PDB ID: 1MKJ [270], orange), with the neck linker shown in red and residue I325 at the start of the neck linker shown as spacefill. Plus-end of microtubule is facing toward upper right.
Tubulin coordinates (grey surface) are part of the apo-structure of human kinesin, which was solved in complex with microtubule by cryo-electron microscopy. The original study derived the coordinates for the apo state from independent docking of PDB ID's 1JFF (tubulin [191]) and 1BG2 (human kinesin, ADP-state [184]) to the EM-derived density map and subsequent merging of the results [271]. For (B), the tubulin density was placed in a similar location with respect to kinesins microtubule-binding interface as in (A), and is shown only for orientation.

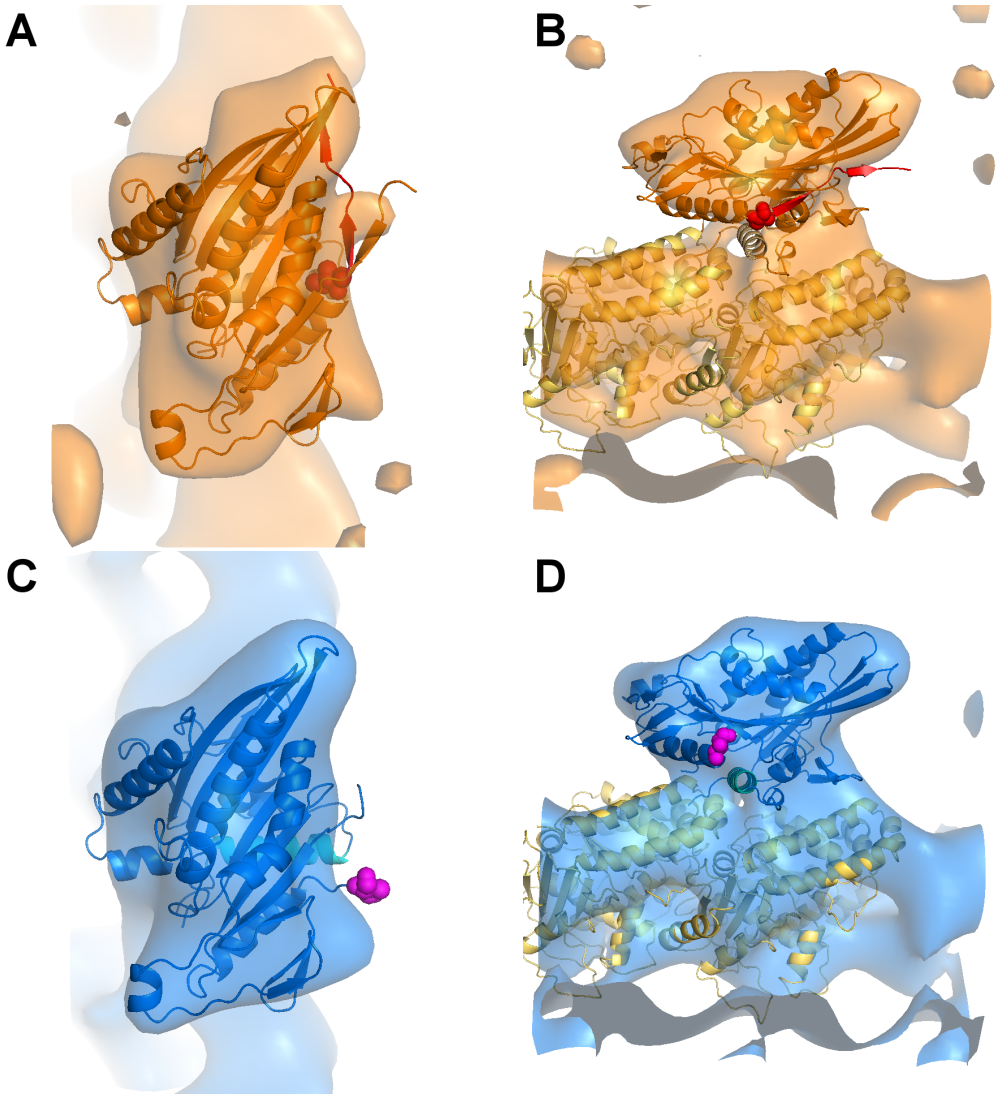

FIGURE 3.3 DOCKING OF MONOMER KINESINS

Atomic coordinates of representative kinesins docked to the density maps of monomer kinesin construct dKH357 in AMPPNP (A,B) and apo (C,D) states. The atomic structures are of human kinesin (PDB ID: 1MKJ [270]) in ATP-like state with neck linker docked (red) and in apo/ADP state with neck linker undocked and disordered (PDB ID: 1BG2 [184]). Density maps were filtered to 18 Å resolution, and atomic coordinates were modified to facilitate docking (see Methods). The docked neck linker in 1MKJ is colored red, and residue I325 at the start of the neck linker of each molecule is shown as spacefill. The side view includes the docked coordinates of tubulin (gold; PDB ID: 1JFF [191])

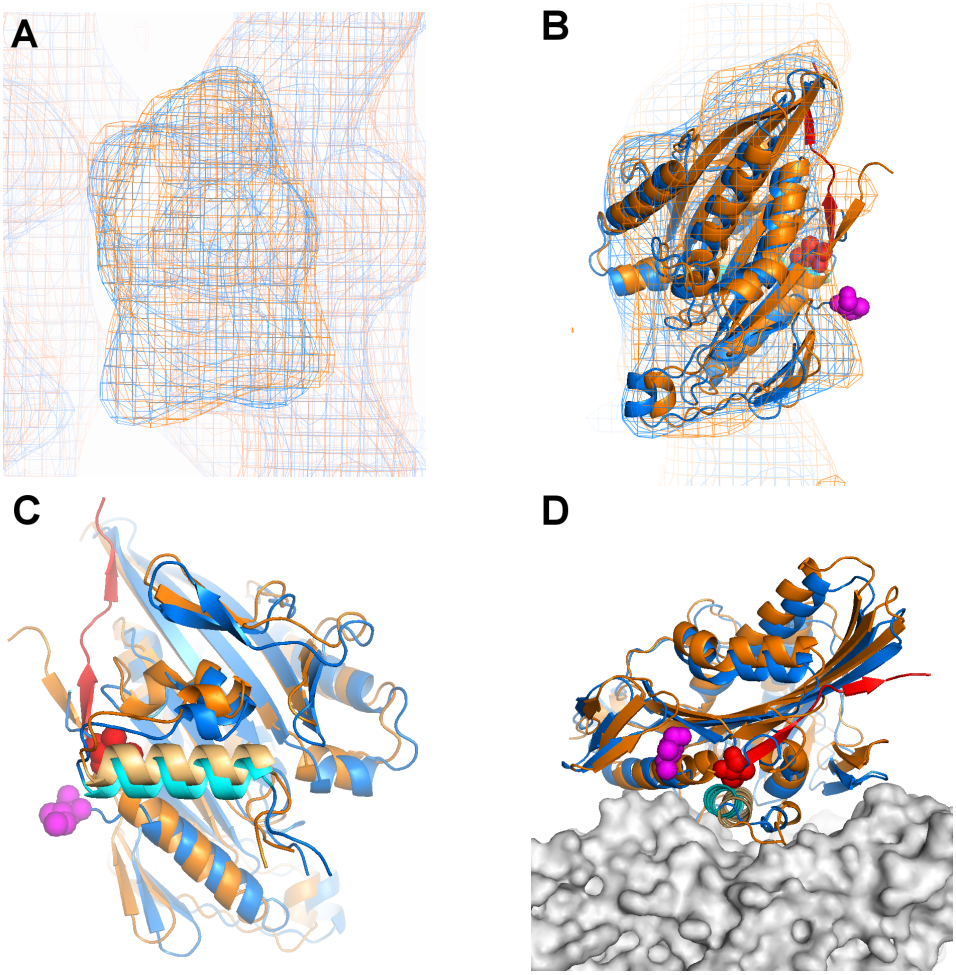

FIGURE 3.4 COMPARISON OF MONOMER KINESINS

Comparison of docked kinesin-microtubule structures showing differences in kinesin core orientation relative to microtubule. AMPPNP state is shown in orange, apo state in blue, and tubulin as grey surface. (A) overlay of density maps aligned in Fourier space with plus-end facing up, view approximately perpendicular to microtubule axis. (B) view of docked structures from the outside of the microtubule, approximately perpendicular to the protofilament axis; plus-end is facing up. (C) view looking at microtubule-binding interface of kinesin, approximately radially from the protofilament axis; plus-end is facing up. (D) side view with plus-end facing right. The Switch-II helix of each kinesin is colored in a lighter shade of the original color; the docked neck linker in 1MKJ [270] is colored red, and residue I325 at the start of the neck linker of each molecule is shown as spacefill.

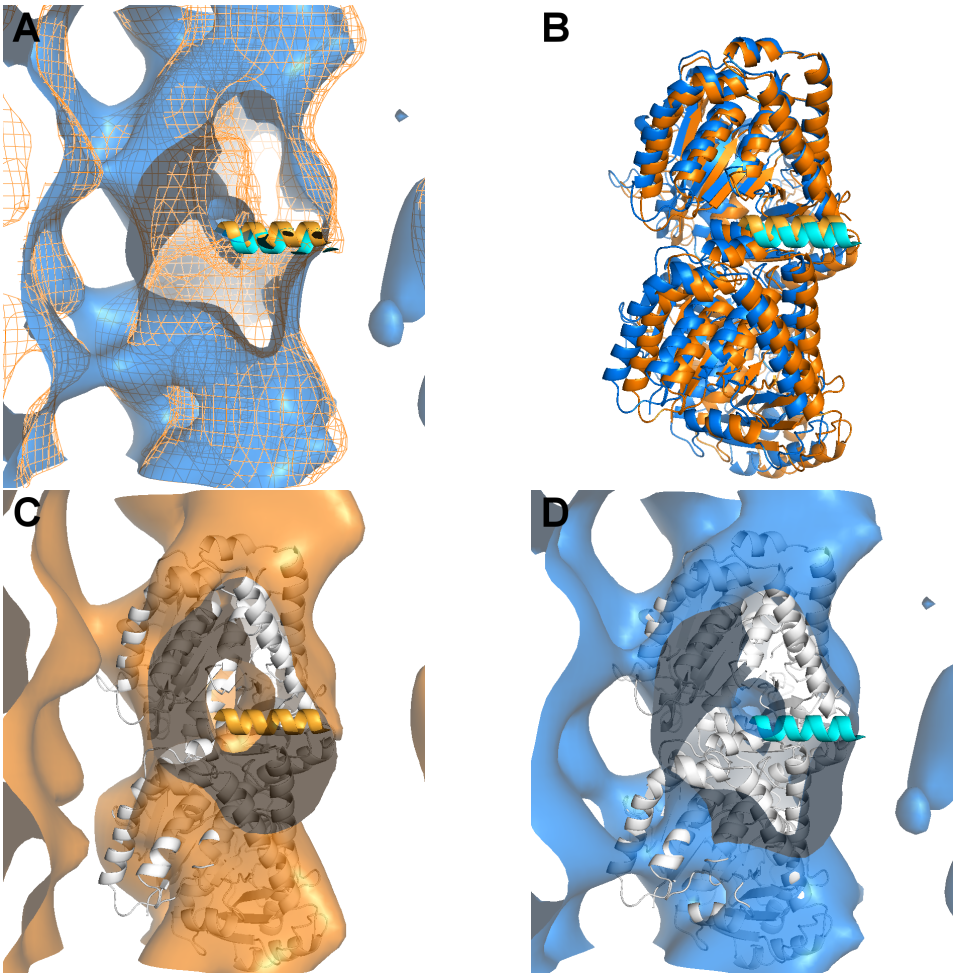

FIGURE 3.5 TUBULIN DOCKING ARTIFACTS

Comparison of docking performance of tubulin atomic coordinates using aligned density maps. Kinesin density has been cut away, but the switch II helix of the docked kinesin is shown for reference in cyan (apo) or orange (AMPPNP) state. Density maps for apo (blue) and AMPPNP (orange) states were adjusted to show similar isosurface levels that are identical across all panels. Tubulin is shown in grey in (C,D), and the plus-end is facing up. (A) overlay of density maps aligned in Fourier space, view approximately perpendicular to microtubule axis. For clarity, the density map for the apo state is shown as blue isosurface, and the map for the AMPPNP state as orange mesh. (B) superposition of the docked coordinates to the electron density maps, shown in the colors of the density maps to which they were fitted. (C) view of the fitted tubulin coordinates to the density map of AMPPNP state. (D) view of the fitted tubulin coordinates to the density map of apo state.

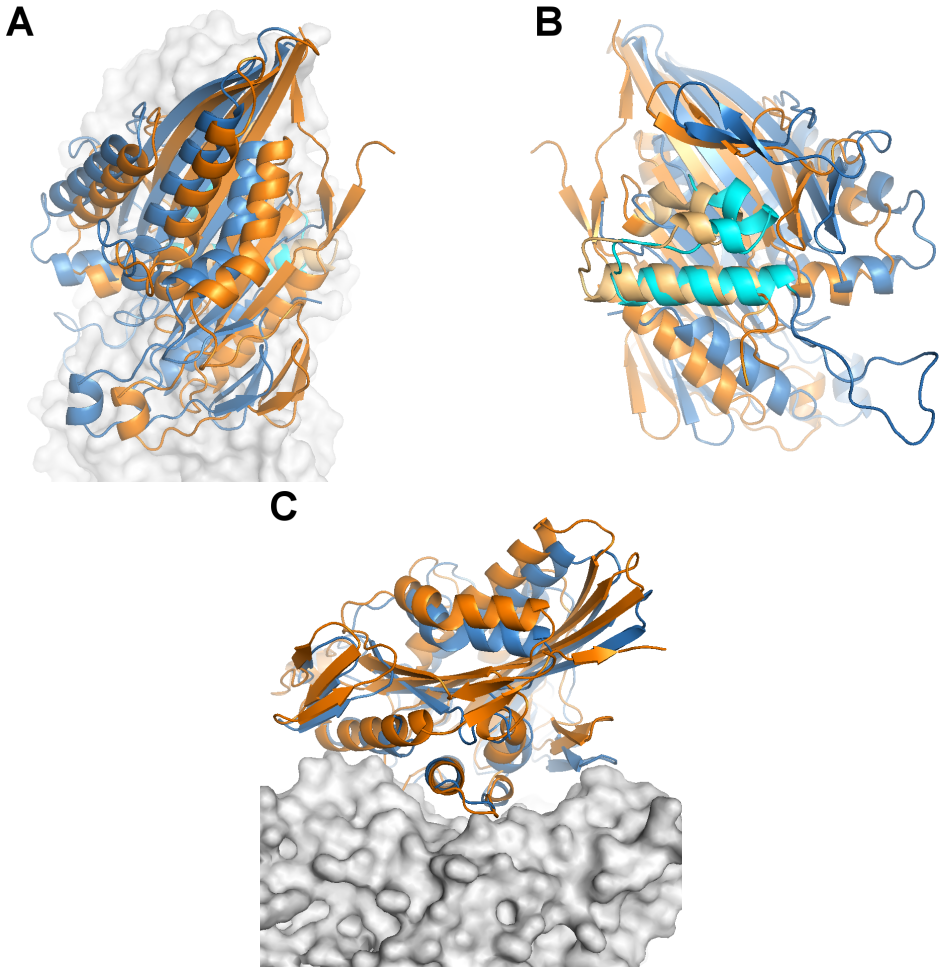

FIGURE 3.6 COMPARISON WITH REFERENCE STRUCTURE

Comparison of our model of the AMPPNP state with a published model for the apo state of human kinesin [271]. For this comparison, the docked tubulin coordinates of dKH357 in AMPPNP state were aligned with tubulin coordinates in the reference structure. The model for the AMPPNP state (docked coordinates of PDB ID: 1MKJ [270]) is colored orange and the reference structure (PDB ID: 2P4N [271]) blue, with the main microtubule-binding site around the switch II helix shown in a lighter shade of the original color. Tubulin is shown as a grey surface.
(A) view from the outside of the microtubule, approximately perpendicular to the protofilament axis; plus-end is facing up.
(B) view looking at microtubule-binding interface of kinesin, approximately radially from the protofilament axis; plus-end is facing up.
(C) side view with plus-end facing right.

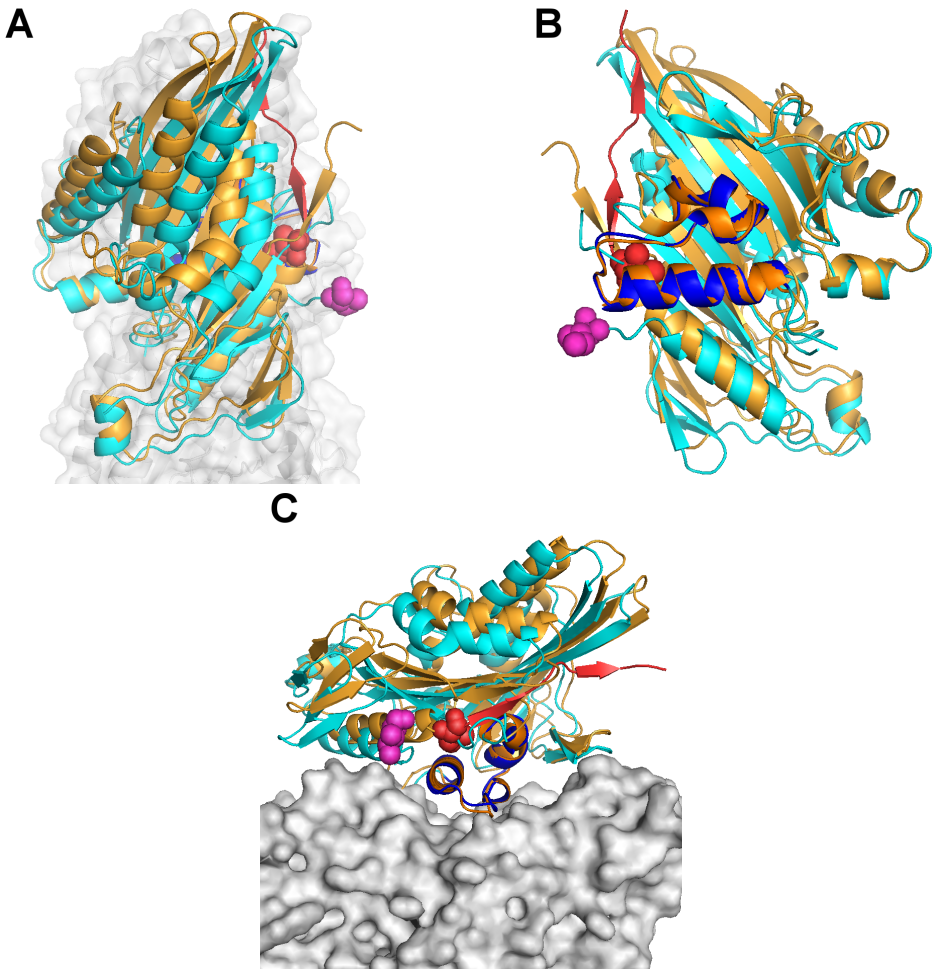

Figure 3.7 Model of conformational switching

Model of conformational switching of kinesin-1 based on X-ray crystallographic information. For this model, the main microtubule-binding interface of human kinesin in the ATP-like (PDB ID: 1MKJ [270]; orange) and ADP/apo-state (PDB ID: 2P4N [271]; cyan) was superimposed under the assumption that these regions are in contact with the microtubule in identical fashion. (A) view from the outside of the microtubule, approximately perpendicular to the protofilament axis; plus-end is facing up. (B) view looking at microtubule-binding interface of kinesin, approximately radially from the protofilament axis; plus-end is facing up. (C) side view with plus-end facing right. The switch II region used for superposition (residues 256-290) is colored in a darker shade of the original color. The docked neck linker in 1BG2 [184] is colored red, and residue I325 at the start of the neck linker of each molecule are shown as spacefilling spheres. Tubulin coordinates (grey surface) are part of the apo-structure of human kinesin, which was solved in complex with microtubule by cryo-electron microscopy. The original study derived the coordinates for the apo state from independent docking of PDB ID's 1JFF (tubulin [191]) and 1BG2 (human kinesin, ADP-state [184]) to the EM-derived density map and subsequent merging of the results [271].

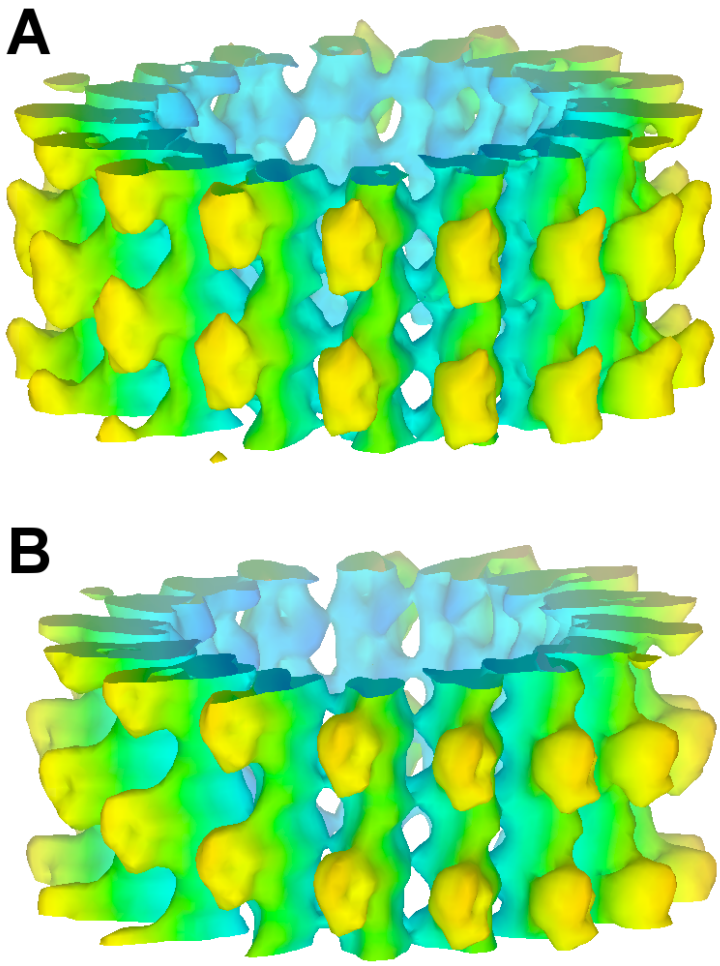

FIGURE 3.8 RECONSTRUCTIONS OF DIMER KINESINS

Structures of dimeric kinesins in the presence of AMPPNP: wild-type dimer kinesin (dKH405wt) (A) and non-processive mutant with 12 residue neck linker insertion (dKH405-I12) (B). Reconstructions were obtained by helical analysis, filtered to 18 Å, normalized and adjusted to show similar isosurfaces. Color varies by radius from inside (blue) to outside (orange).

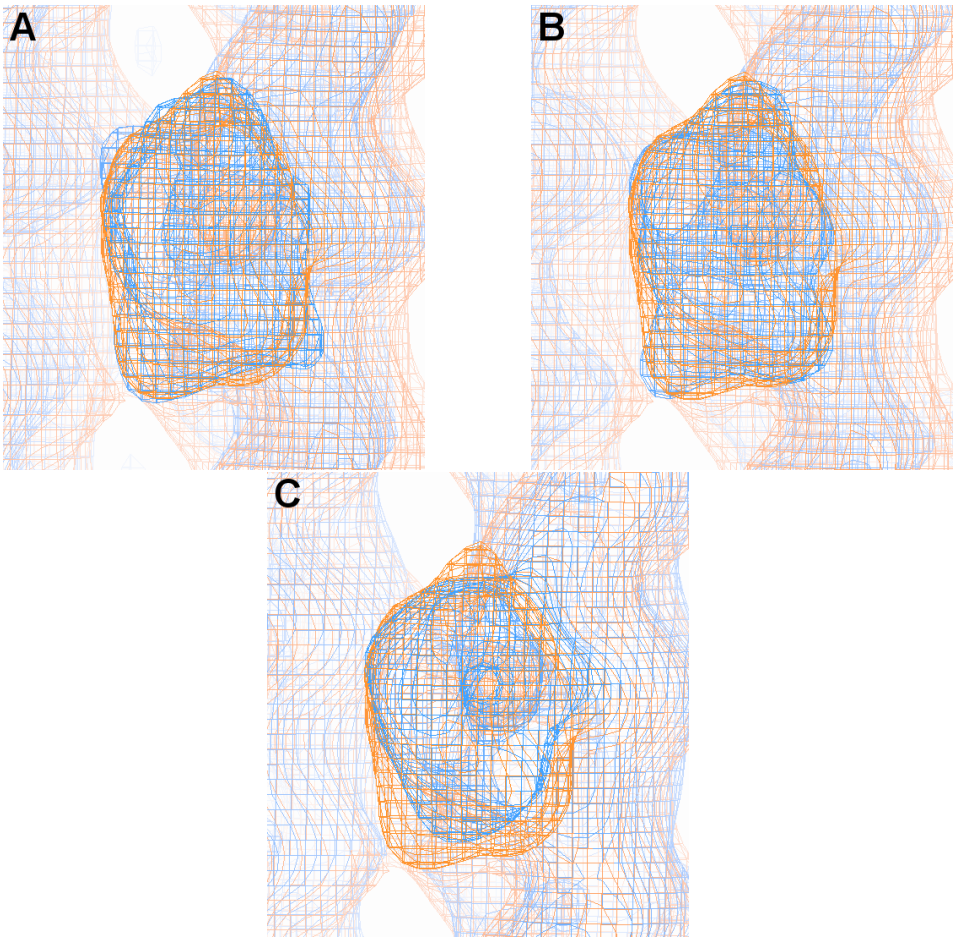

FIGURE 3.9 COMPARISON OF KINESIN STRUCTURES

Comparison of kinesin reconstructions. Kinesin density maps were scaled to the same magnification and aligned in Fourier space. All views are approximately perpendicular to the microtubule axis with the plus-end facing up. Orange density map represents wild-type construct in all panels. (A) Comparison of monomer kinesin in AMPPNP state (blue) with wild-type dimer kinesin (orange) (B) Comparison of monomer kinesin in apo state (blue) with wild-type dimer kinesin (orange) (C) Comparison of wild-type dimer kinesin (orange) with non-processive mutant kinesin (blue)

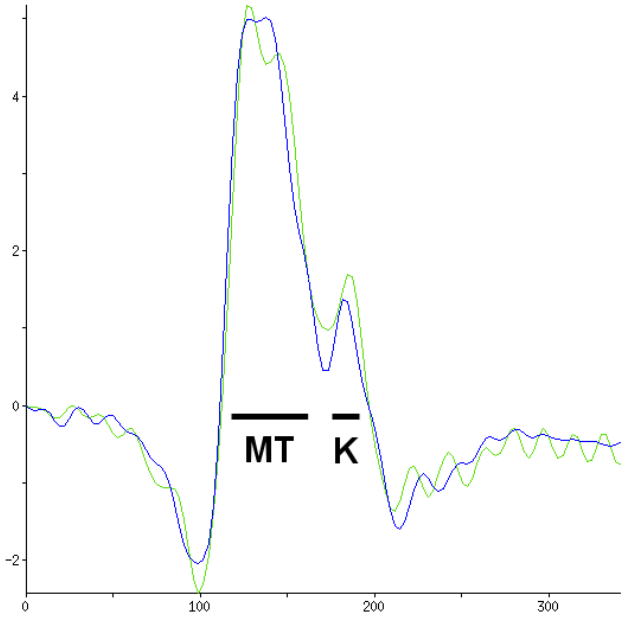

FIGURE 3.10 RADIAL DENSITY PROFILE FOR DIMERS

Graph showing the radial density profiles for dimeric kinesins. Wild-type is (green), mutant (blue). The Y-axis is labeled with arbitrary density values, the X-axis in Å from the microtubule center at 0. Density peaks are labeled **MT** (microtubule) and **K** (kinesin). Due to artifacts related to the contrast transfer function (CTF) (e.g. negative density peaks), the graphs should not be taken as absolute measures of density.

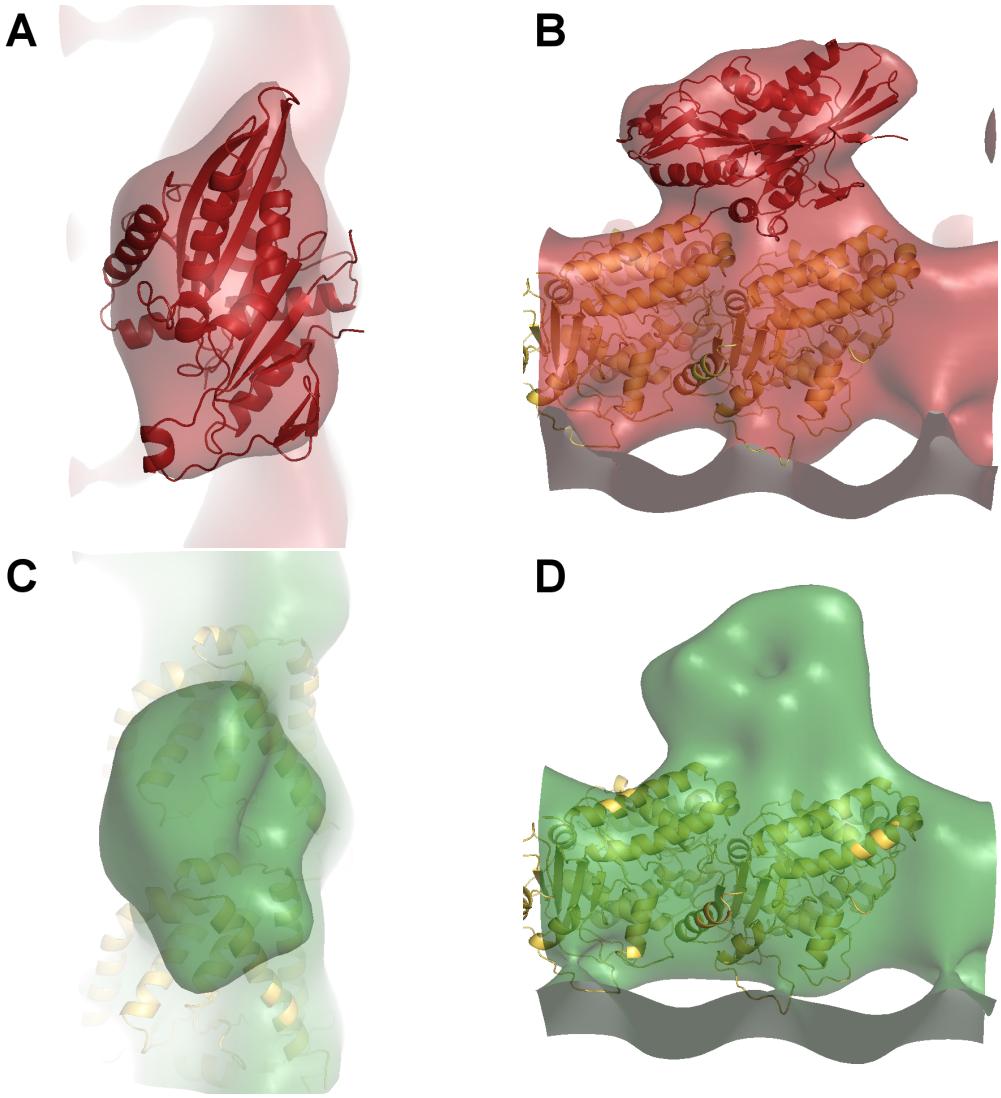

FIGURE 3.11 DOCKING OF DIMER KINESIN

(A,B) Atomic coordinates of a representative kinesin were docked to the density maps of the wild-type dimer kinesin construct dKH405wt. The atomic coordinates are those of human kinesin (PDB ID: 1MKJ [270]) in the ATP-like state with neck linker docked. Density map was filtered to 18 Å resolution, and atomic coordinates were modified to facilitate docking as for the monomers. The side view includes the independently docked coordinates of tubulin (gold; PDB ID: 1JFF [191])
(C,D) Due to the unusual appearance of the mutant dimer kinesin-microtubule complex, only tubulin coordinates (gold; PDB ID: 1JFF [191]) could be docked to the density map and no "reasonable solutions" were found for kinesin.

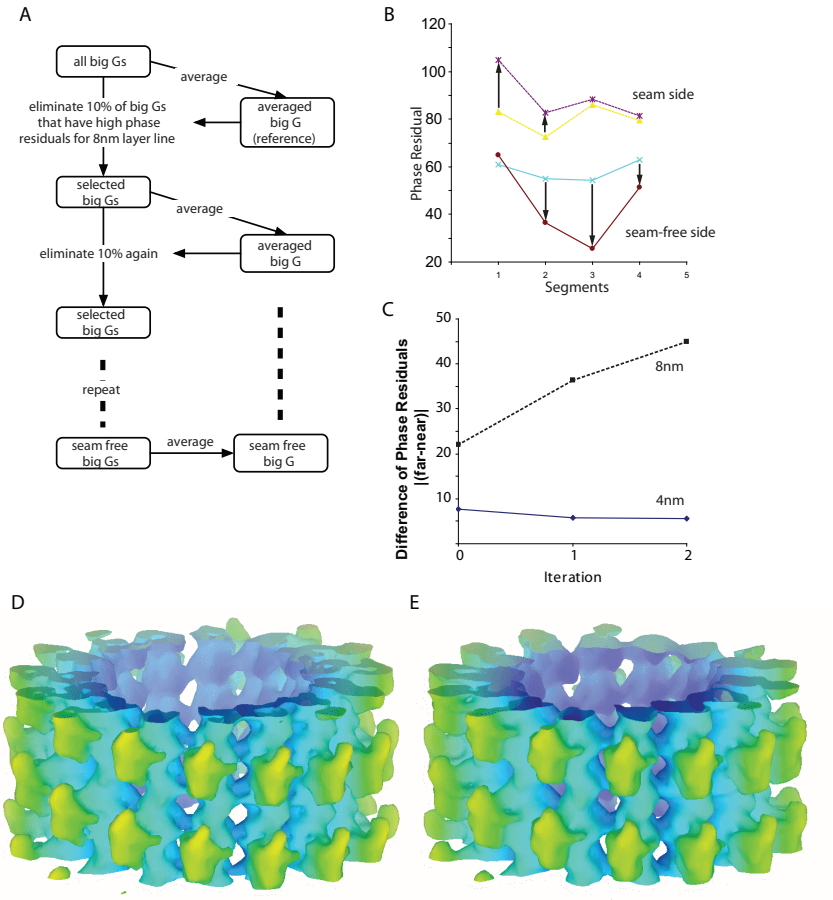

FIGURE 3.12 ASYMMETRIC HELICAL RECONSTRUCTION

Application of asymmetric helical reconstruction to experimental images. (A) Flowchart for distinguishing the seam side and seam-free side within a data set. (B) Phase residuals for 8nm layer line (Bessel order -1.5) for far and near sides of a microtubule with a seam (14 protofilaments, 3-start helix) after alignment to a reference containing equal numbers of seam sides and seam-free sides (yellow and blue plots), and after 2 iterations of refinement (purple and brown plots). (C) Average far-near difference in phase residual for a layer line of integer (4nm, solid line) and non-integer Bessel order (8nm, dashed line) over 2 iterations of refinement. (D,E) Reconstructions of the KIF1A-microtubule complex, shown at 17 Å resolution, using (D) conventional helical reconstruction from seam-free 15-protofilament microtubules, and (E) asymmetric helical reconstruction from 14-protofilament microtubules containing a seam.

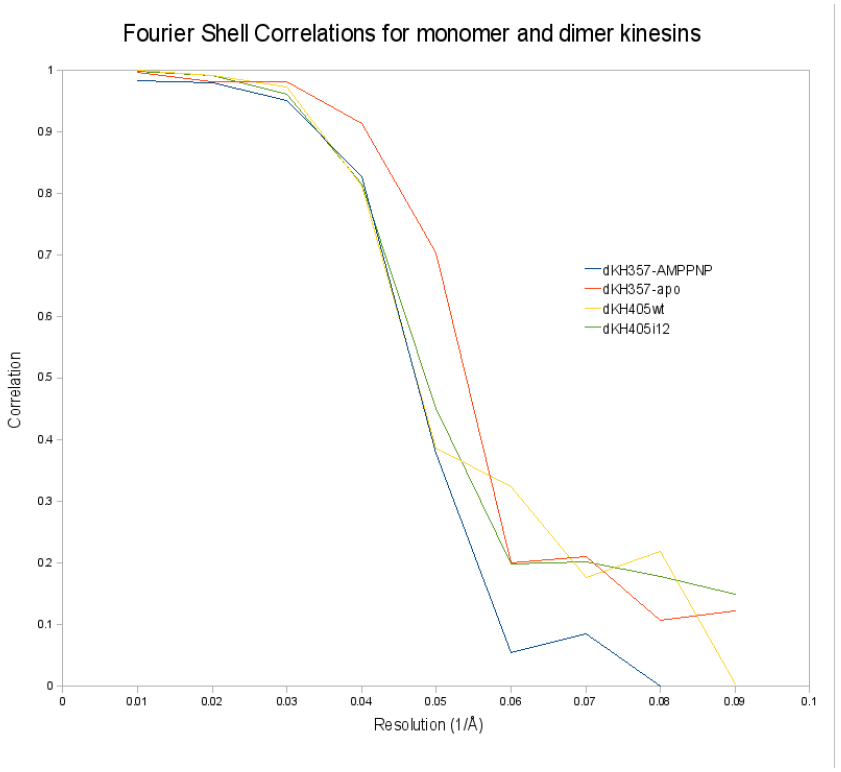

FIGURE 3.13 FOURIER SHELL CORRELATIONS (FSC)

Fourier Shell Correlation curves for monomeric (dKH357) and dimeric kinesins (dKH405).

Tables

Table 3.1 Cross-Correlations for Docking.

	Atomic Coordinates (PDB ID)		
	1MKJ ("ATP")	**1BG2 ("apo")**	**1JFF (tub)**
Map	**absolute values**		
dKH357-AMPPNP	0.138496	0.143531	0.188587
dKH357-apo	0.169948	0.183907	0.201003
dKH405wt	0.157786	0.163863	0.242467
dKH405-I12	N/A	N/A	0.243748
Map	**normalized values**		
dKH357-AMPPNP	0.734	0.761	1
dKH357-apo	0.845	0.915	1
dKH405wt	0.651	0.676	1
dKH405-I12	N/A	N/A	1

CHAPTER FOUR
Discussion

The kinesin-1 nucleotide switch

In order to establish the basis for nucleotide-dependent switching in kinesin-1, we have solved the structures of a monomeric construct of kinesin-1 in the ATP-like and apo states. These two states are expected to be crucial to the mechanism of processivity, and likely constitute the states in the transitional two head-bound state during kinesin walking. Our reconstruction of the apo state generally agrees with published data [271], while the structure of the microtubule-bound monomer in the ATP-like state is novel. Our results suggest that the nucleotide-dependent conformational change of the kinesin-1 core occurs as a clockwise "tilt" between the ATP-like conformation that is more closely aligned with the microtubule protofiment axis, and the apo state. This tilt appears to be analogous to the conformational change observed in KIF1A, but the angle of the tilt is much smaller, from 12° in KIF1A [168] to at most a few degrees based on our reconstructions. This finding argues for a common mechanism of nucleotide-dependent switching, but the differences between kinesin-1 and KIF1A may be indicative of different mechanistic implementations of switching during motility.

Comparison with the processive KIF1A monomer

It has been found that the monomeric KIF1A moves processively along the microtubule using a biased diffusional mechanism [226]. To prevent detachment during motility, KIF1A alternately uses two loops to stay attached to microtubule, even in the weak binding state, and is therefore "anchored" to the microtubule even when the catalytic head is largely released [227]. Furthermore, KIF1A has been proposed to interact during motility with the C-terminal tails of tubulin, the last approximately 10-18 residues of tubulin that are highly disordered [191, 259], and to use this interaction to "float" from one tubulin to the next [227] while being "anchored" to the microtubule even in the weak binding state. Based this and other data, KIF1A can been thought of as "gliding" along the microtubule surface, using its unique K-loop like an oar to interact with successive tubulin subunits, much like a rowboat gliding along a lake [168]. Because KIF1A cannot count on gravity to keep it attached to the microtubule, however, the rowing has to be interrupted by states of strong attachment to prevent detachment from the microtubule. In this mode of movement, the large conformational changes associated with nucleotide-dependent switching may be beneficial in several ways. First, the counter-clockwise tilt is accompanied by a plus-end directed movement of the motor core upon ATP-binding can act to position the K-loop closer to the next binding site. Second, the "reset" of the ATP-like conformation during the weakly attached moves the microtubule-binding site of KIF1A closer to the next tubulin [168]. Together, these mechanistic details provide KIF1A with the ability to move processively by a biased Brownian-motion mechanism, despite effectively having only "one leg to stand on".

In contrast to KIF1A, kinesin-1 moves processively by coordinating the nucleotide cycles of two heads [13, 86, 95, 97, 197]. Increasing evidenc suggests

that the coordination of the heads in kinesin-1 is based at least in part on strain [41, 49, 93, 107, 141, 208, 250, 273, 342]. In particular, Hackney found that relieving strain acting on the heads through insertion of additional residues in the neck linker severely disrupts kinetic processivity in kinesin-1. A simple and attractive mechanism has been proposed to account for strain in the coordination of kinesin-1 [163, 256] and can be easily visualized using KIF1A as an example. Based on this model, the nucleotide cycles of two kinesin heads can be coordinated by linking them with a flexible tether in length just short of the distance between two consecutive microtubule binding sites. Forward stepping could then be coordinated as follows. In the absence of nucleotide, the tether is not long enough to allow a dimer to span two consecutive binding sites. However, stepping could occur when the trailing head binds ATP. The ensuing counter-clockwise tilt would then allow the tethered head to reach forward and attach to the next binding site. This mechanism can therefore couple attachment of one head to the nucleotide-dependent conformational change of the other.

The role of tilting in kinesin-1 processivity

The small angle of nucleotide-dependent tilt apparent in our results might seems at first difficult to reconcile with such a model, because the small angle of the tilt seen in our reconstructions may be on the order of only a few Å. Nonetheless, the model is consistent with our data for the following reasons. First, the 13 amino acids of the neck linker on each head in a two-head bound state can extend to approximately 81 Å, when each amino acid is extended to 3.1 Å. This extension therefore already places considerable strain on the linkage, estimated to approximately 17 pN*nm [141]. The straightening of the core, even if it moves the base of the neck linker toward the plus-end by only 5 Å, would involve a large unfavorable entropy change incurred by restricting the conformational freedom of the of the neck linker residues. The strain on the linkage would then increase by an additional 6-8

pN*nm (1.5 - 2 kT) [163]. Furthermore, even if the movement of the neck linker base is less than 5 Å, considerable bias against straightening of the core is imposed by the clashing of extended neck linker residues against other structural features of the kinesin core, notably a β-domain towards the rear of the kinesin molecule. It is therefore possible that strain on the neck linker prevents nucleotide-dependent straightening of the lead head, thereby playing an important role in processivity [163].

Advances in single-molecule fluorescence tracking have allowed the study of single kinesin dimers during motility, and have yielded considerable insight into the mechanism of kinesin [34, 78, 82, 93, 145, 158, 214, 252, 278, 296, 299, 327] and other molecular motors [235, 242, 298, 340]. A recent study directly addressed the question of whether the decrease in *kinetic processivity* (the ability to complete several nucleotide cycles in a single diffusional encounter with a microtubule [98]) observed in mutants with longer neck linkers [107] leads to a decrease in mechanical processivity (the ability to take many steps before falling off the track [156]). These investigators found that the insertion of additional residues in the neck linker does not necessarily lead to a corresponding decrease in *mechanical processivity* [342]. Instead, progressively longer and more flexible linkers lead to a decrease in *coupling* of ATP hydrolysis to stepping, thereby greatly increasing the number of futile hydrolysis events and decreasing the motor velocity [342]. An applied backward load is likely to increase the resistance to detachment of the motor [17], because backward loads prevent nucleotide binding [324]. A load in the forward direction (towards the microtubule plus-end), on the other hand, restored velocity [342], suggesting that strain may be as important to *coupling* as it is to processivity. The finding that there is no straightforward relationship between *kinetic processivity* and *mechanical processivity* is somewhat surprising. However, it is noteworthy that individual heads under zero-load condition can hydrolyze several ATP before release from the microtubule [148, 198], and it is possible that the uncoordinated attachment/release of

two heads keeps the dimeric motor attached to the microtubule under low ATP concentrations. Furthermore, a model in which coordination is achieved solely through the gating of nucleotide binding to the front head by the effects of strain implies that the insertion of even a single residue in the neck linker would render kinesin-1 largely non-processive in the mechanical sense, a notion clearly contradicted by existing data [107, 342].

It is therefore likely that other mechanisms contribute to *mechanical processivity* of kinesin. Several studies have addressed this problem. Visscher et al. reported that two load-dependent processes are likely to be involved in kinesin-1 motility [324]. Furthermore, strain on the trailing head has been implicated in "trapping" ADP after hydrolysis [52, 307], thereby preventing reversion of the head to the strongly bound apo state in the trailing position. Yet other experiments have suggested that forwards-directed tension accelerates trailing head release [49, 335], and that an externally imposed forward pull on the motor can restore processive motility to motors otherwise unable to move efficiently either by extended neck linkers [342], or by mutation of the neck linker attachment site on the motor core [161]. These observations are also consistent with a proposed mechanism by which ADP release is a force-producing event [116] and allows dimers to take one step per ATP hydrolyzed [46, 47, 71, 265, 289, 324], as compared to single heads that hydrolyze on average four ATP before release [148, 198]. These data emphasize the effects of strain on the release of trailing head, rather than on the gating of the leading head. Nonetheless, they are consistent with our hypothesis that nucleotide-dependent tilting of the core contributes to kinesin processivity.

Other mechanisms affecting processivity

While strain plays an important role in kinesin-1 processivity, it is possible that other structural features contribute to the maintenance coordination between kinesin-1 heads. Recent studies have found that the the β-domain at the front of the

motor core to which the neck linker docks, termed "neck-cover bundle", is actively involved in force production [161] during neck linker docking, as well as "latching" of the neck linker against undocking [140]. It has also been previously reported that feedback on neck linker docking is transmitted from the "neck-cover bundle" to the catalytic site [108]. A recent study proposed that the "neck-cover bundle" dynamically folds forward to generate force [161]. Furthermore, these authors find that the motility of "cover-strand" mutants lacking part of the docking interface of the neck linker can be restored using an assiting load. An external assisting load applied to the neck linker is expected to rotate the kinesin core counter-clockwise, and is therefore consistent with a model in which nucleotide-dependent tilting of the kinesin core traps ATP and accelerates hydrolysis. The involvement of the "neck-cover bundle" in kinesin motility is a newly emerging theme that carries promise in further elucidating the mechanism of kinesin processivity, and it will be interesting to study the transitions in the "neck-cover bundle" using high-resolution structural methods.

Despite the promise of elucidating the mechanism of processivity by comparing processive wild-type dimers with non-processive mutant dimers, our results cannot be taken as evidence for the disruption of processivity in the I12 mutant by the relieving of strain between the heads. Our main finding with respect to the mutant dimer is that it does not fully occupy the microtubule lattice. One possible reason is that the longer neck linkers and/or neck domains emanating from bound heads have considerable freedom to occlude binding sites near the head. Another possibility is that the neck linker is involved in binding, and that the additional residues disrupt the attachment of kinesin dimers to the microtubule. From our work, neither possibility can be ruled out, and it is difficult to infer any information about the nature of processivity from this result. Nonetheless, our result from the wild-type dimer shows that it is in principle possible to decorate microtubule with dimeric kinesins in the two-head bound state, and that helical analysis could be

used to show differences between processive and non-processive dimers.

Lastly, Ruby-Helix was developed to facilitate the analysis of conventional helical objects and, for the first time, incorporate a new method, asymmetric helical reconstruction [162]. The main difference between conventional and asymmetric helical reconstruction is selection of the seam-free side among layer lines with non-integer Bessel orders. Otherwise, distortions of the helical structure with seams are corrected as described for conventional helical analysis, using layer lines of integer Bessel order. Asymmetric helical reconstruction allows the analysis of structures such as the dahlemense strain of tobacco mosaic virus [37], certain bacterial flagella [305], and the majority of in vitro polymerized microtubules [165, 277] possess discontinuities within the helical lattice. These "perturbations" or "seams" prevent application of conventional helical theory to those filaments, but can be analyzed using asymmetric helical analysis. In the case of microtubules and complexes of microtubules and microtubule-binding proteins, the new method allows a significant increase in the overall throughput for structure determination. For example, most studies on kinesin-microtubule complexes have used helical microtubules, which represent approximately 10% of the total for *in vitro*-polymerized microtubules [241]. Applying asymmetric helical reconstruction to kinesin-microtubule complexes allows a significant fraction of the non-helical microtubules to be analyzed, thereby considerably reducing the overall time for structure solving.

Summary/Synopsis

By comparing monomers in different nucleotide states with processive and non-processive dimers of kinesin-1 in our structural studies, we expected to observe nucleotide-dependent differences between monomers and strain-dependent differences between processive and non-processive dimers. We hypothesized that a tilting similar to that observed in the monomeric KIF1A may contribute to processivity in the dimeric motor, as other studies have found a dependence of processivity on the length of the neck linkers connecting the heads. Increasing the length of the neck linker was found to abolish processivity [107], and we argued that in the presence of ATP analogs the fully extended neck linkers would allow the leading head to bind the microtubule in the forward position only in a tilted conformation unable to hydrolyse ATP, as suggested by others [256]. We have likely identified a nucleotide-depended tilt of the kinesin-1 core analogous to that reported for KIF1A [168], but of smaller magnitude. This tilt can be considered consistent with the model of processivity, but we were unable to verify experimentally whether strain on the neck linker indeed constrains the conformation of the two-head bound state.

Perspectives

Since its discovery in 1985, kinesin has been the subject of intensive research, making kinesin proteins perhaps the most-studied protein motor family to date. The enzymatic and biochemical properties of kinesins are well-established, and a large number of atomic models are available, showing kinesin in different nucleotide and structural states. Nonetheless, the structural basis for kinesin processivity remains elusive. An emerging theme in the literature places increasing importance of strain on the heads as a mechanism of coordination (reviewed in [41]). Strain is likely to be transmitted through the neck linker connecting the heads, and the neck linker has indeed been found to have spring-like properties consistent with a role in force transduction [342].

The notion that strain affects the stepping of kinesin presents a change in thinking in the field about the relationship between nucleotide and conformation. Previous studies have focused on the interactions of the nucleotide with the kinesin as the driving force behind conformational changes that lead to motility. The finding that strain can coordinate the kinesin heads implies that such strain can restrict nucleotide-induced conformational switching. This, in turn, suggests that motility in kinesin may be maintained through a feedback loop between the nucleotide and structural elements, such as the neck linker.

Despite good evidence that strain is important for processivity, it remains unclear how such strain would affect the conformations of the heads experiencing the strain. A model based on nucleotide-dependent core rotation of KIF1A could not be fully verified with kinesin-1 (our results). Nonetheless, our results are a starting point for further studies on the structural basis of kinesin processivity. To date, our structures are the first to report on nucleotide-induced switching of kinesin-1 in the functional context of the microtubule. Further studies will be needed to conclusively identify the mechanism by which the nucleotide-induced conformational switch observed in our results is involved in kinesin-1 processivity.

Future

To further verify the nucleotide-induced differences observed in our monomeric constructs of conventional kinesin, it will be necessary to improve the resolution of our reconstructions. Careful consideration will also be given to the interpretation of reconstructions from processive and non-processive dimeric kinesins. Furthermore, in light of other findings regarding structure-function relationships in kinesin [164], it may be necessary to look beyond crystal structures to formulate a working model of kinesin processivity. It is possible that approaches have to be considered that do not depend on static snapshots of the conformation of kinesin, but rather are able to resolve the conformational changes occuring during kinesin motility. Given more recent evidence, it may also be necessary to consider not only kinesin as a motile element, but also whether the microtubule could be involved in kinesin motility (reviewed in [163]).

BIBLIOGRAPHY

[1] Adrian, M., Dubochet, J., Fuller, S. D., and Harris, J. R. (1998). Cryo-negative staining. Micron, 29(2-3):145–60.

[2] Adrian, M., Dubochet, J., Lepault, J., and McDowall, A. W. (1984). Cryo-electron microscopy of viruses. Nature, 308(5954):32–6.

[3] Aizawa, H., Sekine, Y., Takemura, R., Zhang, Z., Nangaku, M., and Hirokawa, N. (1992). Kinesin family in murine central nervous system. J Cell Biol, 119(5):1287–96.

[4] Al-Amoudi, A., Chang, J. J., Leforestier, A., McDowall, A., Salamin, L. M., Norlen, L. P., Richter, K., Blanc, N. S., Studer, D., and Dubochet, J. (2004). Cryo-electron microscopy of vitreous sections. EMBO J, 23(18):3583–8.

[5] Allen, R. D., Metuzals, J., Tasaki, I., Brady, S. T., and Gilbert, S. P. (1982). Fast axonal transport in squid giant axon. Science, 218(4577):1127–9.

[6] Alonso, M. C., Drummond, D. R., Kain, S., Hoeng, J., Amos, L., and Cross, R. A. (2007). An ATP gate controls tubulin binding by the tethered head of kinesin-1. Science, 316(5821):120–3.

[7] Alwyn Jones, T. and Kleywegt, G. J. (1999). CASP3 comparative modeling evaluation. Proteins, Suppl 3:30–46.

[8] Aoyama, K., Ogawa, K., Kimura, Y., and Fujiyoshi, Y. (1995). A method for 2D crystallization of soluble proteins at liquid-liquid interface. Ultramicroscopy, 57(4):345–54.

[9] Arnal, I., Metoz, F., DeBonis, S., and Wade, R. H. (1996). Three-dimensional structure of functional motor proteins on microtubules. Curr Biol, 6(10):1265–70.

[10] Asbury, C. L. (2005). Kinesin: world's tiniest biped. Curr Opin Cell Biol, 17(1):89–97.

[11] Asbury, C. L., Fehr, A. N., and Block, S. M. (2003). Kinesin moves by an asymmetric hand-over-hand mechanism. Science, 302(5653):2130–4.

[12] Asenjo, A. B., Weinberg, Y., and Sosa, H. (2006). Nucleotide binding and hydrolysis induces a disorder-order transition in the kinesin neck-linker region. Nat Struct Mol Biol, 13(7):648–54.

[13] Auerbach, S. D. and Johnson, K. A. (2005). Alternating site ATPase pathway of rat conventional kinesin. J Biol Chem, 280(44):37048–60.

[14] Berliner, E., Young, E. C., Anderson, K., Mahtani, H. K., and Gelles, J. (1995). Failure of a single-headed kinesin to track parallel to microtubule protofilaments. Nature, 373(6516):718–21.

[15] Beroukhim, R. and Unwin, N. (1997). Distortion correction of tubular crystals: improvements in the acetylcholine receptor structure. Ultramicroscopy, 70(1-2):57–81.

[16] Block, S. M. (1995). Nanometres and piconewtons: the macromolecular mechanics of kinesin. Trends Cell Biol, 5(4):169–75.

[17] Block, S. M., Asbury, C. L., Shaevitz, J. W., and Lang, M. J. (2003). Probing the kinesin reaction cycle with a 2D optical force clamp. Proc Natl Acad Sci U S A, 100(5):2351–6.

[18] Block, S. M., Goldstein, L. S., and Schnapp, B. J. (1990). Bead movement by single kinesin molecules studied with optical tweezers. Nature, 348(6299):348–52.

[19] Blom, D. A., Allard, L. F., O'Keefe, M. A., and Mishina, S. (2005). High Resolution Imaging with an Aberration Corrected JEOL 2200FS-AC STEM/TEM. Microsc Microanal, 11:Suppl 2.

[20] Boisset, N., Radermacher, M., Grassucci, R., Taveau, J. C., Liu, W., Lamy, J., Frank, J., and Lamy, J. N. (1993). Three-dimensional immunoelectron microscopy of scorpion hemocyanin labeled with a monoclonal Fab fragment. J Struct Biol, 111(3):234–44.

[21] Boisset, N., Taveau, J. C., Lamy, J., Wagenknecht, T., Radermacher, M., and Frank, J. (1990). Three-dimensional reconstruction of native Androctonus australis hemocyanin. J Mol Biol, 216(3):743–60.

[22] Brady, S. T. (1985). A novel brain ATPase with properties expected for the fast axonal transport motor. Nature, 317(6032):73–5.

[23] Brady, S. T., Lasek, R. J., and Allen, R. D. (1982). Fast axonal transport in extruded axoplasm from squid giant axon. Science, 218(4577):1129–31.

[24] Braet, F., Wisse, E., Bomans, P., Frederik, P., Geerts, W., Koster, A., Soon, L., and Ringer, S. (2007). Contribution of high-resolution correlative imaging techniques in the study of the liver sieve in three-dimensions. Microsc Res Tech, 70(3):230–42.

[25] Bremer, A., Henn, C., Engel, A., Baumeister, W., and Aebi, U. (1992). Has negative staining still a place in biomacromolecular electron microscopy? Ultramicroscopy, 46(1-4):85–111.

[26] Brenner, S. and Horne, R. W. (1959). A negative staining method for high resolution electron microscopy of viruses. Biochim Biophys Acta, 34:103–10.

[27] Brownbridge, G. G., Lowe, P. N., Moore, K. J., Skinner, R. H., and Webb, M. R. (1993). Interaction of GTPase activating proteins (GAPs) with p21ras measured by a novel fluorescence anisotropy method. Essential role of Arg-903 of GAP in activation of GTP hydrolysis on p21ras. J Biol Chem, 268(15):10914–9.

[28] Brunger, A. T., Adams, P. D., Clore, G. M., DeLano, W. L., Gros, P., Grosse-Kunstleve, R. W., Jiang, J. S., Kuszewski, J., Nilges, M., Pannu, N. S., Read, R. J., Rice, L. M., Simonson, T., and Warren, G. L. (1998). Crystallography & NMR system: A new software suite for macromolecular structure determination. Acta Crystallogr D Biol Crystallogr, 54(Pt 5):905–21.

[29] Buseck, P. R., Cowley, J. M., and Eyring, L. (1988). High-Resolution Transmission Electron Microscopy. Oxford University Press.

[30] Butterworth, 4th, J. F. and Strichartz, G. R. (1990). Molecular mechanisms of local anesthesia: a review. Anesthesiology, 72(4):711–34.

[31] Carragher, B., Kisseberth, N., Kriegman, D., Milligan, R. A., Potter, C. S., Pulokas, J., and Reilein, A. (2000). Leginon: an automated system for acquisition of images from vitreous ice specimens. J Struct Biol, 132(1):33–45.

[32] Carragher, B., Whittaker, M., and Milligan, R. A. (1996). Helical processing using PHOELIX. J Struct Biol, 116(1):107–12.

[33] Carter, N. J. and Cross, R. A. (2005). Mechanics of the kinesin step. Nature, 435(7040):308–12.

[34] Carter, N. J. and Cross, R. A. (2006). Kinesin's moonwalk. Curr Opin Cell Biol, 18(1):61–7.

[35] Case, R. B., Pierce, D. W., Hom-Booher, N., Hart, C. L., and Vale, R. D. (1997). The directional preference of kinesin motors is specified by an element outside of the motor catalytic domain. Cell, 90(5):959–66.

[36] Case, R. B., Rice, S., Hart, C. L., Ly, B., and Vale, R. D. (2000). Role of the kinesin neck linker and catalytic core in microtubule-based motility. Curr Biol, 10(3):157–60.

[37] Caspar, D. L. and Holmes, K. C. (1969). Structure of dahlemense strain of tobacco mosaic virus: a periodically deformed helix. J Mol Biol, 46(1):99–133.

[38] Chang, W. H. and Kornberg, R. D. (2000). Electron crystal structure of the transcription factor and DNA repair complex, core TFIIH. Cell, 102(5):609–13.

[39] Chester, D. W., Klemic, J. F., Stern, E., Sigworth, F. J., and Klemic, K. G. (2007). Holey carbon micro-arrays for transmission electron microscopy: a microcontact printing approach. Ultramicroscopy, 107(8):685–91.

[40] Chiu, W., Downing, K. H., Dubochet, J., Glaeser, R. M., Heide, H. G., Knapek, E., Kopf, D. A., Lamvik, M. K., Lepault, J., Robertson, J. D., Zeitler, E., and Zemlin, F. (1986). Cryoprotection in electron microscopy. J Microsc, 141:385–391.

[41] Cochran, J. C. and Kull, F. J. (2008). Kinesin motors: no strain, no gain. Cell, 134(6):918–9.

[42] Cooley, J. W. and Tukey, J. W. (1965). An algorithm for the machine calculation of complex Fourier series. Math Comput, 19:297–301.

[43] Cordova, N. J., Ermentrout, B., and Oster, G. F. (1992). Dynamics of single-motor molecules: the thermal ratchet model. Proc Natl Acad Sci U S A, 89(1):339–43.

[44] Correia, J. J., Gilbert, S. P., Moyer, M. L., and Johnson, K. A. (1995). Sedimentation studies on the kinesin motor domain constructs K401, K366, and K341. Biochemistry, 34(14):4898–907.

[45] Coy, D. L., Hancock, W. O., Wagenbach, M., and Howard, J. (1999a). Kinesin's tail domain is an inhibitory regulator of the motor domain. Nat Cell Biol, 1(5):288–92.

[46] Coy, D. L., Wagenbach, M., and Howard, J. (1999b). Kinesin takes one 8-nm step for each ATP that it hydrolyzes. J Biol Chem, 274(6):3667–71.

[47] Crevel, I., Carter, N., Schliwa, M., and Cross, R. (1999). Coupled chemical and mechanical reaction steps in a processive Neurospora kinesin. EMBO J, 18(21):5863–72.

[48] Crevel, I. M., Lockhart, A., and Cross, R. A. (1996). Weak and strong states of kinesin and ncd. J Mol Biol, 257(1):66–76.

[49] Crevel, I. M., Nyitrai, M., Alonso, M. C., Weiss, S., Geeves, M. A., and Cross, R. A. (2004). What kinesin does at roadblocks: the coordination mechanism for molecular walking. EMBO J, 23(1):23–32.

[50] Crewe, A. V. (1966). Scanning Electron Microscopes: Is High Resolution Possible? Science, 154(3750):729–738.

[51] Cross, R. A. (2001). Molecular motors: Kinesin's string variable. Curr Biol, 11(4):R147–9.

[52] Cross, R. A., Crevel, I., Carter, N. J., Alonso, M. C., Hirose, K., and Amos, L. A. (2000). The conformational cycle of kinesin. Philos Trans R Soc Lond B Biol Sci, 355(1396):459–64.

[53] Crowther, R. A. (1976). The interpretation of images reconstructed from electron micrographs of biological particles. In Markham, R. and Horne, R. W., editors, Proceedings of the Third John Innes Symposium, pages 15–25. North-Holland, Amsterdam.

[54] Crowther, R. A., Henderson, R., and Smith, J. M. (1996). MRC image processing programs. J Struct Biol, 116(1):9–16.

[55] Cyrklaff, M., Adrian, M., and Dubochet, J. (1990). Evaporation during preparation of unsupported thin vitrified aqueous layers for cryo-electron microscopy. J Electron Microsc Tech, 16(4):351–5.

[56] De Carlo, S. (2002). Cryo-negative staining: advantages and applications for three-dimensional electron microscopy of biological macromolecules. PhD thesis, Universite de Lausanne.

[57] De Carlo, S., Boisset, N., and Hoenger, A. (2008). High-resolution single-particle 3D analysis on GroEL prepared by cryo-negative staining. Micron, 39(7):934–43.

[58] De Carlo, S., El-Bez, C., Alvarez-Rua, C., Borge, J., and Dubochet, J. (2002). Cryo-negative staining reduces electron-beam sensitivity of vitrified biological particles. J Struct Biol, 138(3):216–26.

[59] DeRosier, D. and Klug, A. (1968). Reconstruction of three dimensional structures from electron micrographs. Nature, 217:130.

[60] DeRosier, D. J. and Moore, P. B. (1970). Reconstruction of three-dimensional images from electron micrographs of structures with helical symmetry. J Mol Biol, 52(2):355–69.

[61] Desai, A., Verma, S., Mitchison, T. J., and Walczak, C. E. (1999). Kin I kinesins are microtubule-destabilizing enzymes. Cell, 96(1):69–78.

[62] Dubochet, J., Adrian, M., Chang, J. J., Homo, J. C., Lepault, J., McDowall, A. W., and Schultz, P. (1988). Cryo-electron microscopy of vitrified specimens. Q Rev Biophys, 21(2):129–228.

[63] Dubochet, J., Richter, K., Roy, H. V., and McDowall, A. W. (1991). Freezing: facts and hypothesis. Scanning Microsc Suppl, 5(4):S11–5; discussion S15–6.

[64] Egelman, E. H. (1986). An algorithm for straightening images of curved filamentous structures. Ultramicroscopy, 19(4):367–73.

[65] Egelman, E. H. (2007). The iterative helical real space reconstruction method: surmounting the problems posed by real polymers. J Struct Biol, 157(1):83–94.

[66] Endow, S. A. and Waligora, K. W. (1998). Determinants of kinesin motor polarity. Science, 281(5380):1200–2.

[67] Endres, N. F., Yoshioka, C., Milligan, R. A., and Vale, R. D. (2006). A lever-arm rotation drives motility of the minus-end-directed kinesin Ncd. Nature, 439(7078):875–8.

[68] Enemark, E. J. and Joshua-Tor, L. (2008). On helicases and other motor proteins. Curr Opin Struct Biol, 18(2):243–57.

[69] Enos, A. P. and Morris, N. R. (1990). Mutation of a gene that encodes a kinesin-like protein blocks nuclear division in A. nidulans. Cell, 60(6):1019–27.

[70] Ermantraut, E., Wohlfart, K., and Tichelaar, W. (1998). Perforated support foils with pre-defined hole size, shape and arrangement. Ultramicroscopy, 74(1-2):75 – 81.

[71] Fehr, A. N., Asbury, C. L., and Block, S. M. (2008). Kinesin steps do not alternate in size. Biophys J, 94(3):L20–2.

[72] Feynman, R. P. (1963). Lectures in Physics, volume I. Addison-Wesley Publishing Co.

[73] Fisher, M. E. and Kim, Y. C. (2005). Kinesin crouches to sprint but resists pushing. Proc Natl Acad Sci U S A, 102(45):16209–14.

[74] Fisher, M. E. and Kolomeisky, A. B. (2001). Simple mechanochemistry describes the dynamics of kinesin molecules. Proc Natl Acad Sci U S A, 98(14):7748–53.

[75] Frank, J. (2006). Three-Dimensional Electron Microscopy of Macromolecular Assemblies. Oxford University Press, 2nd edition.

[76] Frank, J., Radermacher, M., Penczek, P., Zhu, J., Li, Y., Ladjadj, M., and Leith, A. (1996). SPIDER and WEB: processing and visualization of images in 3D electron microscopy and related fields. J Struct Biol, 116(1):190–9.

[77] Frederick, P. M., Bomans, P., Franssen, V., and Laeven, P. (2000). A vitrification robot for time resolved cryo-electron microscopy. In Cech, S. and Janisch, R., editors, Proceedings of 12th European Congress on Electron Microscopy, volume 1, pages B383–B384. Reklamni Atelier Kupa Brno.

[78] Friedman, D. S. and Vale, R. D. (1999). Single-molecule analysis of kinesin motility reveals regulation by the cargo-binding tail domain. Nat Cell Biol, 1(5):293–7.

[79] Frigo, M. and Johnson, S. G. (2005). The design and implementation of fftw3. Proc. IEEE, 93:216 – 231.

[80] Fukami, A. and Adachi, K. (1965). A new method of preparation of a self-perforated micro plastic grid and its application. J Electron Microsc (Tokyo), 14(2):112–8.

[81] Furuta, K., Edamatsu, M., Maeda, Y., and Toyoshima, Y. Y. (2008). Diffusion and directed movement: in vitro motile properties of fission yeast kinesin-14 Pkl1. J Biol Chem, 283(52):36465–73.

[82] Furuta, K. and Toyoshima, Y. Y. (2008). Minus-end-directed motor Ncd exhibits processive movement that is enhanced by microtubule bundling in vitro. Curr Biol, 18(2):152–7.

[83] Gelles, J., Berliner, E., Young, E. C., Mahtani, H. K., Perez-Ramirez, B., and Anderson, K. (1995). Structural and functional features of one- and two-headed biotinated kinesin derivatives. Biophys J, 68(4 Suppl):276S–281S; discussion 282S.

[84] Gennerich, A. and Vale, R. D. (2009). Walking the walk: how kinesin and dynein coordinate their steps. Curr Opin Cell Biol, 21(1):59–67.

[85] Gibbons, I. R. and Rowe, A. J. (1965). Dynein: A Protein with Adenosine Triphosphatase Activity from Cilia. Science, 149(3682):424–426.

[86] Gilbert, S. P., Moyer, M. L., and Johnson, K. A. (1998). Alternating site mechanism of the kinesin ATPase. Biochemistry, 37(3):792–9.

[87] Glaeser, R. M. (1971). Limitations to significant information in biological electron microscopy as a result of radiation damage. J Ultrastruct Res, 36(3):466–82.

[88] Glaeser, R. M. (1999). Review: electron crystallography: present excitement, a nod to the past, anticipating the future. J Struct Biol, 128(1):3–14.

[89] Glaeser, R. M. (2008). Retrospective: radiation damage and its associated "information limitations". J Struct Biol, 163(3):271–6.

[90] Glaeser, R. M. and Taylor, K. A. (1978). Radiation damage relative to transmission electron microscopy of biological specimens at low temperature: a review. J Microsc, 112(1):127–38.

[91] Goodman, J. W. (1968). Introduction to Fourier Optics. McGraw-Hill, 1st edition.

[92] Greene, L. E. and Eisenberg, E. (1980). Dissociation of the actin.subfragment 1 complex by adenyl-5'-yl imidodiphosphate, ADP, and PPi. J Biol Chem, 255(2):543–8.

[93] Guydosh, N. R. and Block, S. M. (2006). Backsteps induced by nucleotide analogs suggest the front head of kinesin is gated by strain. Proc Natl Acad Sci U S A, 103(21):8054–9.

[94] Hackney, D. D. (1988). Kinesin ATPase: rate-limiting ADP release. Proc Natl Acad Sci U S A, 85(17):6314–8.

[95] Hackney, D. D. (1994a). Evidence for alternating head catalysis by kinesin during microtubule-stimulated ATP hydrolysis. Proc Natl Acad Sci U S A, 91(15):6865–9.

[96] Hackney, D. D. (1994b). The rate-limiting step in microtubule-stimulated ATP hydrolysis by dimeric kinesin head domains occurs while bound to the microtubule. J Biol Chem, 269(23):16508–11.

[97] Hackney, D. D. (1995a). Highly processive microtubule-stimulated ATP hydrolysis by dimeric kinesin head domains. Nature, 377(6548):448–50.

[98] Hackney, D. D. (1995b). Implications of diffusion-controlled limit for processivity of dimeric kinesin head domains. Biophys J, 68(4 Suppl):267S–269S; discussion 269S–270S.

[99] Hackney, D. D. (1996). The kinetic cycles of myosin, kinesin, and dynein. Annu Rev Physiol, 58:731–50.

[100] Hackney, D. D. (2002). Pathway of ADP-stimulated ADP release and dissociation of tethered kinesin from microtubules. Implications for the extent of processivity. Biochemistry, 41(13):4437–46.

[101] Hackney, D. D. (2005). The tethered motor domain of a kinesin-microtubule complex catalyzes reversible synthesis of bound ATP. Proc Natl Acad Sci U S A, 102(51):18338–43.

[102] Hackney, D. D. (2007). Processive motor movement. Science, 316(5821):58–9.

[103] Hackney, D. D., Levitt, J. D., and Suhan, J. (1992). Kinesin undergoes a 9 S to 6 S conformational transition. J Biol Chem, 267(12):8696–701.

[104] Hackney, D. D., Malik, A. S., and Wright, K. W. (1989). Nucleotide-free kinesin hydrolyzes ATP with burst kinetics. J Biol Chem, 264(27):15943–8.

[105] Hackney, D. D. and Stock, M. F. (2000). Kinesin's IAK tail domain inhibits initial microtubule-stimulated ADP release. Nat Cell Biol, 2(5):257–60.

[106] Hackney, D. D. and Stock, M. F. (2008). Kinesin tail domains and Mg2+ directly inhibit release of ADP from head domains in the absence of microtubules. Biochemistry, 47(29):7770–8.

[107] Hackney, D. D., Stock, M. F., Moore, J., and Patterson, R. A. (2003). Modulation of kinesin half-site ADP release and kinetic processivity by a spacer between the head groups. Biochemistry, 42(41):12011–8.

[108] Hahlen, K., Ebbing, B., Reinders, J., Mergler, J., Sickmann, A., and Woehlke, G. (2006). Feedback of the kinesin-1 neck-linker position on the catalytic site. J Biol Chem, 281(27):18868–77.

[109] Hall, K., Cole, D. G., Yeh, Y., Scholey, J. M., and Baskin, R. J. (1993). Force-velocity relationships in kinesin-driven motility. Nature, 364(6436):457–9.

[110] Harris, J. R. (1996). Negative Staining and Cryoelectron Microscopy: The Thin Film Techniques. Garland Science, 1st edition.

[111] Harris, J. R. (2008). Negative staining across holes: application to fibril and tubular structures. Micron, 39(2):168–76.

[112] Harris, J. R., Hoeger, U., and Adrian, M. (2001). Transmission electron microscopical studies on some haemolymph proteins from the marine polychaete Nereis virens. Micron, 32(6):599–613.

[113] Harrison, B. C., Marchese-Ragona, S. P., Gilbert, S. P., Cheng, N., Steven, A. C., and Johnson, K. A. (1993). Decoration of the microtubule surface by one kinesin head per tubulin heterodimer. Nature, 362(6415):73–5.

[114] Hayward, S. B. and Glaeser, R. M. (1979). Radiation damage of purple membrane at low temperature. Ultramicroscopy, 04(2):201–10.

[115] Henningsen, U. and Schliwa, M. (1997). Reversal in the direction of movement of a molecular motor. Nature, 389(6646):93–6.

[116] Higuchi, H., Bronner, C. E., Park, H. W., and Endow, S. A. (2004). Rapid double 8-nm steps by a kinesin mutant. EMBO J, 23(15):2993–9.

[117] Higuchi, H. and Endow, S. A. (2002). Directionality and processivity of molecular motors. Curr Opin Cell Biol, 14(1):50–7.

[118] Higuchi, H., Muto, E., Inoue, Y., and Yanagida, T. (1997). Kinetics of force generation by single kinesin molecules activated by laser photolysis of caged ATP. Proc Natl Acad Sci U S A, 94(9):4395–400.

[119] Hirokawa, N., Pfister, K. K., Yorifuji, H., Wagner, M. C., Brady, S. T., and Bloom, G. S. (1989). Submolecular domains of bovine brain kinesin identified by electron microscopy and monoclonal antibody decoration. Cell, 56(5):867–78.

[120] Hirose, K., Amos, W. B., Lockhart, A., Cross, R. A., and Amos, L. A. (1997). Three-dimensional cryoelectron microscopy of 16-protofilament microtubules: structure, polarity, and interaction with motor proteins. J Struct Biol, 118(2):140–8.

[121] Hirose, K., Henningsen, U., Schliwa, M., Toyoshima, C., Shimizu, T., Alonso, M., Cross, R. A., and Amos, L. A. (2000). Structural comparison of dimeric Eg5, Neurospora kinesin (Nkin) and Ncd head-Nkin neck chimera with conventional kinesin. EMBO J, 19(20):5308–14.

[122] Hirose, K., Lockhart, A., Cross, R. A., and Amos, L. A. (1995). Nucleotide-dependent angular change in kinesin motor domain bound to tubulin. Nature, 376(6537):277–9.

[123] Hirose, K., Lowe, J., Alonso, M., Cross, R. A., and Amos, L. A. (1999a). 3D electron microscopy of the interaction of kinesin with tubulin. Cell Struct Funct, 24(5):277–84.

[124] Hirose, K., Lowe, J., Alonso, M., Cross, R. A., and Amos, L. A. (1999b). Congruent docking of dimeric kinesin and ncd into three-dimensional electron cryomicroscopy maps of microtubule-motor ADP complexes. Mol Biol Cell, 10(6):2063–74.

[125] Ho, M. H., Jap, B. K., and Glaeser, R. M. (1988). Validity domain of the weak-phase-object approximation for electron diffraction of thin protein crystals. Acta Crystallogr A, 44 (Pt 6):878–84.

[126] Hoenger, A. and Aebi, U. (1996). 3-D reconstructions from ice-embedded and negatively stained biomacromolecular assemblies: a critical comparison. J Struct Biol, 117:99–116.

[127] Hoenger, A. and Milligan, R. A. (1996). Polarity of 2-D and 3-D maps of tubulin sheets and motor-decorated sheets. J Mol Biol, 263(2):114–9.

[128] Hoenger, A., Sablin, E. P., Vale, R. D., Fletterick, R. J., and Milligan, R. A. (1995). Three-dimensional structure of a tubulin-motor-protein complex. Nature, 376(6537):271–4.

[129] Hoenger, A., Sack, S., Thormahlen, M., Marx, A., Muller, J., Gross, H., and Mandelkow, E. (1998). Image reconstructions of microtubules decorated with monomeric and dimeric kinesins: comparison with x-ray structure and implications for motility. J Cell Biol, 141(2):419–30.

[130] Hoenger, A., Thormahlen, M., Diaz-Avalos, R., Doerhoefer, M., Goldie, K. N., Muller, J., and Mandelkow, E. (2000). A new look at the microtubule binding patterns of dimeric kinesins. J Mol Biol, 297(5):1087–103.

[131] Hopkins, S. C., Vale, R. D., and Kuntz, I. D. (2000). Inhibitors of kinesin activity from structure-based computer screening. Biochemistry, 39(10):2805–14.

[132] Howard, J. (1996). The movement of kinesin along microtubules. Annu Rev Physiol, 58:703–29.

[133] Howard, J., Hudspeth, A. J., and Vale, R. D. (1989). Movement of microtubules by single kinesin molecules. Nature, 342(6246):154–8.

[134] Hua, W., Chung, J., and Gelles, J. (2002). Distinguishing inchworm and hand-over-hand processive kinesin movement by neck rotation measurements. Science, 295(5556):844–8.

[135] Huang, T. G. and Hackney, D. D. (1994). Drosophila kinesin minimal motor domain expressed in Escherichia coli. Purification and kinetic characterization. J Biol Chem, 269(23):16493–501.

[136] Huang, T. G., Suhan, J., and Hackney, D. D. (1994). Drosophila kinesin motor domain extending to amino acid position 392 is dimeric when expressed in Escherichia coli. J Biol Chem, 269(23):16502–7.

[137] Hunt, A. J., Gittes, F., and Howard, J. (1994). The force exerted by a single kinesin molecule against a viscous load. Biophys J, 67(2):766–81.

[138] Hunt, A. J. and Howard, J. (1993). Kinesin swivels to permit microtubule movement in any direction. Proc Natl Acad Sci U S A, 90(24):11653–7.

[139] Huxley, A. F. (1957). Muscle structure and theories of contraction. Prog Biophys Biophys Chem, 7:255–318.

[140] Hwang, W., Lang, M. J., and Karplus, M. (2008). Force generation in kinesin hinges on cover-neck bundle formation. Structure, 16(1):62–71.

[141] Hyeon, C. and Onuchic, J. N. (2007a). Internal strain regulates the nucleotide binding site of the kinesin leading head. Proc Natl Acad Sci U S A, 104(7):2175–80.

[142] Hyeon, C. and Onuchic, J. N. (2007b). Mechanical control of the directional stepping dynamics of the kinesin motor. Proc Natl Acad Sci U S A, 104(44):17382–7.

[143] Iancu, C. V., Tivol, W. F., Schooler, J. B., Dias, D. P., Henderson, G. P., Murphy, G. E., Wright, E. R., Li, Z., Yu, Z., Briegel, A., Gan, L., He, Y., and Jensen, G. J. (2006). Electron cryotomography sample preparation using the Vitrobot. Nat Protoc, 1(6):2813–9.

[144] Inoue, Y., Toyoshima, Y. Y., Iwane, A. H., Morimoto, S., Higuchi, H., and Yanagida, T. (1997). Movements of truncated kinesin fragments with a short or an artificial flexible neck. Proc Natl Acad Sci U S A, 94(14):7275–80.

[145] Ishii, Y., Taniguchi, Y., Iwaki, M., and Yanagida, T. (2008). Thermal fluctuations biased for directional motion in molecular motors. Biosystems, 93(1-2):34–8.

[146] Jankowsky, E. and Fairman, M. E. (2007). RNA helicases–one fold for many functions. Curr Opin Struct Biol, 17(3):316–24.

[147] Jeng, T. W., Crowther, R. A., Stubbs, G., and Chiu, W. (1989). Visualization of alpha-helices in tobacco mosaic virus by cryo-electron microscopy. J Mol Biol, 205(1):251–7.

[148] Jiang, W. and Hackney, D. D. (1997). Monomeric kinesin head domains hydrolyze multiple ATP molecules before release from a microtubule. J Biol Chem, 272(9):5616–21.

[149] Jiang, W., Stock, M. F., Li, X., and Hackney, D. D. (1997). Influence of the kinesin neck domain on dimerization and ATPase kinetics. J Biol Chem, 272(12):7626–32.

[150] Johnson, M. E. (2000). Potential neurotoxicity of spinal anesthesia with lidocaine. Mayo Clin Proc, 75(9):921–32.

[151] Kamal, A. and Goldstein, L. S. (2002). Principles of cargo attachment to cytoplasmic motor proteins. Curr Opin Cell Biol, 14(1):63–8.

[152] Kamimura, S. and Mandelkow, E. (1992). Tubulin protofilaments and kinesin-dependent motility. J Cell Biol, 118(4):865–75.

[153] Kapoor, T. M., Mayer, T. U., Coughlin, M. L., and Mitchison, T. J. (2000). Probing spindle assembly mechanisms with monastrol, a small molecule inhibitor of the mitotic kinesin, Eg5. J Cell Biol, 150(5):975–88.

[154] Kaseda, K., Higuchi, H., and Hirose, K. (2002). Coordination of kinesin's two heads studied with mutant heterodimers. Proc Natl Acad Sci U S A, 99(25):16058–63.

[155] Kaseda, K., Higuchi, H., and Hirose, K. (2003). Alternate fast and slow stepping of a heterodimeric kinesin molecule. Nat Cell Biol, 5(12):1079–82.

[156] Kawaguchi, K. and Ishiwata, S. (2000). Temperature dependence of force, velocity, and processivity of single kinesin molecules. Biochem Biophys Res Commun, 272(3):895–9.

[157] Kawaguchi, K. and Ishiwata, S. (2001). Nucleotide-dependent single- to double-headed binding of kinesin. Science, 291(5504):667–9.

[158] Kawaguchi, K., Uemura, S., and Ishiwata, S. (2003). Equilibrium and transition between single- and double-headed binding of kinesin as revealed by single-molecule mechanics. Biophys J, 84(2 Pt 1):1103–13.

[159] Kellenberger, E., Haner, M., and Wurtz, M. (1982). The wrapping phenomenon in air-dried and negatively stained preparations. Ultramicroscopy, 9(1-2):139–50.

[160] Kellenberger, E. and Kistler, J. (1979). The physics of specimen preparation. In Hoppe, W. and Mason, R., editors, Advances in Structure Research by Diffraction Methods, volume 3, pages 49–79. Vieweg und Sohn.

[161] Khalil, A. S., Appleyard, D. C., Labno, A. K., Georges, A., Karplus, M., Belcher, A. M., Hwang, W., and Lang, M. J. (2008). Kinesin's cover-neck bundle folds forward to generate force. Proc Natl Acad Sci U S A, 105(49):19247–52.

[162] Kikkawa, M. (2004). A new theory and algorithm for reconstructing helical structures with a seam. J Mol Biol, 343(4):943–55.

[163] Kikkawa, M. (2008). The role of microtubules in processive kinesin movement. Trends Cell Biol, 18(3):128–35.

[164] Kikkawa, M. and Hirokawa, N. (2006). High-resolution cryo-EM maps show the nucleotide binding pocket of KIF1A in open and closed conformations. EMBO J, 25(18):4187–94.

[165] Kikkawa, M., Ishikawa, T., Nakata, T., Wakabayashi, T., and Hirokawa, N. (1994). Direct visualization of the microtubule lattice seam both in vitro and in vivo. J Cell Biol, 127(6 Pt 2):1965–71.

[166] Kikkawa, M., Ishikawa, T., Wakabayashi, T., and Hirokawa, N. (1995). Three-dimensional structure of the kinesin head-microtubule complex. Nature, 376(6537):274–7.

[167] Kikkawa, M., Okada, Y., and Hirokawa, N. (2000). 15 A resolution model of the monomeric kinesin motor, KIF1A. Cell, 100(2):241–52.

[168] Kikkawa, M., Sablin, E. P., Okada, Y., Yajima, H., Fletterick, R. J., and Hirokawa, N. (2001). Switch-based mechanism of kinesin motors. Nature, 411(6836):439–45.

[169] Kiselev, N. A., DeRosier, D. J., and Klug, A. (1968). Structure of the tubes of catalase: analysis of electron micrographs by optical filtering. J Mol Biol, 35(3):561–6.

[170] Kiselev, N. A. and Klug, A. (1969). The structure of viruses of the papilloma-polyoma type. V. Tubular variants built of pentamers. J Mol Biol, 40(2):155–71.

[171] Kiselev, N. A., Sherman, M. B., and Tsuprun, V. L. (1990). Negative staining of proteins. Electron Microsc Rev, 3(1):43–72.

[172] Kistler, J. and Kellenberger, E. (1977). Collapse phenomena in freeze-drying. J Ultrastruct Res, 59(1):70–5.

[173] Kleywegt, G. J. (1996). Use of non-crystallographic symmetry in protein structure refinement. Acta Crystallogr D Biol Crystallogr, 52(Pt 4):842–57.

[174] Kleywegt, G. J. (1999). Experimental assessment of differences between related protein crystal structures. Acta Crystallogr D Biol Crystallogr, 55(Pt 11):1878–84.

[175] Kleywegt, G. J. and Jones, T. A. (1995). Where freedom is given, liberties are taken. Structure, 3(6):535–40.

[176] Kleywegt, G. J. and Jones, T. A. (1996a). Phi/psi-chology: Ramachandran revisited. Structure, 4(12):1395–400.

[177] Kleywegt, G. J. and Jones, T. A. (1996b). xdlMAPMAN and xdlDATAMAN - programs for reformatting, analysis and manipulation of biomacromolecular electron-density maps and reflection data sets. Acta Crystallogr D Biol Crystallogr, 52(Pt 4):826–8.

[178] Kleywegt, G. J. and Jones, T. A. (1997). Detecting folding motifs and similarities in protein structures. Methods Enzymol, 277:525–45.

[179] Klug, A., Crick, F., and Wyckoff, H. (1958). Diffraction by helical structures. Acta Cryst., 11:199–213.

[180] Klug, A. and DeRosier, D. J. (1966). Optical filtering of electron micrographs: reconstruction of one-sided images. Nature, 212(5057):29–32.

[181] Klumpp, L. M., Hoenger, A., and Gilbert, S. P. (2004). Kinesin's second step. Proc Natl Acad Sci U S A, 101(10):3444–9.

[182] Knapek, E. and Dubochet, J. (1980). Beam damage to organic material is considerably reduced in cryo-electron microscopy. J Mol Biol, 141(2):147–61.

[183] Knoll, M. and Ruska, E. (1931). Zeitung fuer Tech. Phys, 12:389.

[184] Kull, F. J., Sablin, E. P., Lau, R., Fletterick, R. J., and Vale, R. D. (1996). Crystal structure of the kinesin motor domain reveals a structural similarity to myosin. Nature, 380(6574):550–5.

[185] Kuo, I. A. and Glaeser, R. M. (1975). Development of methodology for low exposure, high resolution electron microscopy of biological specimens. Ultramicroscopy, 1(1):53–66.

[186] Kuo, J. (2007). Electron Microscopy: Methods and Protocols (Methods in Molecular Biology). Humana Press, 2nd edition.

[187] Lasek, R. J. and Brady, S. T. (1985). Attachment of transported vesicles to microtubules in axoplasm is facilitated by AMP-PNP. Nature, 316(6029):645–7.

[188] Lawrence, C. J., Dawe, R. K., Christie, K. R., Cleveland, D. W., Dawson, S. C., Endow, S. A., Goldstein, L. S., Goodson, H. V., Hirokawa, N., Howard, J., Malmberg, R. L., McIntosh, J. R., Miki, H., Mitchison, T. J., Okada, Y., Reddy, A. S., Saxton, W. M., Schliwa, M., Scholey, J. M., Vale, R. D., Walczak, C. E., and Wordeman, L. (2004). A standardized kinesin nomenclature. J Cell Biol, 167(1):19–22.

[189] Lepault, J., Booy, F. P., and Dubochet, J. (1983). Electron microscopy of frozen biological suspensions. J Microsc, 129(Pt 1):89–102.

[190] Li, H., DeRosier, D. J., Nicholson, W. V., Nogales, E., and Downing, K. H. (2002). Microtubule structure at 8 A resolution. Structure, 10(10):1317–28.

[191] Lowe, J., Li, H., Downing, K. H., and Nogales, E. (2001). Refined structure of alpha beta-tubulin at 3.5 A resolution. J Mol Biol, 313(5):1045–57.

[192] Ludtke, S. J., Baker, M. L., Chen, D. H., Song, J. L., Chuang, D. T., and Chiu, W. (2008). De novo backbone trace of GroEL from single particle electron cryomicroscopy. Structure, 16(3):441–8.

[193] Ludtke, S. J., Baldwin, P. R., and Chiu, W. (1999). EMAN: semiautomated software for high-resolution single-particle reconstructions. J Struct Biol, 128(1):82–97.

[194] Ludtke, S. J., Jakana, J., Song, J. L., Chuang, D. T., and Chiu, W. (2001). A 11.5 A single particle reconstruction of GroEL using EMAN. J Mol Biol, 314(2):253–62.

[195] Lymn, R. W. and Taylor, E. W. (1971). Mechanism of adenosine triphosphate hydrolysis by actomyosin. Biochemistry, 10(25):4617–24.

[196] Ma, Y. Z. and Taylor, E. W. (1995). Mechanism of microtubule kinesin ATPase. Biochemistry, 34(40):13242–51.

[197] Ma, Y. Z. and Taylor, E. W. (1997a). Interacting head mechanism of microtubule-kinesin ATPase. J Biol Chem, 272(2):724–30.

[198] Ma, Y. Z. and Taylor, E. W. (1997b). Kinetic mechanism of a monomeric kinesin construct. J Biol Chem, 272(2):717–23.

[199] Mandelkow, E. and Hoenger, A. (1999). Structures of kinesin and kinesin-microtubule interactions. Curr Opin Cell Biol, 11(1):34–44.

[200] Mandelkow, E. and Mandelkow, E. M. (2002). Kinesin motors and disease. Trends Cell Biol, 12(12):585–91.

[201] Marszalek, J. R., Ruiz-Lozano, P., Roberts, E., Chien, K. R., and Goldstein, L. S. (1999). Situs inversus and embryonic ciliary morphogenesis defects in mouse mutants lacking the KIF3A subunit of kinesin-II. Proc Natl Acad Sci U S A, 96(9):5043–8.

[202] Massover, W. H. (2008). On the experimental use of light metal salts for negative staining. Microsc Microanal, 14(2):126–37.

[203] Massover, W. H., Lai, P. F., and Marsh, P. (2001). Negative staining permits 4.0 A resolution with low-dose electron diffraction of catalase crystals. Ultramicroscopy, 90(1):7–12.

[204] Mather, W. H. and Fox, R. F. (2006). Kinesin's biased stepping mechanism: amplification of neck linker zippering. Biophys J, 91(7):2416–26.

[205] Matsumoto, Y. (2001). Ruby in a Nutshell. O'Reilly Media.

[206] Meluh, P. B. and Rose, M. D. (1990). KAR3, a kinesin-related gene required for yeast nuclear fusion. Cell, 60(6):1029–41.

[207] Metlagel, Z., Kikkawa, Y. S., and Kikkawa, M. (2007). Ruby-Helix: an implementation of helical image processing based on object-oriented scripting language. J Struct Biol, 157(1):95–105.

[208] Milescu, L. S., Yildiz, A., Selvin, P. R., and Sachs, F. (2006). Maximum likelihood estimation of molecular motor kinetics from staircase dwell-time sequences. Biophys J, 91(4):1156–68.

[209] Mimori, Y., Yamashita, I., Murata, K., Fujiyoshi, Y., Yonekura, K., Toyoshima, C., and Namba, K. (1995). The structure of the R-type straight flagellar filament of Salmonella at 9 A resolution by electron cryomicroscopy. J Mol Biol, 249(1):69–87.

[210] Miyamoto, Y., Muto, E., Mashimo, T., Iwane, A. H., Yoshiya, I., and Yanagida, T. (2000). Direct inhibition of microtubule-based kinesin motility by local anesthetics. Biophys J, 78(2):940–9.

[211] Miyazawa, A., Fujiyoshi, Y., Stowell, M., and Unwin, N. (1999). Nicotinic acetylcholine receptor at 4.6 A resolution: transverse tunnels in the channel wall. J Mol Biol, 288(4):765–86.

[212] Moore, A. and Wordeman, L. (2004). The mechanism, function and regulation of depolymerizing kinesins during mitosis. Trends Cell Biol, 14(10):537–46.

[213] Moores, C. A., Yu, M., Guo, J., Beraud, C., Sakowicz, R., and Milligan, R. A. (2002). A mechanism for microtubule depolymerization by KinI kinesins. Mol Cell, 9(4):903–9.

[214] Mori, T., Vale, R. D., and Tomishige, M. (2007). How kinesin waits between steps. Nature, 450(7170):750–4.

[215] Morii, H., Takenawa, T., Arisaka, F., and Shimizu, T. (1997). Identification of kinesin neck region as a stable alpha-helical coiled coil and its thermodynamic characterization. Biochemistry, 36(7):1933–42.

[216] Moyer, M. L., Gilbert, S. P., and Johnson, K. A. (1996). Purification and characterization of two monomeric kinesin constructs. Biochemistry, 35(20):6321–9.

[217] Moyer, M. L., Gilbert, S. P., and Johnson, K. A. (1998). Pathway of ATP hydrolysis by monomeric and dimeric kinesin. Biochemistry, 37(3):800–13.

[218] Naber, N., Minehardt, T. J., Rice, S., Chen, X., Grammer, J., Matuska, M., Vale, R. D., Kollman, P. A., Car, R., Yount, R. G., Cooke, R., and Pate, E. (2003a). Closing of the nucleotide pocket of kinesin-family motors upon binding to microtubules. Science, 300(5620):798–801.

[219] Naber, N., Rice, S., Matuska, M., Vale, R. D., Cooke, R., and Pate, E. (2003b). EPR spectroscopy shows a microtubule-dependent conformational change in the kinesin switch 1 domain. Biophys J, 84(5):3190–6.

[220] Niclas, J., Navone, F., Hom-Booher, N., and Vale, R. D. (1994). Cloning and localization of a conventional kinesin motor expressed exclusively in neurons. Neuron, 12(5):1059–72.

[221] Nishiyama, M., Higuchi, H., Ishii, Y., Taniguchi, Y., and Yanagida, T. (2003). Single molecule processes on the stepwise movement of ATP-driven molecular motors. Biosystems, 71(1-2):145–56.

[222] Nishiyama, M., Higuchi, H., and Yanagida, T. (2002). Chemomechanical coupling of the forward and backward steps of single kinesin molecules. Nat Cell Biol, 4(10):790–7.

[223] Nitta, R., Kikkawa, M., Okada, Y., and Hirokawa, N. (2004). KIF1A alternately uses two loops to bind microtubules. Science, 305(5684):678–83.

[224] Nonaka, S., Tanaka, Y., Okada, Y., Takeda, S., Harada, A., Kanai, Y., Kido, M., and Hirokawa, N. (1998). Randomization of left-right asymmetry due to loss of nodal cilia generating leftward flow of extraembryonic fluid in mice lacking KIF3B motor protein. Cell, 95(6):829–37.

[225] Okada, Y., Higuchi, H., and Hirokawa, N. (2003). Processivity of the single-headed kinesin KIF1A through biased binding to tubulin. Nature, 424(6948):574–7.

[226] Okada, Y. and Hirokawa, N. (1999). A processive single-headed motor: kinesin superfamily protein KIF1A. Science, 283(5405):1152–7.

[227] Okada, Y. and Hirokawa, N. (2000). Mechanism of the single-headed processivity: diffusional anchoring between the K-loop of kinesin and the C terminus of tubulin. Proc Natl Acad Sci U S A, 97(2):640–5.

[228] Otwinowski, Z. and Minor, W. (1997). Processing of x-ray diffraction data collected in oscillation mode. Methods in Enzymology, 276:307–326.

[229] Ovechkina, Y., Wagenbach, M., and Wordeman, L. (2002). K-loop insertion restores microtubule depolymerizing activity of a "neckless" MCAK mutant. J Cell Biol, 159(4):557–62.

[230] Owen, C. H., Morgan, D. G., and DeRosier, D. J. (1996). Image analysis of helical objects: the Brandeis Helical Package. J Struct Biol, 116(1):167–75.

[231] Pechatnikova, E. and Taylor, E. W. (1999). Kinetics processivity and the direction of motion of Ncd. Biophys J, 77(2):1003–16.

[232] Penczek, P., Marko, M., Buttle, K., and Frank, J. (1995). Double-tilt electron tomography. Ultramicroscopy, 60(3):393–410.

[233] Perez-Castro, R., Patel, S., Garavito-Aguilar, Z. V., Rosenberg, A., Recio-Pinto, E., Zhang, J., Blanck, T. J., and Xu, F. (2009). Cytotoxicity of local anesthetics in human neuronal cells. Anesth Analg, 108(3):997–1007.

[234] Peskin, C. S. and Oster, G. (1995). Coordinated hydrolysis explains the mechanical behavior of kinesin. Biophys J, 68(4 Suppl):202S–210S; discussion 210S–211S.

[235] Peterman, E. J., Sosa, H., and Moerner, W. E. (2004). Single-molecule fluorescence spectroscopy and microscopy of biomolecular motors. Annu Rev Phys Chem, 55:79–96.

[236] Pettersen, E. F., Goddard, T. D., Huang, C. C., Couch, G. S., Greenblatt, D. M., Meng, E. C., and Ferrin, T. E. (2004). UCSF Chimera–a visualization system for exploratory research and analysis. J Comput Chem, 25(13):1605–12.

[237] Pierce, D. W., Hom-Booher, N., Otsuka, A. J., and Vale, R. D. (1999). Single-molecule behavior of monomeric and heteromeric kinesins. Biochemistry, 38(17):5412–21.

[238] Potter, C. S., Chu, H., Frey, B., Green, C., Kisseberth, N., Madden, T. J., Miller, K. L., Nahrstedt, K., Pulokas, J., Reilein, A., Tcheng, D., Weber, D., and Carragher, B. (1999). Leginon: a system for fully automated acquisition of 1000 electron micrographs a day. Ultramicroscopy, 77(3-4):153–61.

[239] Quispe, J., Damiano, J., Mick, S. E., Nackashi, D. P., Fellmann, D., Ajero, T. G., Carragher, B., and Potter, C. S. (2007). An improved holey carbon film for cryo-electron microscopy. Microsc Microanal, 13(5):365–71.

[240] Rao, V. B. and Feiss, M. (2008). The Bacteriophage DNA Packaging Motor. Annu Rev Genet.

[241] Ray, S., Meyhofer, E., Milligan, R. A., and Howard, J. (1993). Kinesin follows the microtubule's protofilament axis. J Cell Biol, 121(5):1083–93.

[242] Reck-Peterson, S. L., Yildiz, A., Carter, A. P., Gennerich, A., Zhang, N., and Vale, R. D. (2006). Single-molecule analysis of dynein processivity and stepping behavior. Cell, 126(2):335–48.

[243] Reimer, L. (1998). Transmission Electron Microscopy: Physics of Image Formation and Microanalysis. Springer, 4th edition.

[244] Rice, S., Cui, Y., Sindelar, C., Naber, N., Matuska, M., Vale, R., and Cooke, R. (2003). Thermodynamic properties of the kinesin neck-region docking to the catalytic core. Biophys J, 84(3):1844–54.

[245] Rice, S., Lin, A. W., Safer, D., Hart, C. L., Naber, N., Carragher, B. O., Cain, S. M., Pechatnikova, E., Wilson-Kubalek, E. M., Whittaker, M., Pate, E., Cooke, R., Taylor, E. W., Milligan, R. A., and Vale, R. D. (1999). A structural change in the kinesin motor protein that drives motility. Nature, 402(6763):778–84.

[246] Rogers, G. C., Rogers, S. L., Schwimmer, T. A., Ems-McClung, S. C., Walczak, C. E., Vale, R. D., Scholey, J. M., and Sharp, D. J. (2004). Two mitotic kinesins cooperate to drive sister chromatid separation during anaphase. Nature, 427(6972):364–70.

[247] Romberg, L., Pierce, D. W., and Vale, R. D. (1998). Role of the kinesin neck region in processive microtubule-based motility. J Cell Biol, 140(6):1407–16.

[248] Rose, H. (1984). Information transfer in transmission electron microscopy. Ultramicroscopy, 15(3):173 – 191.

[249] Roseman, A. M., Ranson, N. A., Gowen, B., Fuller, S. D., and Saibil, H. R. (2001). Structures of unliganded and ATP-bound states of the Escherichia coli chaperonin GroEL by cryoelectron microscopy. J Struct Biol, 135(2):115–25.

[250] Rosenfeld, S. S., Fordyce, P. M., Jefferson, G. M., King, P. H., and Block, S. M. (2003). Stepping and stretching. How kinesin uses internal strain to walk processively. J Biol Chem, 278(20):18550–6.

[251] Rosenfeld, S. S., Jefferson, G. M., and King, P. H. (2001). ATP reorients the neck linker of kinesin in two sequential steps. J Biol Chem, 276(43):40167–74.

[252] Rosenfeld, S. S., Xing, J., Jefferson, G. M., and King, P. H. (2005). Docking and rolling, a model of how the mitotic motor Eg5 works. J Biol Chem, 280(42):35684–95.

[253] Rouiller, I., Pulokas, J., Butel, V. M., Milligan, R. A., Wilson-Kubalek, E. M., Potter, C. S., and Carragher, B. O. (2001). Automated image acquisition for single-particle reconstruction using p97 as the biological sample. J Struct Biol, 133(2-3):102–7.

[254] Ruiz, T., Ranck, J. L., Diaz-Avalos, R., Caspar, D. L., and DeRosier, D. J. (1994). Electron diffraction of helical particles. Ultramicroscopy, 55(4):383–95.

[255] Sablin, E. P., Case, R. B., Dai, S. C., Hart, C. L., Ruby, A., Vale, R. D., and Fletterick, R. J. (1998). Direction determination in the minus-end-directed kinesin motor ncd. Nature, 395(6704):813–6.

[256] Sablin, E. P. and Fletterick, R. J. (2004). Coordination between motor domains in processive kinesins. J Biol Chem, 279(16):15707–10.

[257] Sablin, E. P., Kull, F. J., Cooke, R., Vale, R. D., and Fletterick, R. J. (1996). Crystal structure of the motor domain of the kinesin-related motor ncd. Nature, 380(6574):555–9.

[258] Sack, S., Muller, J., Marx, A., Thormahlen, M., Mandelkow, E. M., Brady, S. T., and Mandelkow, E. (1997). X-ray structure of motor and neck domains from rat brain kinesin. Biochemistry, 36(51):16155–65.

[259] Sackett, D. L., Bhattacharyya, B., and Wolff, J. (1985). Tubulin subunit carboxyl termini determine polymerization efficiency. J Biol Chem, 260(1):43–5.

[260] Sadhu, A. and Taylor, E. W. (1992). A kinetic study of the kinesin ATPase. J Biol Chem, 267(16):11352–9.

[261] Sakowicz, R., Berdelis, M. S., Ray, K., Blackburn, C. L., Hopmann, C., Faulkner, D. J., and Goldstein, L. S. (1998). A marine natural product inhibitor of kinesin motors. Science, 280(5361):292–5.

[262] Sartori Blanc, N., Studer, D., Ruhl, K., and Dubochet, J. (1998). Electron beam-induced changes in vitreous sections of biological samples. J Microsc, 192(Pt 2):194–201.

[263] Satir, P. (1995). A decade of kinesin, three decades of dynein. Trends Cell Biol, 5(7):266–7.

[264] Schief, W. R., Clark, R. H., Crevenna, A. H., and Howard, J. (2004). Inhibition of kinesin motility by ADP and phosphate supports a hand-over-hand mechanism. Proc Natl Acad Sci U S A, 101(5):1183–8.

[265] Schnitzer, M. J. and Block, S. M. (1997). Kinesin hydrolyses one ATP per 8-nm step. Nature, 388(6640):386–90.

[266] Shao, Q. and Gao, Y. Q. (2006). On the hand-over-hand mechanism of kinesin. Proc Natl Acad Sci U S A, 103(21):8072–7.

[267] Shao, Q. and Gao, Y. Q. (2007). Asymmetry in kinesin walking. Biochemistry, 46(31):9098–106.

[268] Sherman, M. B., Orlova, E. V., Terzyan, S. S., Kleine, R., and Kiselev, N. A. (1981). On the negative straining of the protein crystal structure. Ultramicroscopy, 7(2):131–8.

[269] Shipley, K., Hekmat-Nejad, M., Turner, J., Moores, C., Anderson, R., Milligan, R., Sakowicz, R., and Fletterick, R. (2004). Structure of a kinesin microtubule depolymerization machine. EMBO J, 23(7):1422–32.

[270] Sindelar, C. V., Budny, M. J., Rice, S., Naber, N., Fletterick, R., and Cooke, R. (2002). Two conformations in the human kinesin power stroke defined by X-ray crystallography and EPR spectroscopy. Nat Struct Biol, 9(11):844–8.

[271] Sindelar, C. V. and Downing, K. H. (2007). The beginning of kinesin's force-generating cycle visualized at 9-A resolution. J Cell Biol, 177(3):377–85.

[272] Skiniotis, G., Surrey, T., Altmann, S., Gross, H., Song, Y. H., Mandelkow, E., and Hoenger, A. (2003). Nucleotide-induced conformations in the neck region of dimeric kinesin. EMBO J, 22(7):1518–28.

[273] Skowronek, K. J., Kocik, E., and Kasprzak, A. A. (2007). Subunits interactions in kinesin motors. Eur J Cell Biol, 86(9):559–68.

[274] Slayter, E. M. and Slayter, H. S. (1992). Light and Electron Microscopy. Cambridge University Press.

[275] Snoeys, J., Lievens, J., Wisse, E., Jacobs, F., Duimel, H., Collen, D., Frederik, P., and De Geest, B. (2007). Species differences in transgene DNA uptake in hepatocytes after adenoviral transfer correlate with the size of endothelial fenestrae. Gene Ther, 14(7):604–12.

[276] Song, Y. H. and Mandelkow, E. (1993). Recombinant kinesin motor domain binds to beta-tubulin and decorates microtubules with a B surface lattice. Proc Natl Acad Sci U S A, 90(5):1671–5.

[277] Song, Y. H. and Mandelkow, E. (1995). The anatomy of flagellar microtubules: polarity, seam, junctions, and lattice. J Cell Biol, 128(1-2):81–94.

[278] Sosa, H., Peterman, E. J., Moerner, W. E., and Goldstein, L. S. (2001). ADP-induced rocking of the kinesin motor domain revealed by single-molecule fluorescence polarization microscopy. Nat Struct Biol, 8(6):540–4.

[279] Sowa, Y. and Berry, R. M. (2008). Bacterial flagellar motor. Q Rev Biophys, 41(2):103–32.

[280] Sprinzl, M. (1994). Elongation factor Tu: a regulatory GTPase with an integrated effector. Trends Biochem Sci, 19(6):245–50.

[281] Stagg, S. M., Lander, G. C., Pulokas, J., Fellmann, D., Cheng, A., Quispe, J. D., Mallick, S. P., Avila, R. M., Carragher, B., and Potter, C. S. (2006). Automated cryoEM data acquisition and analysis of 284742 particles of GroEL. J Struct Biol, 155(3):470–81.

[282] Stark, H., Dube, P., Luhrmann, R., and Kastner, B. (2001). Arrangement of RNA and proteins in the spliceosomal U1 small nuclear ribonucleoprotein particle. Nature, 409(6819):539–42.

[283] Stock, M. F., Guerrero, J., Cobb, B., Eggers, C. T., Huang, T. G., Li, X., and Hackney, D. D. (1999). Formation of the compact confomer of kinesin requires a COOH-terminal heavy chain domain and inhibits microtubule-stimulated ATPase activity. J Biol Chem, 274(21):14617–23.

[284] Stumpff, J., Cooper, J., Domnitz, S., Moore, A. T., Rankin, K. E., Wagenbach, M., and Wordeman, L. (2007). In vitro and in vivo analysis of microtubule-destabilizing kinesins. Methods Mol Biol, 392:37–49.

[285] Sugata, K., Nakamura, M., Ueki, S., Fajer, P. G., and Arata, T. (2004). ESR reveals the mobility of the neck linker in dimeric kinesin. Biochem Biophys Res Commun, 314(2):447–51.

[286] Suloway, C., Pulokas, J., Fellmann, D., Cheng, A., Guerra, F., Quispe, J., Stagg, S., Potter, C. S., and Carragher, B. (2005). Automated molecular microscopy: the new Leginon system. J Struct Biol, 151(1):41–60.

[287] Svoboda, K. and Block, S. M. (1994). Force and velocity measured for single kinesin molecules. Cell, 77(5):773–84.

[288] Svoboda, K., Mitra, P. P., and Block, S. M. (1995). Fluctuation analysis of kinesin movement. Biophys J, 68(4 Suppl):69S.

[289] Svoboda, K., Schmidt, C. F., Schnapp, B. J., and Block, S. M. (1993). Direct observation of kinesin stepping by optical trapping interferometry. Nature, 365(6448):721–7.

[290] Takeda, S., Yonekawa, Y., Tanaka, Y., Okada, Y., Nonaka, S., and Hirokawa, N. (1999). Left-right asymmetry and kinesin superfamily protein KIF3A: new insights in determination of laterality and mesoderm induction by kif3A-/- mice analysis. J Cell Biol, 145(4):825–36.

[291] Tanaka, Y., Kanai, Y., Okada, Y., Nonaka, S., Takeda, S., Harada, A., and Hirokawa, N. (1998). Targeted disruption of mouse conventional kinesin heavy chain, kif5B, results in abnormal perinuclear clustering of mitochondria. Cell, 93(7):1147–58.

[292] Taniguchi, Y., Nishiyama, M., Ishii, Y., and Yanagida, T. (2005). Entropy rectifies the Brownian steps of kinesin. Nat Chem Biol, 1(6):342–7.

[293] Taylor, K. A. and Glaeser, R. M. (1974). Electron diffraction of frozen, hydrated protein crystals. Science, 186(4168):1036–7.

[294] Taylor, K. A. and Glaeser, R. M. (1976). Electron microscopy of frozen hydrated biological specimens. J Ultrastruct Res, 55(3):448–56.

[295] Thomas, D., Fowler, C., and Hunt, A. (2004). Programming Ruby: The Pragmatic Programmers' Guide. Pragmatic Bookshelf.

[296] Thoresen, T. and Gelles, J. (2008). Processive movement by a kinesin heterodimer with an inactivating mutation in one head. Biochemistry, 47(36):9514–21.

[297] Thormahlen, M., Marx, A., Muller, S. A., Song, Y., Mandelkow, E. M., Aebi, U., and Mandelkow, E. (1998). Interaction of monomeric and dimeric kinesin with microtubules. J Mol Biol, 275(5):795–809.

[298] Toba, S., Watanabe, T. M., Yamaguchi-Okimoto, L., Toyoshima, Y. Y., and Higuchi, H. (2006). Overlapping hand-over-hand mechanism of single molecular motility of cytoplasmic dynein. Proc Natl Acad Sci U S A, 103(15):5741–5.

[299] Tomishige, M., Stuurman, N., and Vale, R. D. (2006). Single-molecule observations of neck linker conformational changes in the kinesin motor protein. Nat Struct Mol Biol, 13(10):887–94.

[300] Tomishige, M. and Vale, R. D. (2000). Controlling kinesin by reversible disulfide cross-linking. Identifying the motility-producing conformational change. J Cell Biol, 151(5):1081–92.

[301] Tomkiewicz, D., Nouwen, N., and Driessen, A. J. (2008). Kinetics and energetics of the translocation of maltose binding protein folding mutants. J Mol Biol, 377(1):83–90.

[302] Toyoshima, C. (2000). Structure determination of tubular crystals of membrane proteins. I. Indexing of diffraction patterns. Ultramicroscopy, 84(1-2):1–14.

[303] Toyoshima, C. and Unwin, N. (1988). Ion channel of acetylcholine receptor reconstructed from images of postsynaptic membranes. Nature, 336(6196):247–50.

[304] Toyoshima, C. and Unwin, N. (1990). Three-dimensional structure of the acetylcholine receptor by cryoelectron microscopy and helical image reconstruction. J Cell Biol, 111(6 Pt 1):2623–35.

[305] Trachtenberg, S., DeRosier, D. J., Zemlin, F., and Beckmann, E. (1998). Nonhelical perturbations of the flagellar filament: Salmonella typhimurium SJW117 at 9.6 A resolution. J Mol Biol, 276(4):759–73.

[306] Tripet, B., Vale, R. D., and Hodges, R. S. (1997). Demonstration of coiled-coil interactions within the kinesin neck region using synthetic peptides. Implications for motor activity. J Biol Chem, 272(14):8946–56.

[307] Uemura, S. and Ishiwata, S. (2003). Loading direction regulates the affinity of ADP for kinesin. Nat Struct Biol, 10(4):308–11.

[308] Uemura, S., Kawaguchi, K., Yajima, J., Edamatsu, M., Toyoshima, Y. Y., and Ishiwata, S. (2002). Kinesin-microtubule binding depends on both nucleotide state and loading direction. Proc Natl Acad Sci U S A, 99(9):5977–81.

[309] Unwin, N. (1993). Nicotinic acetylcholine receptor at 9 A resolution. J Mol Biol, 229(4):1101–24.

[310] Unwin, N. (1996). Projection structure of the nicotinic acetylcholine receptor: distinct conformations of the alpha subunits. J Mol Biol, 257(3):586–96.

[311] Unwin, N. (2005). Refined structure of the nicotinic acetylcholine receptor at 4A resolution. J Mol Biol, 346(4):967–89.

[312] Vale, R. D. (1996). Switches, latches, and amplifiers: common themes of G proteins and molecular motors. J Cell Biol, 135(2):291–302.

[313] Vale, R. D., Case, R., Sablin, E., Hart, C., and Fletterick, R. (2000). Searching for kinesin's mechanical amplifier. Philos Trans R Soc Lond B Biol Sci, 355(1396):449–57.

[314] Vale, R. D. and Fletterick, R. J. (1997). The design plan of kinesin motors. Annu Rev Cell Dev Biol, 13:745–77.

[315] Vale, R. D., Funatsu, T., Pierce, D. W., Romberg, L., Harada, Y., and Yanagida, T. (1996). Direct observation of single kinesin molecules moving along microtubules. Nature, 380(6573):451–3.

[316] Vale, R. D. and Milligan, R. A. (2000). The way things move: looking under the hood of molecular motor proteins. Science, 288(5463):88–95.

[317] Vale, R. D. and Oosawa, F. (1990). Protein motors and Maxwell's demons: does mechanochemical transduction involve a thermal ratchet? Adv Biophys, 26:97–134.

[318] Vale, R. D., Reese, T. S., and Sheetz, M. P. (1985). Identification of a novel force-generating protein, kinesin, involved in microtubule-based motility. Cell, 42(1):39–50.

[319] Valentine, R. C., Shapiro, B. M., and Stadtman, E. R. (1968). Regulation of glutamine synthetase. XII. Electron microscopy of the enzyme from Escherichia coli. Biochemistry, 7(6):2143–52.

[320] van Heel, M. (1986). Similarity measures between images. Ultramicroscopy, 21:95–100.

[321] van Heel, M. (1987). Angular reconstitution: a posteriori assignment of projection directions for 3D reconstruction. Ultramicroscopy, 21(2):111–23.

[322] van Heel, M. and Schatz, M. (2005). Fourier shell correlation threshold criteria. J Struct Biol, 151(3):250–62.

[323] Verhey, K. J., Lizotte, D. L., Abramson, T., Barenboim, L., Schnapp, B. J., and Rapoport, T. A. (1998). Light chain-dependent regulation of Kinesin's interaction with microtubules. J Cell Biol, 143(4):1053–66.

[324] Visscher, K., Schnitzer, M. J., and Block, S. M. (1999). Single kinesin molecules studied with a molecular force clamp. Nature, 400(6740):184–9.

[325] von Massow, A., Mandelkow, E. M., and Mandelkow, E. (1989). Interaction between kinesin, microtubules, and microtubule-associated protein 2. Cell Motil Cytoskeleton, 14(4):562–71.

[326] Vos, M. R., Bomans, P. H., Frederik, P. M., and Sommerdijk, N. A. (2008). The development of a glove-box/Vitrobot combination: air-water interface events visualized by cryo-TEM. Ultramicroscopy, 108(11):1478–83.

[327] Vugmeyster, Y., Berliner, E., and Gelles, J. (1998). Release of isolated single kinesin molecules from microtubules. Biochemistry, 37(2):747–57.

[328] Whittaker, M., Carragher, B. O., and Milligan, R. A. (1995). PHOELIX: a package for semi-automated helical reconstruction. Ultramicroscopy, 58(3-4):245–59.

[329] Woehlke, G., Ruby, A. K., Hart, C. L., Ly, B., Hom-Booher, N., and Vale, R. D. (1997). Microtubule interaction site of the kinesin motor. Cell, 90(2):207–16.

[330] Wolf, S. G., Nogales, E., Kikkawa, M., Gratzinger, D., Hirokawa, N., and Downing, K. H. (1996). Interpreting a medium-resolution model of tubulin: comparison of zinc-sheet and microtubule structure. J Mol Biol, 262(4):485–501.

[331] Wood, R. W. (1897). Diffraction of X-rays obtained by a new form of cathode discharge. Science, 5(119):585.

[332] Wriggers, W. and Birmanns, S. (2001). Using situs for flexible and rigid-body fitting of multiresolution single-molecule data. J Struct Biol, 133(2-3):193–202.

[333] Wriggers, W., Milligan, R. A., and McCammon, J. A. (1999). Situs: A package for docking crystal structures into low-resolution maps from electron microscopy. J Struct Biol, 125(2-3):185–95.

[334] Wriggers, W. and Schulten, K. (1998). Nucleotide-dependent movements of the kinesin motor domain predicted by simulated annealing. Biophys J, 75(2):646–61.

[335] Xing, J., Wriggers, W., Jefferson, G. M., Stein, R., Cheung, H. C., and Rosenfeld, S. S. (2000). Kinesin has three nucleotide-dependent conformations. Implications for strain-dependent release. J Biol Chem, 275(45):35413–23.

[336] Yajima, J., Alonso, M. C., Cross, R. A., and Toyoshima, Y. Y. (2002). Direct long-term observation of kinesin processivity at low load. Curr Biol, 12(4):301–6.

[337] Yang, J. T., Laymon, R. A., and Goldstein, L. S. (1989). A three-domain structure of kinesin heavy chain revealed by DNA sequence and microtubule binding analyses. Cell, 56(5):879–89.

[338] Yang, J. T., Saxton, W. M., Stewart, R. J., Raff, E. C., and Goldstein, L. S. (1990). Evidence that the head of kinesin is sufficient for force generation and motility in vitro. Science, 249(4964):42–7.

[339] Yasunaga, T. and Wakabayashi, T. (1996). Extensible and object-oriented system Eos supplies a new environment for image analysis of electron micrographs of macromolecules. J Struct Biol, 116(1):155–60.

[340] Yildiz, A. and Selvin, P. R. (2005a). Fluorescence imaging with one nanometer accuracy: application to molecular motors. Acc Chem Res, 38(7):574–82.

[341] Yildiz, A. and Selvin, P. R. (2005b). Kinesin: walking, crawling or sliding along? Trends Cell Biol, 15(2):112–20.

[342] Yildiz, A., Tomishige, M., Gennerich, A., and Vale, R. D. (2008). Intramolecular strain coordinates kinesin stepping behavior along microtubules. Cell, 134(6):1030–41.

[343] Yildiz, A., Tomishige, M., Vale, R. D., and Selvin, P. R. (2004). Kinesin walks hand-over-hand. Science, 303(5658):676–8.

[344] Yonekura, K., Maki-Yonekura, S., and Namba, K. (2001). Structure analysis of the flagellar cap-filament complex by electron cryomicroscopy and single-particle image analysis. J Struct Biol, 133(2-3):246–53.

[345] Yonekura, K., Toyoshima, C., Maki-Yonekura, S., and Namba, K. (2003). GUI programs for processing individual images in early stages of helical image reconstruction–for high-resolution structure analysis. J Struct Biol, 144(1-2):184–94.

[346] Young, E. C., Berliner, E., Mahtani, H. K., Perez-Ramirez, B., and Gelles, J. (1995). Subunit interactions in dimeric kinesin heavy chain derivatives that lack the kinesin rod. J Biol Chem, 270(8):3926–31.

[347] Young, E. C., Mahtani, H. K., and Gelles, J. (1998). One-headed kinesin derivatives move by a nonprocessive, low-duty ratio mechanism unlike that of two-headed kinesin. Biochemistry, 37(10):3467–79.

[348] Zemlin, F., Beckmann, E., and van der Mast, K. D. (1996). A 200 kV eletron microscope with Schottky Field emitter and a helium-cooled superconducting objective lens. Ultramicroscopy, 3:227–238.

[349] Zhou, Z. H. (2008). Towards atomic resolution structural determination by single-particle cryo-electron microscopy. Curr Opin Struct Biol, 18(2):218–28.